TURUN
YLIOPISTO
UNIVERSITY
OF TURKU

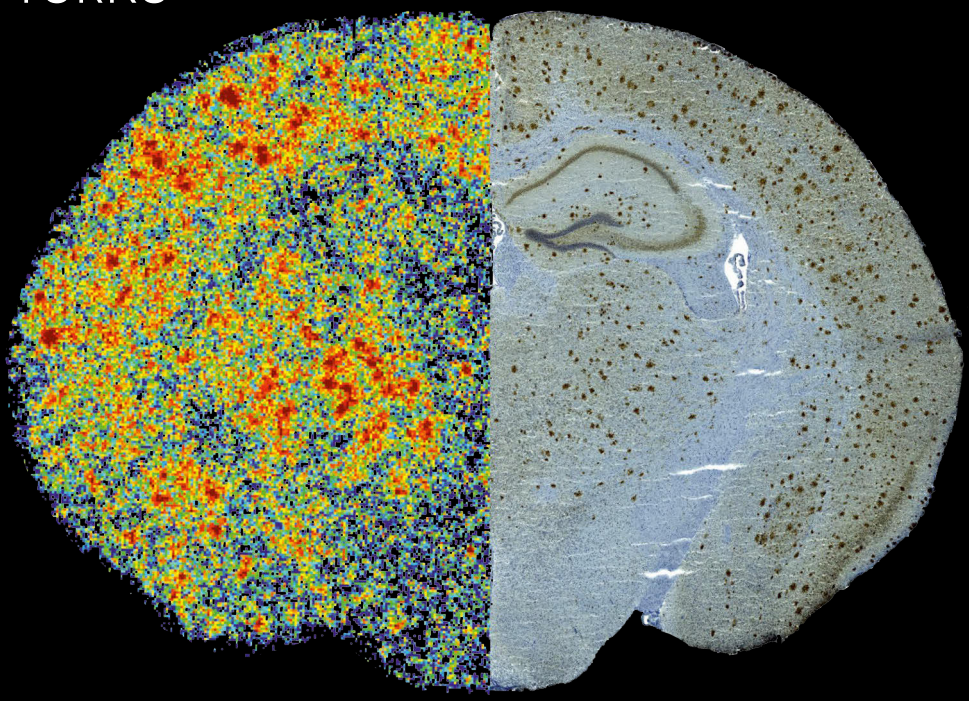

PRECLINICAL DEVELOPMENT OF RADIOPHARMACEUTICALS FOR ALZHEIMER'S DISEASE

Biological Evaluation of (*S*)-[^{18}F]THK5117 and [^{11}C]SMW139 PET Tracers in the APP/PS1-21 Mouse Model of Alzheimer's Disease

Obada Al-Zghool

TURUN YLIOPISTON JULKAISUJA – ANNALES UNIVERSITATIS TURKUENSIS
SARJA – SER. D OSA – TOM. 1774 | MEDICA – ODONTOLOGICA | TURKU 2024

TURUN
YLIOPISTO
UNIVERSITY
OF TURKU

PRECLINICAL DEVELOPMENT OF RADIOPHARMACEUTICALS FOR ALZHEIMER'S DISEASE

Biological Evaluation of (*S*)-[^{18}F]THK5117 and [^{11}C]SMW139 PET Tracers in the APP/PS1-21 Mouse Model of Alzheimer's Disease

Obada Al-Zghool

TURUN YLIOPISTON JULKAISUJA – ANNALES UNIVERSITATIS TURKUENSIS
SARJA – SER. D OSA – TOM. 1774 | MEDICA – ODONTOLOGICA | TURKU 2024

University of Turku

Faculty of Medicine
Department of Clinical Medicine
Clinical Physiology and Nuclear Medicine
Drug Research Doctoral Programme
Turku PET Centre

Supervised by

Adjunct professor Merja Haaparanta-Solin, PhD
Turku PET Centre
University of Turku
Turku, Finland

Professor Juha Rinne, MD, PhD
Turku PET Centre
Turku University Hospital
University of Turku
Turku, Finland

Reviewed by

Associate Professor Kristina Herfert, PhD
Werner Siemens Imaging Center
University of Tübingen
Tübingen, Germany

Adjunct Professor Eino Solje, MD, PhD
Institute of Clinical Medicine
University of Eastern Finland
Kuopio, Finland

Opponent

Associate Professor Mikael Palner, PhD
Department of Clinical Research
University of Southern Denmark
Odense, Denmark

The originality of this publication has been checked in accordance with the University of Turku quality assurance system using the Turnitin OriginalityCheck service.

Cover Image: Obada Al-zghool

ISBN 978-951-29-9603-2 (PRINT)
ISBN 978-951-29-9604-9 (PDF)
ISSN 0355-9483 (Print)
ISSN 2343-3213 (Online)
Painosalama, Turku, Finland 2024

To my father

To my mother

UNIVERSITY OF TURKU
Faculty of Medicine
Department of Clinical Medicine
Clinical Physiology and Nuclear Medicine
Turku PET Centre
OBADA AL-ZGHOOL: Preclinical Development of Radiopharmaceuticals for Alzheimer's Disease – Biological Evaluation of (*S*)-[^{18}F]THK5117 and [^{11}C]SMW139 PET Tracers in the APP/PS1-21 Mouse Model of Alzheimer's Disease
Doctoral Dissertation, 153 pp.
Drug Research Doctoral Programme
February 2024

ABSTRACT

Alzheimer's disease (AD) pathological cascade is characterised by the formation of β-amyloid peptide (Aβ) plaques and neurofibrillary tangles of hyperphosphorylated tau (p-tau) in association with neuroinflammation. Positron emission tomography (PET) allows *in vivo* imaging of these neuropathological changes in living subjects using PET tracers, which opens applications for PET in AD diagnosis and drug development. Imaging rodent models of AD with PET tracers is a valuable translational approach in developing PET tracers for clinical use.

The aim of this thesis work was to conduct a preclinical evaluation of the PET tracers (*S*)-[^{18}F]THK5117 and [^{11}C]SMW139 in the APP/PS1-21 mouse model of AD. *In vivo* PET and *ex vivo* autoradiography were used to assess the binding of (*S*)-[^{18}F]THK5117 to p-tau aggregates, and [^{11}C]SMW139 to P2X7 receptor. Immunohistochemical staining was used to validate the imaging targets. In addition, *ex vivo* methods were used to investigate tracers' pharmacokinetic profile.

In the APP/PS1-21 mice, (*S*)-[^{18}F]THK5117 brain uptake associated with Aβ plaques and MAO-B enzyme, but not p-tau aggregates. [^{11}C]SMW139 longitudinal uptake did not increase with ageing, despite the ongoing neuroinflammation in APP/PS1-21 mice. Histological assessment of imaging targets associated well with PET and autoradiography imaging findings. (*S*)-[^{18}F]THK5117 showed suitable pharmacokinetic properties, whereas [^{11}C]SMW139 presented fast and unfavoured metabolism for *in vivo* imaging.

In conclusion, tracers preclinical evaluation performed in the APP/PS1-21 mouse model of AD showed that (*S*)-[^{18}F]THK5117 *in vivo* binding in the brain is predominantly non-specific, and [^{11}C]SMW139 binding is low. Collectively, findings of this thesis work revealed that *in vivo* PET imaging of tau pathology with (*S*)-[^{18}F]THK5117 and reactive glia with [^{11}C]SMW139 in mice are associated with major limitations, proposing limited preclinical and possibly clinical applications of both tracers.

KEYWORDS: Alzheimer's disease, APP/PS1-21, PET, (*S*)-[^{18}F]THK5117, tau, [^{11}C]SMW139, P2X7 receptor

TURUN YLIOPISTO
Lääketieteellinen tiedekunta
Kliininen laitos
Kliininen fysiologia ja isotooppilääketiede
Turun PET-keskus
OBADA AL-ZGHOOL: Alzheimerin taudin radiolääkkeiden prekliininen kehitys – (*S*)-[^{18}F]THK5117 ja [^{11}C]SMW139 PET-merkkiaineiden biologinen arviointi Alzheimerin taudin APP/PS1-21 hiirimallissa
Väitöskirja, 153 s.
Lääketutkimuksen tohtoriohjelma
Helmikuu 2024

TIIVISTELMÄ

Alzheimerin taudille (AD) on tunnusomaista β-amyloidipeptidiplakkien (Aβ) ja hyperfosforyloituneen tau:n (p-tau) neurofibrillaaristen säikeiden muodostuminen hermokudoksen tulehduksen yhteydessä. Positroniemissiotomografia (PET) tarjoaa mahdollisuuden näiden neuropatologisten muutosten *in vivo* -kuvantamiseen elävillä henkilöillä käyttämällä PET-merkkiaineita. Tämä avaa PET-sovelluksia AD-diagnoosissa ja lääkekehityksessä. Kliinisesti hyväksyttyjen PET-merkkiaineiden saatavuus on haaste. AD-jyrsijämallien kuvantaminen uusilla PET-merkkiaineilla antaa arvokasta translaationaalista tietoa PET-merkkiaineiden kehitykseen.

Tämän väitöskirjan tavoitteena oli PET-merkkiaineiden (*S*)-[^{18}F]THK5117 ja [^{11}C]SMW139 prekliininen kehitys käyttäen AD:n APP/PS1-21-hiirimallia. *In vivo* -PETiä ja *ex vivo* -autoradiografiaa käytettiin p-tau-aggregaattien kuvantamiseen (*S*)-[^{18}F]THK5117:llä ja reaktiivisen glia-P2X7-reseptorin kuvantamiseen [^{11}C]SMW139:llä. Aivojen kuvantamiskohteiden arvioimiseen käytettiin immunohistokemiallista värjäystä, ja *ex vivo* -menetelmiä hyödynnettiin merkkiaineiden farmakokinetiikkaprofiilin tutkimiseen.

APP/PS1-21-hiirillä havaittiin, että (*S*)-[^{18}F]THK5117:n aivokertymä liittyi Aβ-plakkeihin ja MAO-B-entsyymiin, mutta ei p-tau-aggregaatteihin. [^{11}C]SMW139:n kertymä ei lisääntynyt ikääntyessä, vaikka hermostotulehdus jatkui APP/PS1-21-hiirissä. Kuvantamislöydöt korreloivat histologisen analyysin kanssa. (*S*)-[^{18}F]THK5117:llä oli sopivia farmakokineettisiä ominaisuuksia, kun taas [^{11}C]SMW139:llä oli epäsuotuisa metabolia *in vivo* -kuvantamisen kannalta.

Tämän väitöskirjan prekliininen merkkiainetutkimus AD:n APP/PS1-21-hiirimallissa osotti, että (*S*)-[^{18}F]THK5117:n aivokertymä on pääasiassa epäspesifistä ja [^{11}C]SMW139:n kertymä oli vähäistä. Tau-patologian PET-kuvantamisessa (*S*)-[^{18}F]THK5117:llä ja hermotulehduksen kuvantamisessa [^{11}C]SMW139:llä on suuria rajoituksia, mikä voi viitata haasteisiin näiden merkkiaineiden kliinisessä käyttössä.

AVAISSANAT: Alzheimerin tauti, APP/PS1-21, PET, (*S*)-[^{18}F]THK5117, tau, [^{11}C]SMW139, P2X7 reseptori

Table of Contents

Abbreviations

AD	Alzheimer's disease
WHO	World Health Organization
Aβ	β-amyloid peptides
NFTs	neurofibrillary tangles
p-tau	hyperphosphorylated tau
PET	positron emission tomography
ADME	absorption, distribution, metabolism and excretion
tg	transgenic
MCI	mild cognitive impairment
NIA	National Institute on Aging
CSF	cerebrospinal fluid
ApoE	apolipoprotein E
TREM2	triggering receptor expressed on myeloid cells 2
APP	Aβ-precursor protein
PSEN 1	presenilin 1
PSEN 2	presenilin 2
BBB	blood-brain barrier
NTs	neuropil threads
PHFs	paired helical filaments
CNS	central nervous system
GFAP	glial fibrillary acidic protein
TSPO	translocator protein 18-kDa
P2X7	purinergic 2 type X subtype 7
wt	wild type
e^+	positron
e^-	electron
mm	millimetre
3D	three-dimensional
Am	molar activity
p.i.	post-injection
MAO-B	monoamine oxidase B

FDA	Food and Drug Administration
EMA	European Medicines Agency
MS	Multiple Sclerosis
IHC	immunohistochemical
ROI	region of interest
VOI	volume of interest
FC	frontal cortex
STR	striatum
HIPPO	hippocampus
THA	thalamus
CTX	cortex
NC	neocortex
CB	cerebellum
CT	computed tomography
MRI	magnetic resonance imaging
MBq	mega Becquerel
SUV	standardized uptake value
TAC	time-activity curve
%IA/g	percentage injected radioactivity per gram
min	minute
TLC	thin-layer chromatography
RadioTLC	radio-thin-layer chromatography
f_p	free parent tracer over all radioactivity
f_M	free radiometabolites over all radioactivity
PPB	plasma protein binding
Rf	retardation factor
PVE	partial volume effect
Pgp	P-glycoprotein
PSL/pixel-Bkg	background radioactivity-corrected photo-stimulated luminescence intensity per pixel

List of Original Publications

This dissertation is based on the following original publications, which are referred to in the text by their Roman numerals:

I **Alzghool OM**, Rokka J, López-Picón FR, Snellman A, Helin JS, Okamura N, Solin O, Rinne JO, Haaparanta-Solin M. (*S*)-[^{18}F]THK5117 brain uptake is associated with Aβ plaques and MAO-B enzyme in a mouse model of Alzheimer's disease. *Neuropharmacology*, 2021; 196:108676.

II **Alzghool OM**, Aarnio R, Helin JS, Wahlroos S, Keller T, Matilainen M, Solis J, Danon JJ, Kassiou M, Snellman A, Solin O, Rinne JO, Haaparanta-Solin M. Microglial reactivity in a mouse model of beta-amyloid deposition assessed by PET imaging of P2X7 receptor and TSPO using [^{11}C]SMW139 and [^{18}F]F-DPA. Manuscript.

III Aarnio R, **Alzghool OM**, Wahlroos S, O'Brien-Brown J, Kassiou M, Solin O, Rinne JO, Forsback S, Haaparanta-Solin M. Novel plasma protein binding analysis method for a PET tracer and its radiometabolites: A case study with [^{11}C]SMW139 to explain the high uptake of radiometabolites in mouse brain. *Journal of Pharmaceutical and Biomedical Analysis*, 2022; 219:114860.

Additional results that are previously unpublished are also presented.

1 Introduction

Alzheimer's disease (AD) is a neurodegenerative brain disease that is characterised by progressive cognitive decline, eventually leading to terminal secondary illness and death. AD is the most common type of dementia, accounting for 60-70% of all dementia cases. According to the World Health Organization (WHO), over 55 million people worldwide suffer from AD or other types of dementia, and every year there are nearly 10 million new cases (1). In AD, progressive neuronal damage occurs as a result of multiple neuropathological processes, mainly the accumulation of extracellular aggregates of β-amyloid peptides (Aβ) and intracellular inclusions of hyperphosphorylated tau protein (p-tau) (2). Aggregation of Aβ plaques and NFTs is associated with neuroinflammation in the brain (3).

In the past, pathological hallmarks, including Aβ plaques and tau NFTs, were only possible to examine *post-mortem* from AD patients. Nowadays, using positron emission tomography (PET) imaging, it is possible to detect, visualise and monitor amyloid (4) and tau (5) pathologies and neuroinflammation (6) *in vivo* and non-invasively in living subjects. PET is a nuclear imaging method used to investigate various physiological and pathological processes. In the PET method, a positron-emitting radionuclide, such as ^{18}F or ^{11}C, is introduced to a molecule forming a PET tracer that, upon administration to the subject, binds to a specific target, such as a pathological form of a protein or receptor system, generating quantitative information about the investigated target detected inside the PET scanner.

The preclinical development of PET tracers often dictates whether the tracer can be used clinically or not. Thus, a comprehensive biological evaluation of newly developed PET tracers is crucial. Typically, tracer binding properties (affinity and selectivity) and pharmacokinetics profile (ADME: absorption, distribution, metabolism and excretion) are assessed in experimental animals using *in vivo* PET imaging, combined with *in vitro* and *ex vivo* methods to validate the imaging findings. In the scope of AD, transgenic (tg) rodent models expressing the target of interest in the brain are valuable tools in the preclinical evaluation of tracer binding properties and pharmacokinetics profile (7) (8) (9) (10) (11) (12). Also, PET imaging and tracers that are well-characterised and clinically available represent a valuable tool to evaluate the suitability of tg models as translational tools in the preclinical

development of new PET tracers and AD therapies, allowing quantitative and non-invasive assessment (13) (14) (15) (16) (17) (18).

There are clinically available PET tracers capable of revealing the level of Aβ plaques and NFTs in the brain (19) (20), and used as imaging biomarkers in AD diagnosis (21). Nonetheless, there is a need for better imaging biomarkers with improved *in vivo* pharmacokinetics profile, binding sensitivity and specificity for Aβ plaques, NFTs, and other markers of AD neuropathological processes, which could improve the early diagnosis of AD. That represents the rationale for developing new PET tracers and the work presented in the studies of this thesis.

The aim of this thesis was to evaluate newly developed PET tracers and assess the APP/PS1-21 mouse model as a translational tool in the preclinical development of PET tracers. The work of this thesis describes the evaluation of binding properties and pharmacokinetics profile of p-tau targeting tracer, (*S*)-[^{18}F]THK5117, in APP/PS1-21 tg mice (**study I**). In addition, longitudinal imaging of neuroinflammatory reactive glia in the APP/PS1-21 tg mice using [^{11}C]SMW139 and [^{18}F]F-DPA, and evaluating [^{11}C]SMW139 pharmacokinetics profile (**study II**). Finally, the evaluation of [^{11}C]SMW139 pharmacokinetic properties and the analysis of tracer and radiometabolites binding to plasma proteins in mice (**study III**). The outline and shared aspects of studies **I-III** are presented in Figure 1.

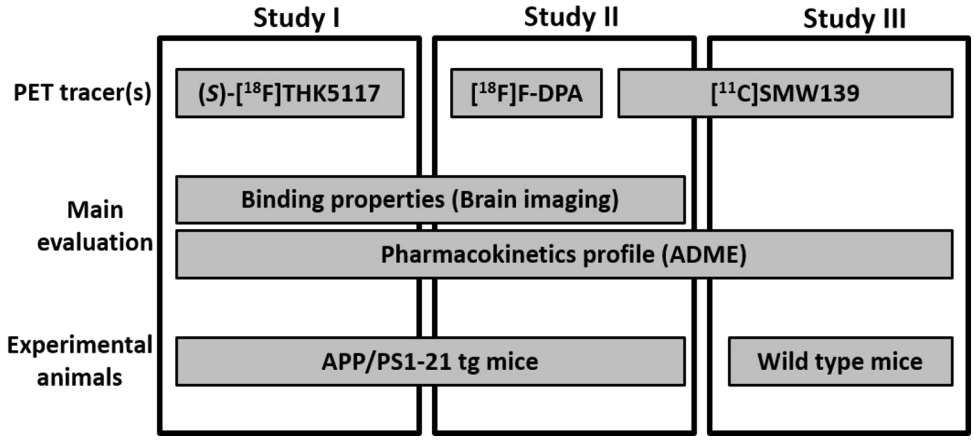

Figure 1. Studies I-III outline and shared aspects. ADME: Absorption, distribution, metabolism, excretion. tg: transgenic.

2 Review of the Literature

2.1 Alzheimer's disease

> "November 29th 1901:
>
> *How are you?* It is always one as the other. Who carried me here? *Where are you?* At the moment, I have temporarily, as I said, I have no means. One simply has to… I don't know myself… I really don't know… dear me, what is to then? *What is your name?* Frau Auguste D. *When were you born?* Eighteen hundred and… *In which year were you born?* This year, no, last year. *When were you born?* Eighteen hundred — I don't know. *What did I ask you?* Ah, D. Auguste. […] *What is your husband called?* I don't know…"
>
> Dr. Alzheimer's original notes as quoted in (22)

In 1906, the German psychiatrist and neuropathologist Alois Alzheimer presented the case of his late patient Auguste D., in which he described "unusual disease of the cerebral cortex". Today, this disease is known as Alzheimer's disease. Auguste D. suffered from progressive cognitive impairment, and her brain showed histopathological lesions, currently known as Aβ plaques and tau NFTs (22).

2.1.1 The continuum of Alzheimer's disease

Cognition refers to a range of mental processes relating to learning new things, using and remembering stored information, and solving problems. Moreover, cognition plays a role in human behaviour, time and space awareness, and response to social and emotional stimuli (23). Normal ageing is associated with a subtle decline in some cognitive functions (24); in AD, the decline is broader and more aggressive. The progression of AD from neuropathological processes in the brain that are unnoticeable by the individual to neuropathological processes that cause cognitive decline and, ultimately, physical, mental, and emotional disabilities is called the AD continuum. There are three phases on this continuum: preclinical AD, mild cognitive

impairment (MCI) due to AD, and dementia due to AD. The AD dementia phase is further divided into mild, moderate and severe (Figure 2) (25). While the AD continuum starts with preclinical AD and ends with severe AD dementia, the length of each phase of the continuum varies between individuals. Besides, not all individuals progress from preclinical AD to MCI and AD dementia phases (26) (27). Up to 26% of individuals with MCI never convert to AD dementia or could even revert to preclinical AD (28), while more than 50% of MCI cases progress to develop AD dementia within five years (29).

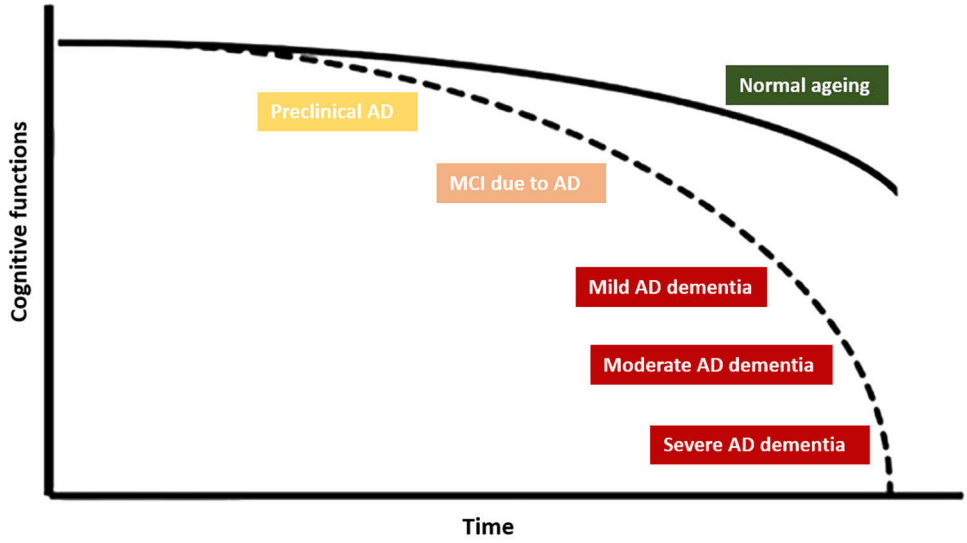

Figure 2. Cognitive decline with aging and AD continuum. AD: Alzheimer's disease, MCI: Mild cognitive impairment. Figure modified from (30).

Preclinical AD is the phase where individuals may have biomarker evidence of AD neuropathological processes that do not lead to clinical symptoms, as the brain can compensate for the damage caused by AD neuropathological processes. This phase is detectable mainly in individuals with pre-existing risk factors or family history or in research and clinical trial settings. *MCI due to AD* is the phase where individuals have biomarker evidence of ongoing neuropathological processes and start to experience subtle difficulties with memory, thinking, and language that do not interfere with daily activities. These subtle symptoms start to appear because the brain can no longer compensate for the ongoing damage. *Dementia due to AD* is characterised by concrete biomarker evidence of AD and intensifying difficulties with memory, language, thinking and behaviour that interfere with the ability to perform daily activities (25).

The progression of AD symptoms from mild to severe differs between individuals. In mild AD, most patients can still function independently but may need assistance in some instrumental activities to maintain safety. Common symptoms of mild AD include forgetting familiar words, the location of everyday objects, and difficulty with planning, organizing, and concentration. In moderate AD, patients are unable to function independently and need more assistance. Additional symptoms include difficulties performing routine, multistep tasks like dressing, episodes of reactive and unexpected behaviour, and difficulty expressing thoughts and emotions. In severe AD, care around the clock is needed as the patient becomes increasingly unable to communicate verbally and loses awareness of their surroundings. Due to brain damage in areas responsible for movement, the patient experiences a decline in simple physical abilities such as walking and sitting and becomes bedridden. As a result, vulnerability to secondary physical complications increases. In addition, because of damage in brain areas that control swallowing, it becomes difficult to eat and drink, and more likely that food particles are swallowed into the trachea and deposited in the lungs, causing aspiration pneumonia, a common cause of death in AD patients. The AD continuum can last up to 20 years, during which AD patient lives on average 4-8 years after diagnosis (25) (31).

The vast majority of AD cases occur in individuals over 65 years of age, thus categorised as late-onset AD, which is more common in women than men (32). It is believed that late-onset AD develops because of multiple factors rather than a single cause. With late-onset AD, advancing in age is the most significant risk factor. The percentage of individuals with AD increases notably beyond the age of 65 (25). According to the National Institute on Aging (NIA), about one in 13 people age 65 to 84 and one in three people 85 and older are living with AD (33). Genetics is another risk factor with a well-established association with late-onset AD, most notably individuals with Down syndrome (34), apolipoprotein E (*APOE*) allele e4 carriers (35), and the triggering receptor expressed on myeloid cells 2 (*TREM2*) AD-variants (36). Family history is also a risk factor, even though it does not necessarily guarantee developing AD. Individuals with first-degree relatives (parent or sibling) with AD are more likely to develop AD than individuals with no AD family history (37) (38). Additionally, having more than one first-degree relative with AD increases the individual's likelihood of developing AD even more (39). Other risk factors of late-onset AD are generally modifiable and include mainly physical activity, social and mental activity, education, diet, smoking, diabetes and hypertension (25). It is suggested that up to 40% of dementia cases could be delayed or prevented by addressing these modifiable risk factors (40). The Finnish intervention study to prevent cognitive decline and disability (FINGER) was the first study to show that a multidomain lifestyle intervention is beneficial for preventing cognitive decline in individuals at risk of developing dementia (41). On the other hand, 1-5% of all AD

cases are early-onset (42). This category mostly includes *familial* AD, which occurs due to mutations in Aβ-precursor protein (*APP*), presenilin 1 (*PSEN1*) or presenilin 2 (*PSEN2*) genes, which have a causative relationship with AD and result in a very aggressive form of the disease (43) (44).

2.1.2 Diagnosis and treatment of Alzheimer's disease

In the past, a definitive diagnosis of AD was only feasible *post-mortem* by acquiring neuropathological evidence of AD pathology on autopsy (45). Despite that still being a practice (46) (47), nowadays, diagnosing AD in a living subject can be achieved by utilising accurate biomarkers imaged in the brain and measured in the cerebrospinal fluid (CSF) combined with cognitive tests (48). According to the latest recommendations of the International Working Group, AD clinical diagnosis entails both positive biomarkers and AD-specific clinical phenotypes, which highlight the brain dysfunction that the biomarkers are signalling. Evidence of biomarker abnormality without accompanying clinical symptoms is not sufficient to confirm the diagnosis of AD, and individuals falling in this category should be classified as at risk for progression to AD (49). Biomarkers emerge at different stages of the AD continuum, as shown by the dynamic biomarker changes model (Figure 3) (50). Biomarkers of amyloid and tau pathologies appear abnormal at all stages of the AD continuum, including the asymptomatic preclinical stage. Currently established biomarkers include CSF $A\beta_{42}$, total and p-tau, amyloid PET, and tau PET (50) (51). Aggregation of Aβ in the brain correlates with decreased levels of $A\beta_{42}$ in the CSF and amyloid-positive PET scan (52) (53). Meanwhile, the aggregation of p-tau correlates with increased CSF total and p-tau and tau-positive PET scan (54) (53). Other AD biomarkers detect structural changes in the brain, thus highlighting neuronal damage and neurodegeneration. These biomarkers include hippocampal grey matter atrophy detected by magnetic resonance imaging (MRI), and reduced cortical metabolic activity assessed with [^{18}F]FDG PET (50). Both hippocampal atrophy and [^{18}F]FDG hypometabolism associate with tau but not amyloid pathology (50) (55). Neurodegeneration biomarkers are not usually present in the early stages of the disease and are not only specific for AD. Thus, they are more valuable in assessing the progression of AD than early diagnosis (50) (46). Notably, the latest recommendations of the International Working Group state that increased tracer uptake in amyloid PET, tau PET, and [^{18}F]FDG-PET hypometabolism can be used as biomarker measures in AD diagnosis; however, PET imaging cannot be recommended for routine use in AD diagnosis, due to financial cost, limited accessibility, and regulatory restrictions (49).

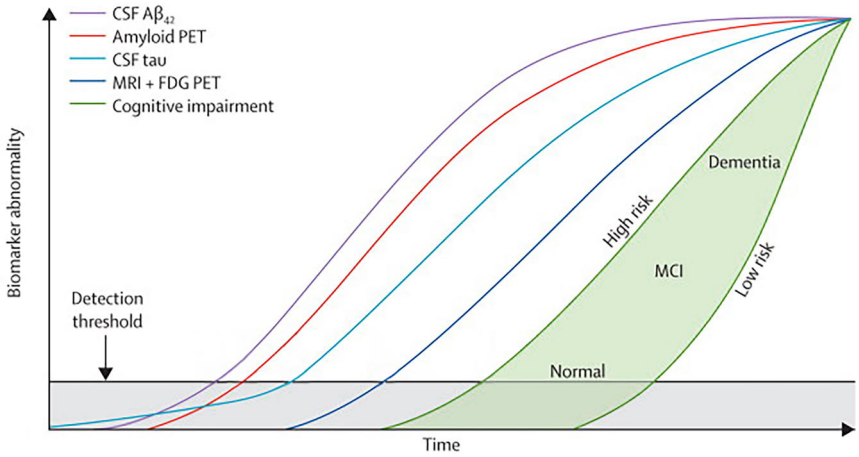

Figure 3. Biomarkers dynamic change model in Alzheimer's disease (AD) continuum. Decreased $A\beta_{42}$ in the cerebrospinal fluid (CSF) and positive amyloid PET are the first detected biomarkers in AD. Although tau pathology precedes amyloid pathology, biomarker levels in CSF and PET are below the detection threshold at this stage. As AD progresses, tau biomarkers are detected in CSF and PET. Then, brain atrophy is detected with magnetic resonance imaging (MRI), and hypometabolism is detected with [^{18}F]FDG PET, both revealing ongoing neurodegeneration. After all biomarkers show abnormalities, cognitive impairment and clinical symptoms follow. Cognitive impairment is presented as a zone because individuals with similar biomarker profiles could have different clinical course of AD, depending on their exposure to risk and protective factors. The black horizontal line refers to the biomarkers detection threshold. Figure modified from (50).

Integrating biomarkers in routine AD diagnosis helps establish early diagnosis and confirm a probable diagnosis of AD (46) (56). Moreover, biomarker-supported early diagnosis of AD is highly valuable to include the correct subjects in clinical trials and research studies and to allow better treatment planning. A timely diagnosis of AD allows for early medical intervention with symptomatic and novel treatments with potential disease-modifying effects, which could affect the course of the disease, better manage associated symptoms and postpone institutionalisation (25) (57). There are seven drugs treating AD. Two of these drugs, *aducanumab* and *lecanemab*, could currently be regarded as biomarker-modifying treatments, as their disease-modifying effect is yet to be established. Both drugs aim to alter the course of AD by clearing Aβ deposits and slow cognitive decline in individuals with early AD, including MCI and mild AD. Nonetheless, neither treatment cures AD. The other five drugs, *dopenzil*, *rivastigmine*, *galantamine*, *memantine*, *memantine with dopenzil*, treat cognitive symptoms in individuals with moderate and severe AD but do not affect the underlying pathophysiological processes causing the symptoms nor the course of the disease. These medications improve symptoms by maintaining the levels of acetylcholine neurotransmitter, or in the case of memantine limiting the effect of the neurotransmitter glutamate (58) (59). The AD drug development

pipeline is active. Several disease-modifying treatments targeting tau pathology, neuroinflammation and other pathological processes are being developed (60). Ultimately, disease-modifying treatments that address several pathological processes beyond Aβ deposition are needed to cure AD.

2.1.3 Neuropathological processes of Alzheimer's disease

The healthy brain of an adult has billions of neurons. Extensions of these neurons are connected, allowing different neurons to communicate. There are trillions of these connections, i.e., synapses in the brain where neurotransmitters, the brain's signal, are exchanged between connected neurons, creating a cellular foundation for memories, cognition, feelings and movement. Aggregation of Aβ and p-tau into deposits of varying sizes and structures, are two of several neuropathological processes causing the gradual death of neurons in AD (2). The ongoing amyloid and tau pathologies trigger the immune system in the brain to clear the toxic protein aggregates and debris of dying neurons, eventually leading to a state of chronic neuroinflammation as immune cells become unable to handle the needs. The other associated neuropathological change is neurodegeneration, which manifests as brain atrophy and glucose hypometabolism, compromising normal brain functions even further (Figure 4) (61) (62). Nonetheless, the complete sequence of pathological processes in AD is still partly unresolved at the molecular level.

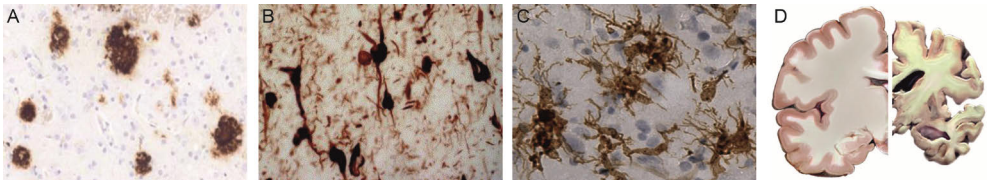

Figure 4. Histopathological view of Alzheimer's disease (AD) neuropathological processes. (A) Aβ plaques. (B) Neurofibrillary tangles (NFTs). (C) Reactive microglia as a sign of neuroinflammation. (D) Neurodegeneration is seen as atrophy in the AD brain (right hemisphere) compared to a healthy brain (left hemisphere). Figure modified from (63) (64) (65) (66).

The expansion of amyloid and tau pathologies in the brain follow different paths (Figure 5). Spreading of NFTs precedes Aβ plaques by years (67) and shows a specific and consistent pattern in neuroanatomically connected regions, which allows differentiating six progressive neuropathological stages of AD, unlike Aβ plaques, which exhibit spreading variations in brain subregions and between individuals, limiting Aβ plaques value in AD pathological staging (68). Moreover, only NFTs' progression pattern and burden correlate with neurodegeneration (69) (70) (71), the severity of cognitive decline and the duration of AD (72).

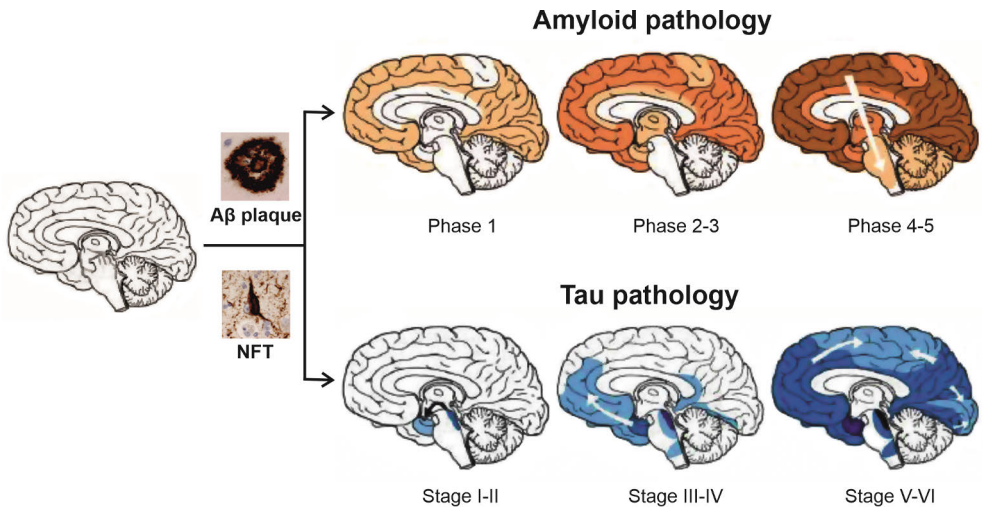

Figure 5. Development of Aβ plaques (phases 1-5) and neurofibrillary tangles (NFTs) (stages I-VI) in Alzheimer's disease (AD). (A) Aβ plaques spread into the neocortex (phase 1), allocortex and hippocampus (phases 2-3), other subcortical structures and cerebellum (phases 4-5). (B) NFTs spread into transentorhinal and entorhinal cortex (stages I-II), hippocampus and associated neocortical areas (stages III-IV), other neocortical areas, including motor and sensory neocortex (stages V-VI). Figure modified from (73) (74).

Aggregation of Aβ

Aβ plaques are protein deposits found predominantly outside the neurons and formed by the accumulation of Aβ peptide fragments as a primary component. Aβ also accumulates into smaller aggregate structures, such as fibrils and oligomers (64). Aβ is a byproduct of APP cleavage (75) and is produced in small concentrations during normal cellular metabolism (76). APP is a transmembrane protein expressed in the plasma membrane and sub-cellular organelles in all tissues (77). No consensus has been made on the exact physiological role of Aβ (76) (78) or APP (64) (79). APP is cleaved via two pathways in the brain. The *non-amyloidogenic* pathway, where APP is cleaved by α- and γ-secretases, and Aβ is not a byproduct of the process. Products of the non-amyloidogenic pathway are considered non-pathologic. On the contrary, in the *amyloidogenic* pathway, APP is cleaved by β- and γ-secretases, and Aβ fragments of varying lengths are produced, of which $A\beta_{42}$ and $A\beta_{40}$ are the two forms associated with AD as they are the most hydrophobic and prone to precipitate in the brain (2) (62) (Figure 6). Mutations in *APP* and γ-secretase catalytic subunits *PSEN1* and *PSEN2* favour amyloidogenic APP cleavage and increase $A\beta_{42}$ production (80). Under normal circumstances, Aβ steady-state level is regulated by clearance across the blood-brain barrier (BBB) in a receptor-mediated process (81) (82) and degradation by enzymatic activity (83) (84). These processes remain active in AD; however, an imbalance emerges between the amyloidogenic Aβ production and Aβ

clearance and degradation. Thus, Aβ starts to aggregate into soluble oligomers, insoluble fibrils and eventually Aβ plaques (2) (62). Based on the amyloid cascade hypothesis, this imbalance is the trigger of all other neuropathological processes in AD, including tau pathology, neuroinflammation, and neurodegeneration (80).

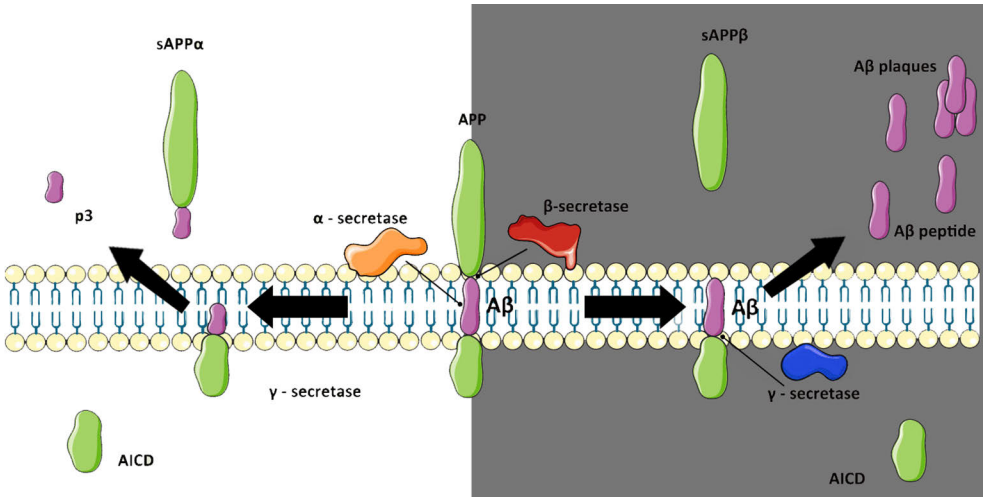

Figure 6. Cleavage pathways of Aβ-precursor protein (APP). In the non-amyloidogenic pathway (left side), APP is cleaved within the Aβ sequence by α- and γ-secretases and Aβ production is prevented. In the amyloidogenic pathway (right side), β- and γ-secretases cleave APP at different locations, which results in the production of Aβ peptides of different lengths to the extracellular domain, where Aβ aggregates as oligomers, fibrils and plaques. Figure modified from (85).

Aggregation of p-tau

NFTs are intracellular protein deposits of p-tau in neuronal soma. Neuropil threads (NTs) are also intracellular deposits of p-tau found in axons and dendrites or dystrophic neurites surrounding neuritic plaques, i.e. intracellular Aβ plaques (86). P-tau also accumulates into smaller aggregate structures, such as fibrils and oligomers. In NFTs and NTs, p-tau is the major component and aggregates primarily as paired helical filaments (PHFs) (87). Interestingly, the structure of tau PHFs varies in different tauopathies, a group of neurodegenerative disorders characterised primarily by tau inclusions, including AD (88). Tau is one of many microtubule-associated proteins located predominantly in the axons (89). Tau is encoded by *MAPT*, and mutations in this gene do not cause AD but instead cause *familial* frontotemporal dementia, often with parkinsonism (90) (91). Tau is expressed as six isoforms that differ by the presence of three (3R) or four (4R) repeats of the microtubule-binding domain (92). In AD, both 3R and 4R tau isoforms are found in PHFs (93). The presence of tau isoforms in tau inclusions varies in different tauopathies; for instance, tau inclusions consist primarily of 3R isoforms in Pick's

disease and 4R isoforms in progressive supranuclear palsy and corticobasal degeneration tauopathies. Whereas similar to AD, tau inclusions are made of both 3R and 4R isoforms in chronic traumatic encephalopathy, sporadic and MAPT-related frontotemporal dementia (88) (94). An established function of tau is promoting the assembly of the microtubules' building blocks, tubulins, and holding the structure of microtubules (95). This role of tau is regulated by its degree of phosphorylation, i.e. the net sum of tau kinases and phosphatases activity (96). Tau hyperphosphorylation has been shown to cause detachment of tau from tubulins, hence the breakdown of neuronal microtubules and the formation of p-tau deposits and neurodegeneration in AD (2) (97) (Figure 7).

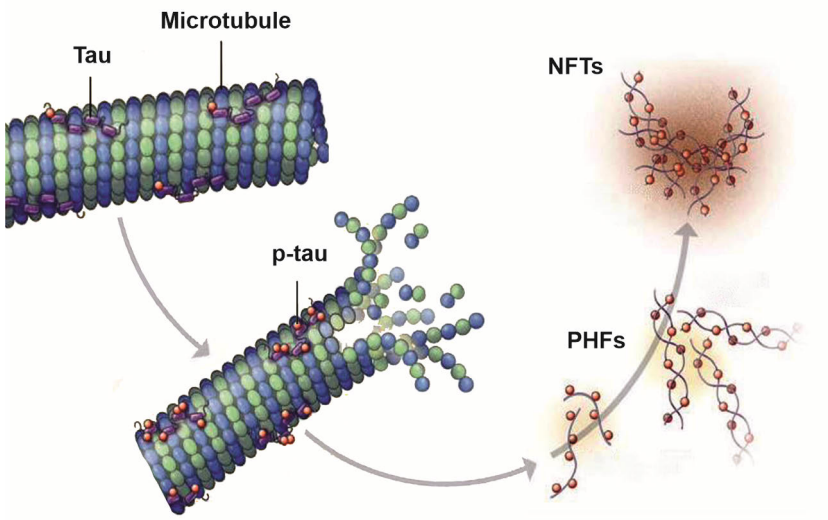

Figure 7. Tau pathology in Alzheimer's disease (AD). Under physiological conditions, tau is sufficiently phosphorylated and binds to microtubules, promoting their stability. In AD, the imbalance in kinase and phosphatase activities and abnormal increase of free tau cause hyperphosphorylated tau (p-tau) to detach from the microtubules, which start to dissociate and p-tau self-aggregate into paired helical filaments (PHFs) and neurofibrillary tangles (NFTs). Figure is modified from (2).

Tau hyperphosphorylation in AD occurs via two mechanisms. First, the imbalance in tau kinases and phosphatases activity as excessive kinase, reduced phosphatase activities or both. Several kinases phosphorylate tau at the microtubule-binding domain, i.e. serine/threonine-proline residue. Other kinases phosphorylate tau at proline-free residues. Tau phosphorylation by some of these kinases makes tau susceptible to more phosphorylation by other kinases (98). Hyperphosphorylation of tau is prevented by dephosphorylation, an activity of phosphatases, of which ~70% is exerted by the protein phosphatase 2A alone (99), which also directly inhibit the

activity of several kinases (100). In AD, tau phosphatase activity is significantly diminished by ~30%, facilitating abnormal tau hyperphosphorylation and aggregation of p-tau (101) (102). Second, abnormal amounts of free tau become available as tau-microtubule bonds break down, due to hyperphosphorylation, especially in the microtubule-binding domain (97) (103). Free tau is more susceptible to hyperphosphorylation than microtubule-bound tau (104), further boosting p-tau aggregation. The tau hypothesis states that aggregation of p-tau precedes and triggers Aβ aggregation and all AD neuropathological changes (105).

Neuroinflammation

Neuroinflammation is the immune response of the central nervous system (CNS), exerted mainly by microglia, astrocytes, and infiltrating immune cells from the periphery when BBB sustains biochemical or mechanical damage (106). Microglia are the CNS-resident and most abundant immune cells. In physiological conditions, microglia play a role in brain development and maintenance of its functional state via neuronal apoptosis and maintenance of synaptic plasticity. The immune function of microglia comprises surveillance of the brain for any abnormalities (106) (107). It is estimated that microglia scan the entire brain volume once every few hours (108). When microglia detect a pathogen, protein aggregates or cell debris, a neuroinflammatory process is initiated to engulf and degrade the stimulus, and typically, microglial reactivity is resolved once the stimulus is eliminated. In neurodegenerative diseases, microglia sustain a reactive state, which gradually turns into a neuropathological process (109) (110) (111). In AD, inclusions of Aβ and p-tau trigger a neuroprotective reaction from reactive microglial, which operate to clear those protein aggregates, limit the extent of ongoing tissue damage, and promote tissue repair. However, the chronic nature of AD forces a continuous neuroinflammatory response from microglia, which subsequently results in reactive microglia suffering structural degradation and compromised functions, becoming neurotoxic and reinforcing the ongoing neuroinflammation in the brain (106) (112) (113). In AD, evidence exists on the correlation between reactive microglia, Aβ, and p-tau inclusions (114). Moreover, reactive microglia load correlates with p-tau inclusions load (115), and reactive microglia closely colocalises with Aβ plaques, indicating an interaction between amyloid pathology and neuroinflammation (116).

Reactive microglia have morphologically reduced branching, resulting in a reduced surveillance area and biochemically different expression profiles of signalling pathways and cell surface markers. Reactive microglia adopt a range of phenotypes depending on their microenvironment, the intensity and type of pathological stimuli, i.e. Aβ or p-tau aggregates, and AD stage (106). The various phenotypes of reactive microglia are categorised in the dual phenotype model: *pro-*

inflammatory (M1) and *anti-inflammatory (M2)* (107) (117). The M1 phenotype plays a crucial role in fighting neuropathological processes. However, it induces damage to healthy neurons and fuels additional neuroinflammation by secreting pro-inflammatory mediators, such as TNF-γ, IL-1β, IL-6, nitric oxide and superoxide. The M2 phenotype plays a central role in tissue repair through secreting anti-inflammatory mediators and growth factors, such as IL-10, TGF-β, nerve growth factor and glial cell-derived neurotrophic factor (Figure 8) (107) (117). The M1 – M2 model is beneficial to demonstrate that reactive microglia under different conditions could be detrimental (M1) or protective (M2). However, the model is also oversimplified, as all reactive microglia phenotypes do not fit strictly in the M1 or M2 categories. Besides, identification markers of pro-inflammatory or anti-inflammatory phenotypes lack specificity (106) (118).

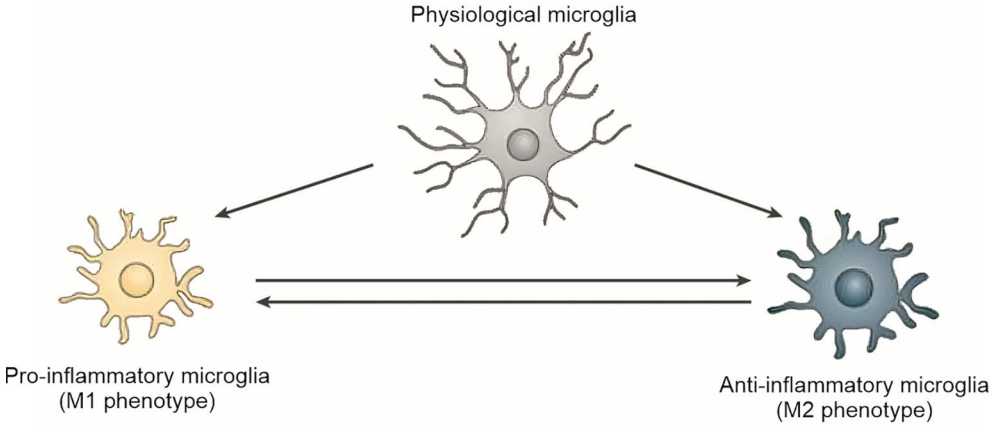

Figure 8. Phenotypes of microglia. Physiological microglia are dynamic and have long and active processes. Reactive microglia are more static and appear different with shorter processes and swollen cell bodies. The M1-M2 model of reactive microglia phenotypes represents a simplified categorization of reactive microglia as pro- or anti-inflammatory. Phenotypes of reactive microglia are many, and some phenotypes do not strictly fit into either category. The same reacted microglial cell can switch between different phenotypes based on the microenvironment. Figure modified from (106) (118).

In addition to microglia, astrocytes contribute to the CNS neuroinflammatory response (119). In physiological conditions, astrocytes regulate cerebral blood flow and maintain neurotransmitter homeostasis. Processes of astrocytes also contribute to the formation of the BBB and synapses (106). Reactive astrocytes communicate with microglia to mediate microglial function (120) and attempt to eliminate pathological triggers, including Aβ and p-tau deposits (106). During neuroinflammation, reactive astrocytes characterised by hypertrophic processes and upregulated expression of glial fibrillary acidic protein (GFAP) induce the harmful A1 or protective A2 phenotypes. In AD, A1 reactive astrocytes are found in

abundance, where their secreted neuroinflammatory mediators induce apoptosis of neurons and disrupt the BBB, which in turn enhances neuroinflammation and other neuropathological processes in AD (106).

Among the primary markers of reactive microglia phenotypes are the translocator protein 18-kDa (TSPO) and purinergic 2 type X subtype 7 (P2X7) receptor (106) (111). In the CNS, TSPO is expressed predominantly in microglia and, to a lesser extent, in astrocytes, but its expression is generally low in the brain under physiological conditions (121). TSPO is located on the outer mitochondrial membrane. The most well-understood function of TSPO is its role in steroid synthesis by transporting cholesterol from the outer to the inner mitochondrial membrane. TSPO is also involved in immunomodulatory response and cellular processes, like proliferation and apoptosis (122) (123). Imaging and histopathological studies reveal that the expression of TSPO is elevated in reactive microglia and astrocytes during AD (124) (125) and that it can be used as an imaging biomarker of neuroinflammation (126).

P2X7 is a cell surface receptor expressed in microglia, astrocytes and other glia such as oligodendrocytes (127). In physiological conditions, P2X7 receptor mediates glial-neuron communication and plays a role in neurotransmitter release. More importantly, P2X7 receptor is involved in the synthesis and secretion of inflammatory mediators and cytokines (128) (129). P2X7 receptor is a ligand-gated ion channel activated by ATP and controls the influx of Na^{+} and Ca^{+2} and the efflux of K^{+} (127). In AD, ongoing tissue damage and neurodegeneration result in increased amounts of extracellular ATP, which leads to abnormal activation of P2X7 receptor and provokes additional neuroinflammation (128) (129). In addition, P2X7 receptor expression and activity are increased in reactive microglia during neuroinflammation, enhancing the overall inflammatory signalling and production of pro-inflammatory mediators, such as IL-1β, TNF-γ, and superoxide (128).

2.1.4 Rodent models of Alzheimer's disease

Rodent models represent a fundamental tool in studying AD neuropathological processes at the cellular and molecular levels. In addition, AD rodent models are routinely used in preclinical development and *in vivo* evaluation of novel PET tracers. Similarly, AD rodent models in drug development are used to validate therapeutic targets and evaluate the efficacy of novel treatments. Over the years, many rodent models of AD neuropathological processes have been developed and validated (130) (131) (132). According to the ALZFORUM research models database, 204 models are available in mice and 17 in rats. These models mimic at least one neuropathological process of AD (133). However, no rodent model presents all features of AD with the same complexity and dynamics seen in humans.

Currently, most AD rodent models listed in ALZFORUM are tg models developed by introducing single or multiple mutated or wild type (wt) human genes, which have a causative relation to *familial* AD. These genes are *APP*, *PSEN1*, and *PSEN2* for amyloid pathology (43) and *MAPT* for tau pathology (90). Depending on the introduced genes, the rodent model mimics primarily amyloid pathology, tau pathology, or both, often associated with neuroinflammation as a secondary neuropathological change. Other pathological changes, such as neurodegeneration and cognitive decline, could be presented in some tg models. However, these are generally less established pathological changes of AD tg rodent models. It must be noted that the current rodent models fail to mimic the late-onset human AD, which represents the vast majority of human AD cases. Instead, rodent models explicitly mimic the early-onset human AD, i.e. *familial* AD, which represents only a minor proportion of the total number of human AD cases. The robustness, onset age and temporal course of neuropathological changes vary among different models, depending on the genetic mutations used and transgene overexpression level in the brain (131). Below is a brief overview of AD tg rodent models. ALZFORUM offers a descriptions of genotype and phenotype characteristics of AD rodent models (133).

Amyloid pathology rodent models

These models have been created by introducing the human *APP*, *PSEN1* or *PSEN2* to the mouse genome. *APP* is the genetic basis of all amyloid pathology rodent models. Mutated *APP* increases Aβ production and/ or aggregation (132), whereas wt *APP* does not phenotype amyloid pathology (131). Several *APP* mutations alone or in combination produce amyloid pathology with different associating secondary neuropathological changes. For instance, the **APP23** and **TgCRND8** mouse models develop Aβ deposits associated with neuroinflammation, moderate p-tau around Aβ plaques but no NFTs, behavioural changes, and some neurodegeneration (131) (132). Mutated *PSEN1* and *PSEN2* increase $A\beta_{42}$ production, which is the most aggregation-prone length of Aβ (131). Rodent models express mutated *PSEN1* or *PSEN2* do not phenotype Aβ deposition. However, when mutated *PSEN1* and *PSEN2* are used in combination with *APP*, the rodent model phenotypes an aggressive amyloid pathology characterised by early onset age and accelerated Aβ aggregation. For example, the **APP/PS1-21** (also known as APPPS1 or $APP_{KM670/671NL}/PS_{L166P}$) mouse model exhibits aggressive deposition of Aβ as early as 1.5-2 months associated with robust neuroinflammation and subsequently p-tau around Aβ plaques but no NFTs (134). The rat model **TgF344-AD** phenotypes the full spectrum of AD neuropathological processes with deposition of Aβ in association with neuroinflammation and cognitive decline at 6 months, followed by NFTs formation and neurodegeneration at 15 months (135).

Tau pathology rodent models

Mutations in *MAPT* cause a decrease in tau interactions with microtubules and promote tau aggregation (136). Thus, mutated *MAPT* has been used to create tg models mimicking tau pathology. For example, the **hTau.P301S** mouse model phenotypes NFTs associated with neuroinflammation, neuronal loss, and cognitive decline in the absence of amyloid pathology (137). In addition, mutated *MAPT* has been incorporated in amyloid pathology tg models to overcome their lack of NFTs and create more representative models of AD, where both AD pathological inclusions, i.e. extracellular Aβ plaques and intracellular NFTs, are present in the same model. In the mouse model **3xTg-AD**, mutated *MAPT*, *APP* and *PSEN1* phenotype Aβ plaques, neuroinflammation, and cognitive decline followed by NFTs after a few months (138).

Models of neuroinflammation

Neuroinflammation, characterised by reactive microglia and astrocytes, is phenotyped in most amyloid and tau pathologies rodent models, due to ongoing pathological changes. Upregulated expression of the neuroinflammatory markers TSPO (139) and P2X7 receptor (140) have been reported in these models. No mutations in genes related to neuroinflammation have a causative relation with *familial* AD. Dedicated neuroinflammation tg models utilising risk genes for late-onset AD, such as **PS19-TREM2^{CV}** have been developed (133). Such models are generated in amyloid or tau tg models and are typically used to investigate the effect of reduced neuroinflammation on ongoing pathologies by suppressing the risk genes (141). Other methodologies than genetic manipulation have been utilised to develop rodent models of AD, for instance, artificially created AD models via intracerebral injections of Aβ or p-tau deposits into the brain. However, these models have significant limitations, such as being extremely invasive, having a high probability of methodological artefacts, and variability of the developed pathologies (142) (143).

2.2 PET imaging in Alzheimer's disease

PET is a nuclear imaging modality that enables quantifiable measurements of molecular targets, biological functions, and pathological processes in humans and animals relatively non-invasively using a PET tracer. In AD, PET imaging can be used to detect and monitor amyloid pathology (4), tau pathology (5), and neuroinflammation (6). Accordingly, the applications of PET imaging in AD scope include investigating neuropathological changes (144), improving diagnosis, and evaluating treatment effects (46) (61). In addition, PET imaging is used in AD drug

development to validate novel targets, assess the efficacy of potential treatments, and improve subject recruitment to clinical trials (143) (145) (146).

2.2.1 The methodology of PET imaging

PET imaging is a sophisticated procedure involving specific preceding steps that must occur in consecutive order. The first step is producing the positron-emitting radionuclide inside a cyclotron. The most commonly used positron-emitting radionuclides in medical imaging are ^{18}F and ^{11}C. This is due to their fast decay, with a half-life of 109.8 minutes for ^{18}F and 20.4 minutes for ^{11}C, and other favourable decay characteristics. Once produced, the radionuclide starts decaying immediately. Therefore, the following steps must be performed with a reasonable speed (147) (148). The second step is synthesising the PET tracer molecules by incorporating the radionuclide into a biologically active molecule. In each PET tracer molecule, the radionuclide accounts for the signal detected by the PET scanner, and the biological molecule accounts for the interaction with the desired biological target. Then comes the PET imaging step, which records the radionuclide decay happening inside the subject lying inside the PET scanner. PET imaging starts simultaneously with the tracer administration to the subject (147) (148).

Radionuclides possess excess protons and, thus, undergo radioactive decay primarily via positron (e^+) emission. Each extra proton decays to a neutron, releasing a positron and a neutrino ($\mathbf{p} \rightarrow \mathbf{n} + \mathbf{e}^+ + \mathbf{v}$). As positrons are emitted, they travel in the tissue for a few millimetres (mm) (maximum 2.4 mm for ^{18}F and 4.1 mm for ^{11}C) restricted by their limited kinetic energy (maximum 634 keV for ^{18}F and 960 keV for ^{11}C). When the positron energy is consumed, it immediately interacts with its nearest antiparticle, i.e. electron (e^-). The e^+/e^- interaction initiates the base event of PET imaging called annihilation, which generates two photons emitted simultaneously in opposite directions. Due to the high energy of photons (511 keV), they can escape the subject body, where they are registered inside the PET scanner by a ring of detectors surrounding the subject (147) (148). The annihilation location is identified after performing mathematical corrections to the registered pair of photons. Unpaired photons due to scattering or random events are discarded. The spatial resolution of PET scanners is typically 4-6 mm for a clinical PET scanner, ~2.5 mm for the human brain dedicated PET scanner (HRRT), and ~1.5 mm for µPET scanner dedicated for small animals. Finally, this data is constructed into three-dimensional (3D) tomographic images, where for each 3D voxel, the intensity of the signal is proportional to the radionuclide amount (Figure 9) (147) (148).

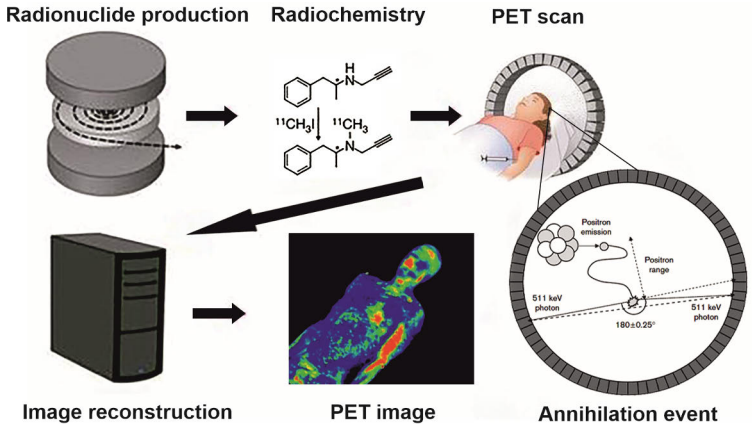

Figure 9. Steps of PET method. First, positron-emitting radionuclides (^{18}F and ^{11}C) are produced inside a cyclotron. Then, radiochemistry, i.e. radiosynthesis of the PET tracer by incorporating the radionuclide within a biologically active molecule. Next, the PET tracer is administered to the subject inside the PET scanner, and the PET imaging procedure begins. A radionuclide, as it decays, releases positrons, which consume their kinetic energy to travel for a few millimetres in the surrounding tissue before colliding with their antiparticles (electrons) in an event called annihilation. An annihilation event results in a pair of 511 keV photons emitted simultaneously in nearly opposite directions, which are detected by the PET scanner detectors. Finally, computational data processing and corrections for artefacts are performed, which result in a constructed three-dimensional PET image of tracer radioactivity distribution. Figure modified from (149) (150) (151).

2.2.2 Development of novel PET tracers

PET tracers are designed to measure biological targets quantitatively, for example, a receptor system, physiological process, or pathophysiological change in a disease state. An essential characteristic of PET tracers is that they are always prepared at non-pharmacological doses, typically in the pico- and femtomoles per gram. Such doses lead to less than 10% target occupancy and do not interfere with the target function or tissue physiology nor produce undesired side effects or toxicity. Moreover, tracer doses result in improved temporal resolution of PET imaging, which reduces the subject's imaging time and radiation exposure (152).

PET tracers are considered radiopharmaceuticals. Therefore, developing a novel PET tracer is similar to a pharmaceutical drug. Below is an overview of tracer development stages tailored for imaging a brain target (153) (154) (155). Tracer development starts with **target validation**, where a biological target with a proven implication in a disease state is identified as a potential target for PET imaging. The next stage is called **hit-to-lead**. A hit is a small chemical molecule or antibody construct with often pre-existing information on its pharmacology, metabolism, physicochemical properties, binding affinity and selectivity to the identified biological target. Hits are often identified by high-throughput screening of compound libraries, re-examining previously developed chemical entities, *in silico*

modelling, or literature search (156). Hits are tested against the biological target in preliminary *in vitro* binding assays, and the most favourable hit based on the available and obtained information is selected as the lead. The next stage is **lead optimisation**, i.e. lead radiochemistry, where a feasible labelling procedure with a radionuclide is established, and radiochemical synthesis with sufficient yield, radiochemical purity, and molar activity (Am, previously named specific activity) is achieved for the lead. After the lead radiochemistry has been established, its evaluation as a novel PET tracer begins.

Although PET tracers are ultimately intended for *in vivo* imaging of biological targets in humans, PET tracers can also bind their targets in *in vitro* settings, which is highly valuable in the early evaluation stages. Tracer development continues with ***in vitro*** **evaluation**. At this stage, *in vitro* binding assays and autoradiography provide valuable information on the binding affinity and selectivity of the tracer towards its target. Nonetheless, the translational value of *in vitro* studies is limited; a novel tracer showing promising *in vitro* results might still fail *in vivo*. Therefore, if general requirements are fulfilled and no obvious limitations appear in *in vitro* settings, it is recommended that tracer development proceed to **preclinical evaluation**, i.e. *in vivo* and *ex vivo* studies in animal models. A PET tracer must be biocompatible and nontoxic, both aspects are typically investigated at the preclinical stage in toxicity and dosimetry studies (155). In addition, typically performed studies at this stage include *in vivo* or *ex vivo* biodistribution, *in vivo* PET and *ex vivo* autoradiography imaging with and without pre-treatment, metabolism and radiometabolites analysis. These studies combined establish the pharmacokinetics profile, i.e. ADME, and binding properties of the novel PET tracer.

All the obtained findings of tracer development up to this stage should be sufficient to answer the question: *Is this novel PET tracer suited for clinical evaluation in humans?* There is no clear-cut answer to this question, and the case of each tracer must be carefully assessed to present a balanced risk-benefit evaluation to the medical ethics committee and regulatory authority to approve the clinical evaluation stage. While many novel PET tracers reach clinical evaluation, most do not progress to authorised clinical use, due to having suboptimal binding properties and/ or pharmacokinetics profile, ADME. Over the years, many PET tracers have been developed to image different targets in the brain. Based on the successful and unsuccessful experiences, a set of development requirements were introduced to assess the pharmacokinetic and binding properties of a novel PET tracer (155) (156) (157) (158) (159) (160) (161). Following is a brief overview of these requirements.

Binding affinity and selectivity: The PET tracer should possess sufficient binding affinity and selectivity to its target. Binding affinity is expressed as the equilibrium dissociation constant (K_d), which in molar units refers to the ligand concentration needed to occupy half of the target binding sites, i.e. 50% occupancy.

Generally, Kd ≤ 1 nM has been an acceptable affinity range for a PET tracer. However, deviations from this rule could be made, as binding affinity directly depends on the target concentration in the tissue. On the other hand, binding selectivity means that the tracer binds its target without significant non-specific binding to molecules other than its target. Specific *in vivo* binding translates to a high signal-to-noise ratio in PET images, which is crucial for target visualisation (157).

Absorption and distribution: The first requirement of any PET tracer is to have sufficient target reachability and concentration to the tissue where its target is located. For a target in the brain, the tracer needs to penetrate the BBB. Small chemical molecules (molecular weight < 700 Da) that are sufficiently lipophilic ($LogD_{7.4}$ = 1-3) tend to pass through the BBB efficiently via passive diffusion (157). Insufficiently lipophilic tracers suffer from poor passage across the BBB, whereas highly lipophilic tracers exhibit high non-specific binding in brain tissue, plasma proteins, and metabolic enzymes (162). Characterising tracer binding to plasma proteins is necessary because that reveals the fraction of the tracer which is not bound to plasma protein in the vascular system and is available for target engagement (159) (163) (164).

Metabolism: The tracer must be metabolised at a reasonable speed, have low non-specific binding in the target organ, and have fast clearance from the blood. Only then will the measured radioactivity mirror specific binding. The time the tracer circulates with the blood is determined by its metabolic stability, i.e. tracer degradation, presence of radiometabolites, and excretion speed. For a PET tracer, it is essential to quantify the actual fractions of unchanged tracer and radiometabolites because PET as a method detects annihilation events of all positrons and is unable to differentiate if the detected signal originates from the unchanged tracer or its radiometabolites. Thus, BBB-penetrating radiometabolites disturb the analysis of PET data in the brain, for example, uptake and specific binding, and demand more sophisticated quantification methods that include a correction for radiometabolites and pharmacokinetic modelling. Also, understanding tracer metabolism and protein-free fraction enables the determination of actual input from the vascular system to the brain (158).

Excretion: The tracer should reversibly bind its desired target, reach equilibrium, and clear from the body in a reasonable time. Depending on its lipophilicity, a tracer is excreted through two pathways: hydrophilic renal excretion via the kidneys and lipophilic hepatobiliary excretion via the liver. Generally, the way the body metabolises a PET tracer reduces its lipophilicity, which in turn helps in renal excretion and produces radiometabolites that are more hydrophilic and less able to penetrate the BBB (165).

2.2.3 PET tracers for imaging tau pathology

Many PET tracers divided broadly into two generations have been developed for imaging tau pathology in AD. Below are the main findings from the development of each tracer. **[^{18}F]FDDNP** was the first tracer ever to image NFTs in AD. The tracer showed uptake in brain regions with NFTs that was higher in the brains of individuals with AD and MCI than in healthy subjects. However, clinical development of [^{18}F]FDDNP revealed a lack of binding selectivity to NFTs, as the tracer also showed high uptake in brain regions with Aβ plaques and insufficient binding affinity for both NFTs and Aβ plaques *in vivo* (166). Clinical evaluation revealed major metabolic instability for the tracers **[^{11}C]PBB3** and **[^{18}F]T808** represented by very fast metabolism and brain-penetrating radiometabolites for [^{11}C]PBB3 (167) and substantial defluorination, i.e. the dissociation of the radionuclide ^{18}F from the tracer molecule for [^{18}F]T808 (168). To date, **[^{18}F]AV1451** (also known as [^{18}F]T807 or flortaucipir) is the only tau PET tracer approved by the Food and Drug Administration (FDA), but not the European Medicines Agency (EMA) for clinical use in individuals with cognitive impairment and suspected AD (20). [^{18}F]AV1451 exhibited high binding affinity to p-tau deposits and selectivity over Aβ plaques on AD brain sections in *in vitro* autoradiography. In individuals with AD, the tracer showed high uptake in brain regions of high NFT load and low non-specific white matter binding. Moreover, [^{18}F]AV1451 showed a strong association with the severity of cognitive impairment and neurodegeneration, and the amount and brain area of tracer uptake was higher in individuals with severe AD than those with mild AD or MCI (166) (167) (168). A major disadvantage of [^{18}F]AV1451 is its off-target binding in brain regions that lack tau pathology in AD, such as the mid-brain substantia nigra, choroid plexus, meninges, and striatum (167).

THK tracers ([^{18}F]THK523, [^{18}F]THK5105, [^{18}F]THK5117, (*S*)-[^{18}F]THK5117, [^{18}F]THK5351) were the most novel tracers developed to image tau pathology at the start of this thesis work. THK tracers were identified from high-throughput screening of β-sheet-binding small molecules. **[^{18}F]THK523** was the first evaluated tracer in this series and showed higher binding affinity to p-tau deposits than Aβ plaques in *in vitro* autoradiography. Preclinical evaluation in tau pathology tg mice showed higher tracer uptake than in wt control mice. However, in clinical evaluation, [^{18}F]THK523 failed to visualise p-tau deposits in the AD brain as the tracer showed higher non-specific binding in white matter than a specific binding in grey matter (167). **[^{18}F]THK5105** and **[^{18}F]THK5117** were then developed to improve the *in vivo* binding properties to p-tau deposits. Both tracers showed improved binding affinity to p-tau deposits by differentiating individuals with AD from healthy subjects, and tracers uptake correlated with cognitive decline (167). Compared to [^{18}F]THK5105, [^{18}F]THK5117 showed a better pharmacokinetics profile (168). Clinical evaluation was then continued with the (*S*)-enantiomer of [^{18}F]THK5117,

(*S*)-[^{18}F]THK5117 (also known as [^{18}F]THK5317), which demonstrated the same improved *in vivo* binding properties, and preferable pharmacokinetics profile, mainly improved signal-to-background ratio, due to faster clearance from the blood and brain. However, a non-negligible white matter binding remained an issue with these tracers, which complicates the interpretation and analysis of *in vivo* tracer binding seen in PET images (166) (167). **[^{18}F]THK5351** was then developed and showed reduced *in vivo* non-specific white matter binding and improved specific binding in brain regions with p-tau deposits compared to (*S*)-[^{18}F]THK5117, which also correlates with cognitive decline and neurodegeneration (167). Despite the improved *in vivo* binding, [^{18}F]THK5351 exhibited high uptake in the subcortical regions thalamus, basal ganglia, and midbrain, due to non-specific binding to monoamine oxidase B (MAO-B) enzyme. A drawback common to the other THK tracers, as revealed by additional studies. With that, the development of the THK tracers series concluded that, due to the limited *in vivo* binding selectivity, these tracers have limited utility for imaging tau pathology in AD (167) (169).

The second-generation tau tracers were developed to overcome the first-generation tracers' suboptimal binding selectivity and pharmacokinetic limitations. [^{18}F]PI-2620 and [^{18}F]RO-948 were developed based on the chemical structure of [^{18}F]AV1451. [^{18}F]GTP-1 was developed based on [^{18}F]T808, and [^{18}F]PM-PBB3 based on [^{11}C]PBB3. Meanwhile, [^{18}F]MK-6240 and the analogues [^{18}F]JNJ-067 and [^{18}F]JNJ-311 are novel molecules (169). Collectively, *in vitro* binding assays and autoradiography of the second-generation tau tracers clearly showed high specific binding to p-tau deposits and absence of non-specific binding to Aβ plaques, MAO-B or MAO-A enzymes (167) (170) (171) (172). The most advanced and promising development has been with **[^{18}F]PI-2620**. The tracer showed an excellent pharmacokinetics profile with fast brain uptake, clearance from non-target regions, and no indications of brain-penetrating radiometabolites in preclinical (170) and clinical (173) evaluations. In individuals with AD, [^{18}F]PI-2620 uptake was significantly high in brain regions of p-tau deposits, and tracer uptake appears to achieve the Braak staging of tau pathology *in vivo* in AD (174). [^{18}F]PI-2620 also seem to have the potential to image p-tau deposits in non-AD tauopathies (175). **[^{18}F]RO-948** (167) and **[^{18}F]GTP-1** (172) (176) showed suitable pharmacokinetics profiles without brain-penetrating radiometabolites and specific binding in brain regions with p-tau deposits in individuals with AD. The development of other second-generation tau tracers has been less positive. In the case of **[^{18}F]MK-6240**, despite the moderate pharmacokinetics profile and binding affinity to p-tau deposits in individuals with AD, the tracer showed substantial non-selective binding in neuromelanin-containing neurons in midbrain and melanin-containing cells, and defluorination in preclinical evaluation (171). The development of **[^{18}F]JNJ-067** and **[^{18}F]JNJ-311** revealed limitations with *in vivo* binding selectivity and

pharmacokinetics profile. Warranted additional studies, preliminary evaluation of **[^{18}F]PM-PBB3** (also known as [^{18}F]-APN-1607 or florzolotau) showed suitable binding properties and pharmacokinetics profile (177) (178).

The feasibility of amyloid PET imaging in AD drove and contributed to developing PET tracers for imaging tau and glia (discussed below). The development of PET tracers for imaging amyloid pathology is a broad research area and extends beyond the scope of this thesis (reviewed in (19) (179) (180)). However, it is worth noting that the availability of PET tracers for imaging amyloid pathology preceded that of tau by years. Currently, the PET tracers [^{18}F]flutemetamol, [^{18}F]florbetaben and [^{18}F]florbetapir are approved by the FDA and EMA for clinical use (19).

2.2.4 PET tracers for imaging P2X7 receptor

To date, there are no PET tracers approved by the FDA or EMA for imaging neuroinflammation in the brain. Few PET tracers have been developed for imaging P2X7 receptor and underwent preclinical and clinical evaluation. **[^{11}C]A-740003** was the first tracer developed to image P2X7 receptor. The preclinical evaluation revealed poor BBB penetration and brain uptake of the tracer (181). **[^{18}F]EFB** also showed the same limitation (182). **[^{11}C]GSK1482160** showed to bind human P2X7 receptor with high affinity in *in vitro* binding assays (183). Preclinical evaluation in rodent models of induced neuroinflammation revealed *in vivo* and *ex vivo* tracer uptake into mice brains (184) but not rats brains, due to the low [^{11}C]GSK1482160 binding affinity to rat P2X7 receptor (183). [^{11}C]GSK1482160 also showed to cross the BBB in non-human primates (183). Clinical evaluation of [^{11}C]GSK1482160 in healthy subjects revealed low brain uptake, indicating that the tracer is unsuitable for further clinical evaluation (185). Subsequently, **[^{11}C]I-GSK1482160**, **[^{11}C]Br-GSK1482160** (186), **[^{18}F]IUR-1601** (187), **[^{18}F]IUR-1602** (188), and **[^{123}I]TZ6019** (189) were developed based on GSK1482160. However, *in vitro* evaluation of those tracers has not been encouraging, due to suboptimal binding properties and/ or radiochemistry.

The development of **[^{11}C]JNJ54173717** and **[^{18}F]JNJ-64413739** produced similar findings. Both tracers demonstrated high *in vitro* binding affinity to human P2X7 receptor (190) (191). The preclinical evaluation revealed higher [^{11}C]JNJ54173717 (190) and [^{18}F]JNJ-64413739 (192) uptake in the rat brain compared to controls, where the expression of human and endogenous P2X7 receptor is upregulated, which was also confirmed with autoradiography. In addition, the binding specificity of both tracers was also demonstrated by *in vivo* blocking of P2X7 receptor using chemically distinct receptor ligands, which resulted in significantly reduced tracer uptake (190) (192). Both tracers showed suitable pharmacokinetics profiles in rats. In non-human primates, [^{11}C]JNJ54173717

showed suitable brain uptake and clearance (190), whereas [^{18}F]JNJ-64413739 demonstrated high non-specific binding (191). Subsequently, in clinical evaluation, [^{18}F]JNJ-64413739 brain uptake in healthy subjects showed high between-subject variability (193). [^{11}C]JNJ54173717 also produced similar variability and failed to differentiate individuals with Parkinson's disease or Amyotrophic lateral sclerosis from healthy subjects (194) (195).

[^{11}C]SMW139 was the most recently developed tracer for P2X7 receptor imaging at the start of this thesis work. Similar to the previous tracers, *in vitro* and preclinical evaluations showed promising findings, where [^{11}C]SMW139 demonstrated suitable binding affinity to human and rat P2X7 receptors (196). In rats, [^{11}C]SMW139 showed no abnormalities in peripheral biodistribution, predominant hepatobiliary excretion, BBB penetration, and moderate metabolic stability, despite the presence of BBB-penetrating radiometabolites (197). Regarding brain uptake, [^{11}C]SMW139 demonstrated high *in vivo* binding to human P2X7 receptor overexpressed in rat striatum. Binding to P2X7 receptor was also confirmed by *in vitro* autoradiography (197). Moreover, selective binding of [^{11}C]SMW139 was demonstrated by *in vitro* and *in vivo* blocking of P2X7 receptor (197). Nonetheless, in *in vitro* autoradiography, [^{11}C]SMW139 binding was similar on brain sections from individuals with AD and healthy subjects, despite the increased expression of P2X7 receptor in the AD tissue. [^{11}C]SMW139 also demonstrated higher binding in white matter than in grey matter in both brain sections (197). These findings suggested that AD might not be the ideal neurodegenerative disease for [^{11}C]SMW139 clinical evaluation (197), and the tracer evaluation was shifted to Multiple Sclerosis (MS) based on the findings that P2X7 receptor expression is strongly upregulated in the brain sections of individuals with MS and brain of MS rat model (198). In line with these findings, [^{11}C]SMW139 showed significantly higher brain uptake in MS rat model compared to control rats. Tracer uptake was also specific, as demonstrated by *in vitro* and *in vivo* blocking of P2X7 receptor (196). [^{11}C]SMW139 was then evaluated in a small set of individuals with MS and healthy controls. The tracer showed higher brain uptake in the MS group (199), with the assumption that [^{11}C]SMW139 brain-penetrating radiometabolites detected in rats (197) do not penetrate the human brain. Subsequently, it was revealed that [^{11}C]SMW139 metabolism produces three similar radiometabolites in healthy human subjects and mice, two of which have also been detected in mice brains, concluding that correction for BBB-penetrating radiometabolites is critical for correct [^{11}C]SMW139 *in vivo* quantification (200). In conclusion, [^{11}C]SMW139 clinical evaluation is yet to reveal the potential of the tracer to image P2X7 receptor in individuals with neurodegenerative diseases.

3 Aims

The aim of this thesis was to evaluate PET tracers designed to image p-tau inclusions and reactive glia. Another aim was to assess the suitability of the APP/PS1-21 mouse model of Aβ deposition for preclinical development of PET tracers by evaluating the availability of the investigated imaging targets.

The following specific objectives were set for each study in this thesis:

I. To investigate the *in vivo* binding selectivity of the p-tau inclusions targeting tracer, (*S*)-[^{18}F]THK5117, in relation to Aβ plaques and MAO-B enzyme, and assess the pharmacokinetic properties of (*S*)-[^{18}F]THK5117 in the APP/PS1-21 mouse model.

II. To image neuroinflammatory reactive glia in the APP/PS1-21 mouse model longitudinally with [^{11}C]SMW139 targeting P2X7 receptor, compare the uptake of [^{11}C]SMW139 to that of [^{18}F]F-DPA targeting TSPO in the same mice, and assess the pharmacokinetic properties of [^{11}C]SMW139.

III. To study metabolism and radiometabolite formation of [^{11}C]SMW139, and plasma protein binding of the tracer and its radiometabolites in mice to better understand the pharmacokinetic properties of [^{11}C]SMW139.

4 Materials and Methods

4.1 Studies experimental design (I-III)

Preclinical evaluation of the PET tracers was performed using *in vivo* PET imaging (**I**,**II**), accompanied with various *ex vivo* experiments (**I-III**) to validate the PET imaging findings. In study **I**, evaluation of (*S*)-[^{18}F]THK5117 was performed using a cross-sectional *in vivo* PET imaging experimental design. Different tg and wt control mice were used at the time points 2-3, 6-7, 12-16 and 19-26 months (Figure 10). Each mouse served as an experimental unit, and the primary outcome was the group difference in (*S*)-[^{18}F]THK5117 uptake between tg and age-matched wt mice in brain regions affected by Aβ deposition at each time point. Changes in (*S*)-[^{18}F]THK5117 *in vivo* uptake and *ex vivo* binding on brain tissue sections were compared to the immunohistochemical quantifications of potential tracer binding targets p-tau, Aβ plaques, and MAO-B enzyme. Also, an imaging experiment after MAO-B enzyme *in vivo* blocking was performed to further validate (*S*)-[^{18}F]THK5117 binding selectivity. (*S*)-[^{18}F]THK5117 metabolism in plasma and brain, and biodistribution to the brain and peripheral organs were also evaluated.

In study **II**, a longitudinal *in vivo* PET imaging experimental design was used. The same tg and wt mice were imaged with [^{11}C]SMW139 at 5, 8, 11 and 14 months, and with [^{18}F]F-DPA only at 14 months (Figure 10). In this study, experimental units were each mouse both as an individual repeatedly imaged, and as a group member imaged at a defined time point. [^{11}C]SMW139 *in vivo* uptake change with ageing was investigated in brain regions with microglial reactivity due to Aβ deposition, where the primary outcome was the longitudinal difference in [^{11}C]SMW139 uptake between the baseline and the follow-up scans in tg and wt mice as individuals and groups. [^{11}C]SMW139 *in vivo* uptake in comparison to [^{18}F]F-DPA uptake was investigated with the group difference in [^{11}C]SMW139 and [^{18}F]F-DPA uptake between tg and age-matched wt mice being the primary outcome. [^{11}C]SMW139 *in vivo* uptake and *ex vivo* binding on brain tissue sections were compared to the immunohistochemical quantifications of P2X7 and P2Y12 receptors expression, whereas [^{18}F]F-DPA *in vivo* uptake was compared to TSPO expression. Therefore, study **II** was a continuation of study **I** with regard to the animal model assessment in terms of evaluating the availability of imaging targets. [^{11}C]SMW139 metabolism in

plasma and brain, and biodistribution to the brain and peripheral organs were evaluated.

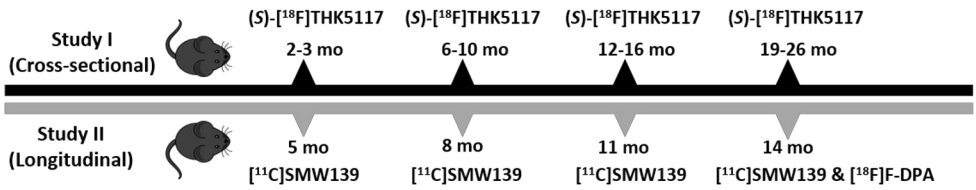

Figure 10. *In vivo* PET imaging design in studies I-II. mo: months.

In study **III**, [^{11}C]SMW139 metabolism was thoroughly investigated using wt mice only. Unchanged [^{11}C]SMW139 and radiometabolite fractions, and the number of radiometabolites were analysed in mouse plasma and brain by radio-thin-layer chromatography (RadioTLC). In addition, protein-free fractions of unchanged [^{11}C]SMW139 and radiometabolites in plasma available for brain uptake were quantified by plasma protein binding (PPB) analysis. Each animal served as an experimental unit. Fractions of unchanged [^{11}C]SMW139 and its radiometabolites in plasma and brain, as well as protein-free fractions of [^{11}C]SMW139 and its radiometabolites in plasma served as the primary outcomes. Table 1 illustrates experiments in studies **I-III**.

Table 1. Experiments performed in studies I-III.

Study	IHC	*in vivo* PET imaging			*ex vivo* experiments			
		Cross	Blocking	Long	Brain ARG	Biodistribution	RadioTLC	PPB
I	x	x	x		x	x	x	
II	x			x	x	x	x	
III							x	x

Abbreviations: IHC: immunohistochemistry, Cross: cross-sectional, Long: longitudinal, ARG: autoradiography, RadioTLC: radio-thin-layer chromatography, PPB: plasma protein binding.

4.2 Experimental animals

All animal procedures were approved by the Regional State Administrative Agency for Southwestern Finland (Licenses ESAVI/ 4660/ 04.10.07/ 2016 and ESAVI/ 16273/ 2019). All studies were performed in accordance with the ARRIVE guidelines (201) and the EU Directive 2010/63/EU on the protection of animals used for scientific purposes. Additionally, all studies adhered to the 3Rs principle

(Replacement, Reduction, and Refinement) by utilising the same PET imaged mice for *ex vivo* experiments (**I**) if and when feasible, utilising the same mouse in as many *ex vivo* experiments as possible (**I-III**) and employing a longitudinal PET imaging design (**II**). Each three to four mice of the same gender were group-housed in individually ventilated cages in the Central Animal Laboratory at the University of Turku under the following controlled housing conditions: 12-hour light cycle (7:00 to 19:00 light), temperature 21℃ (3℃), humidity 55% (15%) and aspen wood bedding. Soy-free chow (RM3 (E) Soya Free, Special Diets Service, Essex, UK) and tap water were available *ad libitum*. Animals' well-being adhered to the ethical principles of the International Council of Laboratory Animal Science (ICLAS).

4.2.1 APP/PS1-21 mouse model (I,II)

The APP-PS1-21 is a mouse model of Aβ deposition. This model expresses the human KM670/671NL-mutated *APP* and L166P-mutated *PSEN1* driven by the neuron-specific mouse Thy1 promoter (134). These mutations phenotype aggressive Aβ deposition in this model starting at 6 weeks in the neocortex and progressing from there to the hippocampus, thalamus and other cortical brain regions. By the age of 8 months, the entire forebrain is covered with Aβ plaques, and the size and quantity of the plaques increase with ageing (134). Aβ deposition is associated with robust neuroinflammation characterized by increased reactive microglia and astrocytes around the plaques, and subsequently subtle presence of p-tau but no NFTs (134). The APP/PS1-21 mouse model colony (KÖESLER, Rottenburg, Germany) was bred and maintained with C57BL/6Cn wt mice. Breeding litters consisted of both AD-diseased heterozygote tg and healthy wt mice. The genotype, i.e. tg or wt, was confirmed by immunohistochemical (IHC) staining of Aβ plaques after the mice were sacrificed. In studies **I-II**, the APP/PS1-21 mouse model was utilized at various time points, from 2 to 26 months.

4.2.2 Wild type animals (I-III)

The wt littermates of tg mice (C57BL/6Cn background) and additional C57BL/6NRj wt mice (Janvier Labs, Le Genest-Saint-Isle, France) were used as age-matched controls for the tg mice in the *in vivo* imaging and *ex vivo* experiments.

4.3 Synthesis of PET tracers (I-III)

^{18}F and ^{11}C radionuclides were produced in the nuclear reactions ^{18}O (p,n) ^{18}F and ^{14}N (p,α) ^{11}C, respectively, using the CC-18/9 cyclotron (Efremov Scientific Institute of Electrophysical Apparatus, St. Petersburg, Russia) at the Accelerator Laboratory

of Turku PET Centre. The radiotracers (*S*)-[^{18}F]THK5117 (202), [^{11}C]SMW139 (203), and [^{18}F]F-DPA (204) (Figure 11) were synthesized at the Radiopharmaceutical Chemistry Laboratory of Turku PET Centre as described in the original publications. Description of tracer batches (**I-III**) are presented in Table 2.

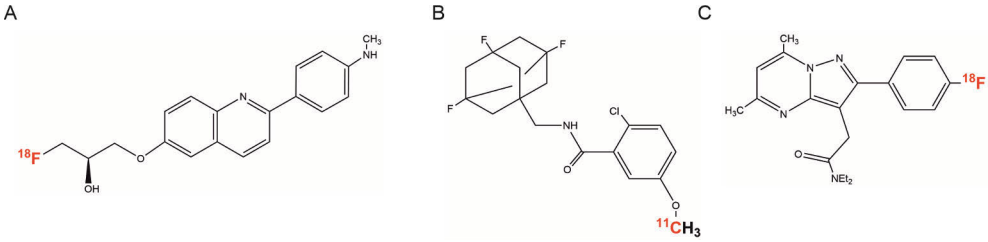

Figure 11. Chemical structures of PET tracers used in studies I-III. (A) **(*S*)-[^{18}F]THK5117** (6-[(3-[^{18}F]fluoro-2-hydroxy)propoxy]-2-(4-methylaminophenyl)quinoline), (B) **[^{11}C]SMW139** (2-chloro-5-[^{11}C]methoxy-N-((3,5,7-trifluoroadamantan-1-yl)methyl)benzamide) and (C) **[^{18}F]F-DPA** (N,N-diethyl-2-(2-(4-([^{18}F]fluoro)phenyl)-5,7 dimethylpyrazolo[1,5-a]pyrimidin-3-yl)acetamide).

Table 2. Radiotracer batches used in studies I-III. Values presented as mean (standard deviation).

Study	I	II		III
Radiotracer(s)	(*S*)-[^{18}F]THK5117	[^{11}C]SMW139	[^{18}F]F-DPA	[^{11}C]SMW139
n	11	32	3	27
Am_{EOS} (GBq/μmol)	-	91 (41)	9 (0.8)	110 (49)
Am_{Inj} (GBq/μmol)	840 (410)	33 (21)	3.2 (0.6)	37 (27)
Injected mass (μg/kg)	0.15 (0.09)	6.06 (5.61)	22.5 (4.32)	8.3 (6.9)
Yield (%)	11 (5)	24.3 (2.8)	7.9 (1.7)	-
Radiochemical purity (%)	> 98%	98.3 (0.5)	> 99%	98.3 (0.5)
Shelf-life (h)	6	1	> 4	1

Abbreviations: *n*: number of produced batches, Am_{EOS}: molar activity at end of synthesis, Am_{Inj}: molar activity at injection, GBq: gega Becquerel, h: hour.

4.4 *In vitro* methods (I,II)

4.4.1 Immunohistochemistry

IHC staining was performed to investigate the expression of imaging targets and their change with ageing in tg and wt mice. In study **I**, IHC staining on fixed-frozen brain sections was used to assess p-tau, Aβ plaques, and MAO-B enzyme-using a

separate group than the PET imaged mice, which allowed for the more time-consuming perfusion fixation procedure, as mice were not used in subsequent *ex vivo* experiments. Additionally, fresh-frozen brain sections collected from the mice used in the MAO-B enzyme *in vivo* blocking experiment were used for Aβ plaques and MAO-B enzyme IHC staining. In study **II**, staining was performed to assess the expression of TSPO, P2X7, and P2Y12 receptors on the same sections used in the *ex vivo* brain autoradiography experiment, which prevented the perfusion fixation procedure; instead, sections were post-fixed at the start of the staining procedure (Table 3).

Table 3. Description of mice counts in studies I and II.

Study	**I**			**II**		
	Aβ	**p-tau**	**MAO-B**	**P2X7**	**TSPO**	**P2Y12**
n tg (female)	17* (7)	12 (7)	17*(7)	7 (4)	15 (7)	
n wt (female)	5 (3)	5 (3)	5 (3)	5 (0)	12 (6)	
Age groups (months)	3, 7-9,10*,11-14,23			5,8-10,12,14,15		

*****including the 5 male mice used in the MAO-B enzyme *in vivo* blocking experiment
Abbreviations: *n*: number of mice, tg: transgenic, wt: wild type, Aβ: β-amyloid peptides, p-tau: Hyperphosphorylated tau, MAO-B: Monoamine oxidase B enzyme, TSPO: Translocator protein 18-kDa, P2X7: Purinergic 2 type X subtype 7 receptor, P2Y12: Purinergic 2 type Y subtype 12 receptor.

20 µm-thick coronal brain sections used in *ex vivo* brain autoradiography experiment (described below in section 4.6.1) and stored afterwards at -40°C for staining were used. Consecutive (**I**) and non-consecutive (**II**) sections of the same mouse went through antigen retrieval with formic acid (p-tau, Aβ plaques, MAO-B enzyme) or citrate buffer (TSPO, P2X7 and P2Y12 receptors). Endogenous hydrogen peroxidase enzyme was blocked with hydrogen peroxide in a methanol solution, and background proteins were blocked with a blocking solution. Sections were then incubated with the primary antibody (Table 4), followed by an incubation with the corresponding secondary antibody. The staining detection system was developed by the consecutive incubations in avidin-biotin-peroxidase complex and DAB substrate (p-tau, Aβ plaques, MAO-B enzyme), or only in DAB substrate (TSPO, P2X7 and P2Y12 receptors). Staining protocols of all imaging targets are described in the original publications. IHC staining of p-tau, Aβ plaques, and MAO-B enzyme was performed manually in the Medicity Research Laboratory, University of Turku. HistoCore (University of Turku) performed IHC staining of Aβ plaques and MAO-B enzyme (blocking experiment), TSPO, P2X7, and P2Y12 receptors using the semi-automated Labvision autostainer (Thermo-Fisher Scientific, Vantaa, Finland).

Table 4. Staining type and primary antibodies used in studies I and II.

Study	Imaging target	1ry Ab	Immunogen	Origin/ Cat
I	Aβ	6E10	$Aβ_{1-16}$	Covance Inc./ SIG-39320
	p-tau	AT8	Phosphorylated Ser202 on PHF-Tau	Thermo Fisher Scientific/MN1020
	MAO-B	Anti-MAOB	MAO-B epitope signature tag	SIGMA /HPA002328
II	P2X7	Anti-P2X7	amino acids 136-152 of mouse P2X7	APR-008
	TSPO	Anti-PBR	Human PBR aa 150 to the C-terminus	EPR5384
	P2Y12	Anti-P2Y12	C-terminus of mouse P2Y12	AS-55043A

Abbreviations: Aβ: β-amyloid peptides, p-tau: Hyperphosphorylated tau, MAO-B: Monoamine oxidase B enzyme, TSPO: Translocator protein 18-kDa, P2X7: Purinergic 2 type X subtype 7 receptor, P2Y12: Purinergic 2 type Y subtype 12 receptor, 1ry Ab: primary antibody, Cat: catalog #.

IHC-stained sections were digitized using the Panoramic 250 Flash slide scanner (3DHistech, Hungary). Section images were captured with Case Viewer v. 2.1 (3DHistech). Quantification of imaging targets in tg and wt mice was performed by manually drawing a region of interest (ROI) for thalamus (THA) on both brain hemispheres and cortex (CTX) on one hemisphere (**I**, **II**) using two sections/mouse (Figure 12A). Imaging targets were quantified as positive objects/mm^2 using two different methods. The amount of p-tau, Aβ plaques, TSPO and P2Y12 receptor were quantified as the count of 6E10, AT8, anti-PBR and anti-P2Y12-positive objects/mm^2 using the positive cell detection function in QuPath (205) (Queen's University, Belfast, Northern Ireland). Whereas the more demanding quantification of P2X7 receptor as the count of anti-P2X7-positive objects/mm^2 was performed by Turku BioImaging (University of Turku) using the artificial intelligence object detection algorithm You Only Learn One Representation (YOLOR) (206) implemented in Python. No MAO-B enzyme quantification was performed.

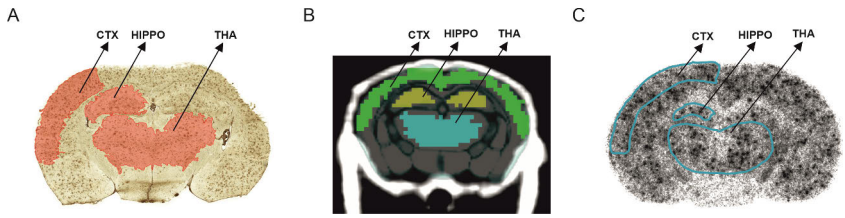

Figure 12. Representative view of image data analyses for the same brain regions from (A) immunohistochemical staining, (B) *in vivo* PET/ CT imaging and (C) *ex vivo* brain autoradiography. CTX: cortex, HIPPO: hippocampus, THA: thalamus.

4.5 *In vivo* PET imaging (I,II)

In vivo dynamic PET/ computed tomography (CT) scans (**I**,**II**) were conducted using the small animal Inveon Multimodality PET/CT device (Siemens Medical Solutions, Knoxville, TN, USA). According to the manufacturer, this scanner offers a 12.7 cm axial and 10 cm transaxial field-of-view, approximately 1.5 mm spatial resolution of the PET camera and 10% sensitivity in the centre of the field-of-view. The imaging workflow was conducted with two mice at a time. Mice were anaesthetized with an inhaled mixture of isoflurane/O_2 (induction ~4%, maintenance ~2.5%) and cannulated in the lateral tail vein, via which the tracer injection was administered. Imaging started with the CT scan for attenuation correction of the PET data and anatomical referencing in PET image analysis. Then, just after an intravenous bolus injection of the tracer (up to 200 µL) started with the first animal, dynamic PET recordings in 3D list mode were initiated. Tracer injections were flushed with physiological saline (10-20 µL) to ensure the whole tracer injection passed from the cannula. Raw PET data were recorded for 40 minutes (min) after (*S*)-[^{18}F]THK5117 injection (**I**) and 60 min after [^{11}C]SMW139 and [^{18}F]F-DPA injections (**II**) with an energy window of 350-650 keV. After (*S*)-[^{18}F]THK5117 scans, mice were sacrificed for *ex vivo* experiment, whereas after [^{11}C]SMW139 and [^{18}F]F-DPA scans, mice were returned to their cages for longitudinal imaging and separate mice were used for *ex vivo* experiment (Figure 13). PET imaging protocol and mice count in studies I-II are presented in Table 5.

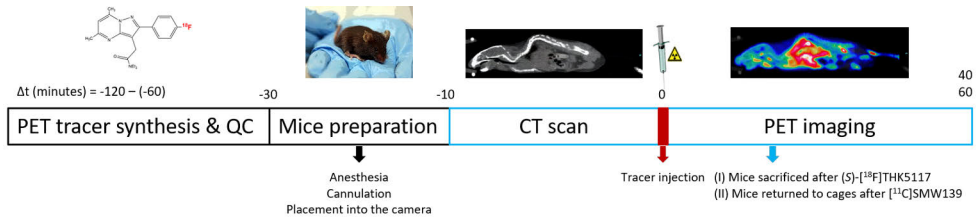

Figure 13. Illustration of imaging workflow in studies I-II. QC: Quality control, Δt: time difference.

3D list mode PET data were converted into 3D sinograms and decay-corrected to the injection time, then divided into 49-time frames (30 × 10 s, 15 × 60 s, 4 × 300 s) and reconstructed using a 2D-filtered back-projection algorithm into an image with a voxel size of 0.78 × 0.78 × 0.80 mm, or approximately 0.5 mm^3. PET images underwent volume of interest (VOI)-based analysis using Inveon Research Workplace Image Analysis software (Siemens Medical Solutions). For the investigated ROIs in studies **I** and **II**, VOIs were manually drawn for the frontal cortex (FC), striatum (STR), THA, hypothalamus, hippocampus (HIPPO), neocortex (NC) and cerebellum (CB). VOIs drawing was guided by an external 3D magnetic

resonance imaging (MRI) mouse brain template (MRM NAt Mouse Brain Database, McKnight Brain Institute) and the mouse CT image in the absence of the corresponding PET image to avoid potential bias (Figure 12B). Regional radioactivity concentration in VOIs as mega Becquerel/ millilitre (MBq/ml) were semi-quantified as standardized uptake value (SUV)-based ratios relative to CB as reference region (**I**) or SUVs (**II**). Tracer pharmacokinetics were investigated from SUV time-activity curves (TACs) (**I,II**). Findings of tracers' uptake are presented from NC, THA and HIPPO as representative cortical and subcortical regions. Findings of tracers uptake in the other ROIs are presented in the original publications and, for simplicity purposes, are not presented here unless relevant to the discussion.

4.5.1 MAO-B enzyme *in vivo* blocking experiment (I)

(*S*)-[^{18}F]THK5117 binding to MAO-B enzyme in APP/PS1-21 mouse brain was assessed (**I**). Mice (n = 3) were pre-treated with MAO-B enzyme selective and irreversible inhibitor (R)-(−)-deprenyl hydrochloride (Selegiline hydrochloride, Sigma-Aldrich) (10 mg/kg, intraperitoneal, 600 µL) at 24 and 1 hour before PET imaging as previously described (207). Control mice (n = 2) did not receive any injections. After the PET scans, mice were sacrificed to investigate (*S*)-[^{18}F]THK5117 regional binding in the brain using *ex vivo* autoradiography and for IHC staining.

Table 5. Imaging protocol and mice count in studies I and II. Values presented as mean (standard deviation).

Study	**I**	**II**	
Radiotracer(s)	(*S*)-[^{18}F]THK5117	[^{11}C]SMW139	[^{18}F]F-DPA
Experimental design	Cross-sectional	Longitudinal	Cross-sectional
PET scan (min)	40	60	60
Injected activity (MBq)	6.0 (0.8)	9.5 (0.5)	6.7 (0.5)
Quantification Δt (min *p.i.*)	20-40	3-15	25-50
Quantification readout	SUV, VOI/ CB	SUV	SUV
Reference region	CB	-	-
Age groups (months)	2-3,6-10*,12-16,19-26	5,8,11,14	14
n tg (female)	28** (6)	6 (4)	3 (2)
n wt (female)	20 (6)	7 (6)	4 (4)

*mice used in MAO-B enzyme *in vivo* blocking experiment were 10 months old

**including mice used in MAO-B enzyme *in vivo* blocking experiment.

Abbreviations: min: minutes, MBq: mega Becquerel, Δt: time difference, *p.i.*: post injection, *n*: number of mice, tg: transgenic, wt: wild type, SUV: standardized uptake value, VOI: volume of interest, CB: cerebellum.

4.6 *Ex vivo* methods

4.6.1 Brain autoradiography (I,II)

Tracers binding was also assessed from mouse brain tissue sections to further evaluate the specific and non-specific binding (**I**,**II**). *Ex vivo* brain autoradiography experiments were performed in age-matched tg and wt mice at almost identical ages as the *in vivo* PET-imaged mice. Investigated time points were 40 min after (*S*)-[^{18}F]THK5117 injection (**I**, PET-imaged mice), and 10 min after [^{11}C]SMW139 injection (**II**, PET-imaged mice at 14 months, *unpublished data*) (Table 6).

Table 6. Protocols of *ex vivo* brain autoradiography experiments and mice count in studies I and II. Values presented as mean (standard deviation).

Study	**I**	**II**
Radiotracer(s)	(*S*)-[^{18}F]THK5117	[^{11}C]SMW139
Sacrifice Δt (min *p.i.*)	40	10
Injected activity (MBq)	6.1 (1)	10 (0.7)
Quantification readout	ROI/ CB	SUV
Reference region	CB	-
Age groups (months)	2-3,6-712-16,19-26	5,8-10,12,14
n tg (female)	15 (5)	13* (6)
n wt (female)	16 (7)	17* (8)

*****including longitudinally imaged mice
Abbreviations: Δt: time difference, min: minutes, *p.i.*: post-injection, MBq: mega Becquerel, *n*: number of mice, tg: transgenic, wt: wild type, ROI: region of interest, CB: cerebellum, SUV: standardized uptake value.

At the predefined time points and while under deep anaesthesia, mice were sacrificed by cardiac puncture, during which they underwent transcardial perfusion with saline to eliminate the blood from the brain and peripheral organs. Cardiac blood (200-500 µL) was collected immediately into a gel-lithium heparin tube (Terumo Europe, Leuven, Belgium), and the rapidly dissected brain was weighed, measured for radioactivity in an automatic gamma counter (Wizard^2 2480, Perkin Elmer, Turku, Finland) and proceeded for *ex vivo* experiments. The brain was quickly frozen by immersion into isopentane (C_5H_{12}, Sigma Aldrich, Missouri, USA) cooled on dry ice. 20 µm-thick coronal brain sections were cut from various ROIs using the cryomicrotome (Leica CM 3050 S cryostat, Leica Microsystems, Germany). The cut sections were mounted on microscope slides, cool-air dried, and exposed to erased imaging plates (Fuji imaging plate BASTR2025, Fuji Photo Film Co., Japan) for at

least two half-lives of the radionuclide. Imaging plates were then scanned at 25 µm spatial resolution (BAS5000 analyser, Fujifilm Lifesciences, Japan) (Figure 14).

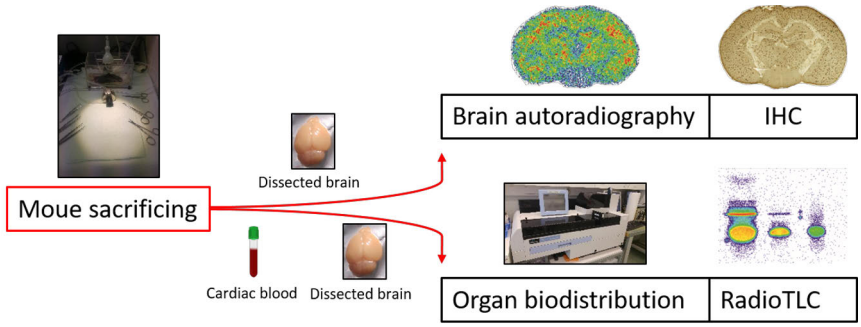

Figure 14. Illustration of *ex vivo* experiments workflow in studies I-III. IHC: immunohistochemistry, RadioTLC: radio-thin-layer chromatography.

The digital images of radioactivity distribution on the brain sections were analysed using Aida Image Analysis software (Raytest Isotopenmeßgeräte GmbH, Straubenhardt, Germany). ROIs were drawn manually on ≥ 7 sections (**I-II**)/ ROI/mouse for FC, STR, CTX, HIPPO, THA, hypothalamus, pons and CB (Figure 12C). Images were analysed for count densities and expressed as background radioactivity-corrected photo-stimulated luminescence intensity per pixel (PSL/ pixel-Bkg, pixel size 25 µm x 25 µm = 625 µm^2) in the ROI as ratios to a reference region (**I**) or SUV (**II**). In ratio calculations, CB was used as a reference region. For SUV calculations, the ROI PSL/ pixel-Bkg value was converted into SUV based on brain percentage injected radioactivity per gram (%IA/g) (using the PSL/pixel-Bkg of the ROI and CTX and the pre-measured CTX %IA/g values). Findings of tracers' uptake are presented only from CTX as a representative region. Findings of tracers uptake in the other ROIs are presented in the original publications and, for simplicity purposes, are not presented here unless relevant to the discussion.

4.6.2 Radio-thin-layer chromatography (I-III)

RadioTLC, i.e. thin-layer chromatography combined with digital autoradiography, was used (**I-III**) to assess tracers metabolism in mouse plasma and brain. Change in tracer parent fraction and number of formed radiometabolites were investigated at 5, 15, 30, 45 and 60 min after (*S*)-[^{18}F]THK5117 injection (**I**), and at 10, 30 and 45 min after [^{11}C]SMW139 injection (**II-III**) (Table 7). The tracer parent fraction in plasma is the total fraction of free and protein-bound tracer sub-fractions, whereas the tracer parent fraction in the brain consists of the free sub-fraction only.

Table 7. RadioTLC experimental design and mice count in studies I-III.

Study	I	II	III
Radiotracer	(*S*)-[^{18}F]THK5117	[^{11}C]SMW139	[^{11}C]SMW139
Sacrifice Δt (min *p.i.*)	5,15,30,45,60	10,30,45	10,30,45
Injected activity (MBq)	6.25 (0.65)	10.9 (2.74)* 19.5 (7.73) 19.8 (5.17)	14.5 (5.8)
Age groups (months)	2-3,6-7,12-13,15-16, 19-21,24-26	5,8-10**,12-15	5-13
n Plasma,tg (female)	3 (1)	19 (10)	-
n Plasma, wt (female)	20 (12)	40 (22)	46 (19)***
n Brain,tg (female)	3 (1)	12 (10)	-
n Brain, wt (female)	20 (12)	34 (21)	34 (11)

*Injected doses at 10,30 and 45 minutes, respectively.
**At 10 min, mice were 8-10 mo; at 30 and 45 min, mice were 7-10 mo.
***Counts in the table only represent the number of mice from which parent fraction analysis was successful. As reported in the original publication, a total of 43 female and 30 male mice were used for method development.
Abbreviations: Δt: time difference, min: minutes, *p.i.* post-injection, MBq: mega Becquerel, *n*: number of mice tg: transgenic, wt: wild type.

Mouse blood and brain were collected as described above in chapter 4.6.1. Plasma was obtained by centrifuging the cardiac blood and separating the supernatant. The separated plasma (100 µL) was then measured for radioactivity, mixed with acetonitrile, and centrifuged to precipitate plasma proteins. A brain homogenate from the dissected brain (up to one-third of the cortex) was manually homogenised with the TLC mobile phase as a solvent in a glass homogeniser and centrifuged to obtain a protein-free, clear homogenate. Afterwards, plasma and brain homogenate supernatants were applied on the TLC plate (Merck KGaA, Darmstadt, Germany) and placed in a TLC twin-chamber (10x10 cm) containing the mobile phase to develop for migration distance of 4 cm during a predefined migration time. A tracer sample (5 µL, roughly corresponding to plasma sample radioactivity) diluted into the mobile phase was also applied on the TLC plate as a reference standard to identify tracer parent fraction from radiometabolite fractions (Table 8).

In study **III**, measured ^{11}C-radioactivity in plasma and brain as %IA/g prior to radioTLC procedure was used to calculate [^{11}C]SMW139 total and metabolite-corrected *ex vivo* TACs at 10, 30, and 45 min post-injection (*p.i.*). Additionally, a subset of mice (n = 3, 4, 4 at 10, 30 and 45 min, respectively) were used in the PPB experiment to analyse the protein-free fractions of [^{11}C]SMW139 (f_P, free parent tracer over all radioactivity) and radiometabolites (f_M, free radiometabolites over all

radioactivity) in plasma. Blood-separated plasma underwent an ultrafiltration step in the 10-kDa UF semipermeable membrane (Microcon-10 kDa Centrifugal Filter Unit with Ultracel-10 membrane, Merck KGaA). Starting plasma (~80 µL) placed in the membrane was centrifuged (14,100*g*, 7 min) to obtain the first filtrate, which in the membrane was further centrifuged to obtain the second filtrate (14,100*g*, 4 min). The first and second filtrates (10 µL each) were then processed for radioTLC together with the other samples as described above (Figure 2, original publication **III**).

Table 8. Protocols of RadioTLC experiments in studies I-III.

Study	I	II	III
Radiotracer	(*S*)-[^{18}F]THK5117	[^{11}C]SMW139	[^{11}C]SMW139
Chromatography	TLC	HPTLC* (and TLC**)	TLC
Plasma centrifugation	2000*g* x 3 min	12100*g* x 90s	12100*g* x 90s
Plasma:acetonitrile	-	1:1.4 *v/v*	1:2 *v/v*
Brain homogenate centrifugation	2000*g* x 3 min	2000*g* x 3 min	2000*g* x 3 min
TLC plate	silica gel 60 F254 (Art no. 1.05567.0001)	high-performance silica gel 60 RP-18 (Art no. 1.05914.0001)	silica gel 60 RP-18 (Art no. 1.05559.0001)
Mobile phase	acetonitrile/0.5 M phosphoric acid (50/50, *vol/vol*)	acetonitrile:water:trifluoroacetic acid (75:25:0.1, *v/v/v*)	acetonitrile:water:trifluoroacetic acid (65:35:0:1, *v/v/v*)
Mobile phase (µL)***	5	15	15
Plasma sample (µL)	20	5-12	10
Brain homogenate sample (µL)	20	8-20	10
Migration time (min)	-	35-50	6
Migration distance (cm)	4	4	4

*HPTLC and TLC chromatographical methods were used in study II to separate radioactive compounds; findings were very similar. HPTLC method is described in the table under study II.
**The same TLC method was used in studies II and III
***Volume µL/ chamber
Abbreviations: TLC: thin-layer chromatography, HPTLC: high-performance TLC, min: minutes, cm: centimetre, s: seconds, v/v: volume/volume.

Thereafter, plates were dried with warm air, processed for digital autoradiography as described above in chapter 4.6.1, and scanned at 50 µm spatial resolution to visualize the separated radioactive compounds. Chromatographical analysis was performed using Aida Image Analysis software. In the chromatogram, the reference standard corresponded to the unchanged tracer, i.e. the parent fraction in the plasma and brain homogenate samples. The proportion of (*S*)-[^{18}F]THK5117 and

[^{11}C]SMW139 parent fractions were quantified as percentages from the total ^{18}F- or ^{11}C-radioactivity in the sample by dividing the background radioactivity-corrected PSL value of the parent fraction to the PSL value of the whole sample.

4.6.3 Organ biodistribution (I,II)

Distribution of ^{18}F-radioactivity after (*S*)-[^{18}F]THK5117 injection (**I**) and ^{11}C-radioactivity after [^{11}C]SMW139 injection (**II**) were studied in tg and wt mice to investigate tracers peripheral distribution, excretion and check for defluorination with (*S*)-[^{18}F]THK5117. In study **I**, the PET-imaged mice and additional mice were sacrificed 40 min after (*S*)-[^{18}F]THK5117 injection. In study **II**, [^{11}C]SMW139 was allowed to distributed for 10, 30 and 45 min (Table 9).

Table 9. Biodistribution experiments and mice count in studies I and II.

Study	I	II		
Radiotracer(s)	(*S*)-[^{18}F]THK5117	[^{11}C]SMW139		
Quantification readout	%IA/g	%IA/g		
Sacrifice Δt (min *p.i.)*	40	10	30	45
Injected activity (MBq)	6.14 (1.04)	10.07 (1.63)	21.3 (2.79)	24.2 (2.81)
n tg (female)	13 (4)	22 (12)	2 (2)	-
n wt (female)	15 (6)	23 (13)	15 (6)	10 (8)
Age groups (months)	2-3,6-7,12-13,15-16, 19-21,24-26	5,8-10,12,14		

Abbreviations: Δt: time difference, min: minutes, *p.i.*: post-injection, MBq: mega Becquerel, *n*: number of mice, tg: transgenic, wt: wild type, %IA/g: percentage injected radioactivity per gram.

Mice were sacrificed by cardiac puncture as described above in chapter 4.6.1, and organs of interest were dissected immediately after scarification, individually weighted and measured for ^{18}F- and ^{11}C-radioactivity using a gamma counter (Wizard^2 2480, PerkinElmer, Finland) (Figure 14). Organs of interest included whole blood, plasma, erythrocytes, adrenal glands, thymus, spleen, pancreas, heart, kidneys, white adipose tissue, bladder, bone (parietal bone), muscles, testis and ovaries, lungs, salivary glands, eyes, brown adipose tissue, Harderian glands, brain, a sample from the cortex (only in **II**), gallbladder, liver, stomach, small intestine, and large intestine. Additionally, the tail radioactivity was measured to ensure the success of the tracer injection and that the tracer passed into the systemic circulation. Organ radioactivity measurements were corrected for the organ weight, ^{11}C- or ^{18}F-radioactivity decay and background activity. ^{18}F- and ^{11}C-radioactivity measurements were expressed as %IA/g, calculated using the following equation:

%IA/g = measured radioactivity (Bq) × 100%/ injected radioactivity (Bq) × organ weight (g).

4.7 Statistical analyses (I-III)

In all studies, results were presented as mean with standard deviation of the mean in brackets when $n \geq 3$, mean or individual values when $n < 3$. The group difference in (*S*)-[^{18}F]THK5117 regional uptake as binding ratios between tg and age-matched wt mice in cross-sectional *in vivo and ex vivo* imaging experiments was evaluated with the Mann-Whitney t-test (**I**). The difference in [^{11}C]SMW139 or [^{18}F]F-DPA regional uptake as SUVs between tg and age-matched wt mice in *in vivo* PET imaging was tested using t-test with Welch's correction (**II**). Longitudinal analysis of [^{11}C]SMW139 uptake as SUV was performed using a linear mixed model with compound symmetry covariance structure (**II**). The model consisted of *time* as a within-subject factor, *genotype* as a between-subjects factor and the interaction of both factors, *time x genotype*, which examined if tg and wt groups had significantly different trends of uptake change with ageing. If the interaction term was deemed insignificant, it was dropped from the model. As a post-hoc analysis, differences in the least squares means were assessed for all significant factors to find individual differences between time points. (**II**). The difference in [^{11}C]SMW139 parent fraction between tg and wt, female and male mice was examined using t-test with Welch's correction. The difference in (*S*)-[^{18}F]THK5117 biodistribution between tg and wt, female and male mice was examined using t-test with Welch's correction. The differences in [^{11}C]SMW139 biodistribution between tg and wt, female and male mice were examined using t-test with Welch's correction, while [^{11}C]SMW139 biodistribution difference between young and old mice at 5,8-10,12 and 14 months was examined using Kruskal-Wallis test. In all studies, statistical tests were performed as two-sided. *P*-value ≥ 0.05 was considered the threshold for statistical significance. Statistical analyses were performed in GraphPad Prism (GraphPad Software, San Diego, CA), except analyses of *in vivo* PET imaging in (**II**) were performed in SAS software (SAS Institute Inc., Cary, NC, USA).

5 Results

5.1 Assessment of Aβ plaques, p-tau, P2X7 receptor, and TSPO by IHC

APP/PS1-21 mice showed a quick onset and fast deposition of Aβ plaques, as previously reported (134). 6E10-positive Aβ plaques were detectable at 3 months in CTX, and at 7 months, all brain regions except CB were covered with Aβ plaques. With age, the amount of Aβ plaques heavily increased to the last evaluated time point at 23 months. Quantification of Aβ plaques in CTX and THA clearly differentiated tg from age-matched wt mice at the investigated time points (**I**). Representative cortical images of Aβ plaques and quantification of 6E10-positive plaques in CTX of tg and age-matched wt mice are presented in (Figure 15A-B). APP/PS1-21 mice presented sparse p-tau detectable at 7 until 23 months, without a clear increasing trend with age. P-tau spatial distribution seemed similar to Aβ plaques, starting in CTX and extending to subcortical regions, such as HIPPO, THA and STR. No NFTs were detected in any of the tg mice. Quantifying p-tau in CTX and THA did not show a clear difference between tg and age-matched wt mice (**I**). P-tau representative cortical images and quantification of AT8-positive staining in CTX of tg and age-matched wt mice are presented in (Figure 15C-D). Anti-P2X7-positive aggregates in APP/PS1-21 mice reflected a subtle increase in receptor expression in CTX, HIPPO, THA and STR, initially detectable at 5 months and remained modest until the last investigated time point at 15 months. Quantification of P2X7 receptor in CTX and THA showed a minor difference between tg and age-matched wt mice (**II**) (Figure 15E-F). TSPO expression was upregulated in a similar trend to Aβ plaques in APP/PS1-21 mice. Anti-PBR-positive aggregates in cortical and subcortical regions were detectable at 5 months and considerably increased with age until reaching a plateau at around 10 months. Quantification of TSPO in CTX and THA showed a clear difference between tg and age-matched wt mice (**II**) (Figure 15G-H). Quantification of P2Y12 receptor expression in APP/PS1-21 mice followed a similar pattern to TSPO and differentiated tg from age-matched wt mice (supplementary figure 4, original publication **II**).

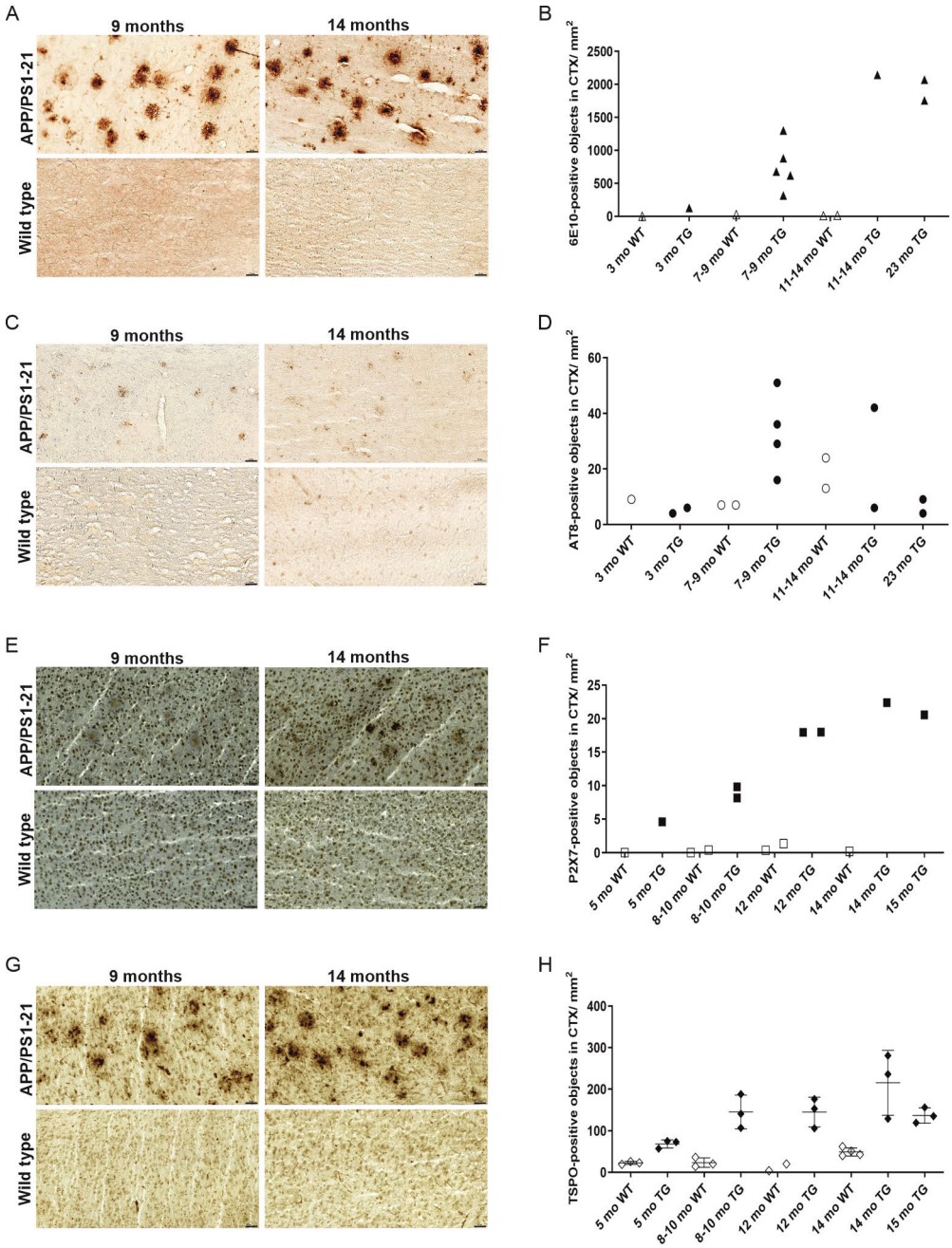

Figure 15. Immunohistochemical staining of imaging targets in APP/PS1-21 tg and wt mice. Representative images at 9 and 14 months, and quantification of β-amyloid peptides (Aβ) plaques (A-B), hyperphosphorylated tau (C-D), Purinergic 2 type X subtype 7 (P2X7) receptor (E-F) and Translocator protein 18-kDa (TSPO) (G-H) staining at all investigated time points. Microscopic captions magnification 20x, scale bar 50 μm. Image enhancement as colour brightness and contrast adjustments have been done to improve figure readability.

5.2 Pharmacokinetics profile of (*S*)-[^{18}F]THK5117 and [^{11}C]SMW139

5.2.1 Metabolism in plasma and brain

(*S*)-[^{18}F]THK5117 was moderately metabolised in mouse plasma and stable in the brain. Tracer parent fraction decreased from 71.1% (4.5) at 5 min to 19.7% (9) at 60 min *p.i.* from the total radioactivity in plasma, whereas (*S*)-[^{18}F]THK5117 parent fraction still comprised 91% (2.3) at 60 *p.i.* from the total radioactivity in the brain (Figure 16A,C). Multiple radiometabolites of (*S*)-[^{18}F]THK5117 were detected in mouse plasma at 60 min *p.i.* (Figure 16B), while only unchanged (*S*)-[^{18}F]THK5117 was detected in the brain (Figure 16D). No difference in tracer radiometabolism was found based on genotype, gender or age.

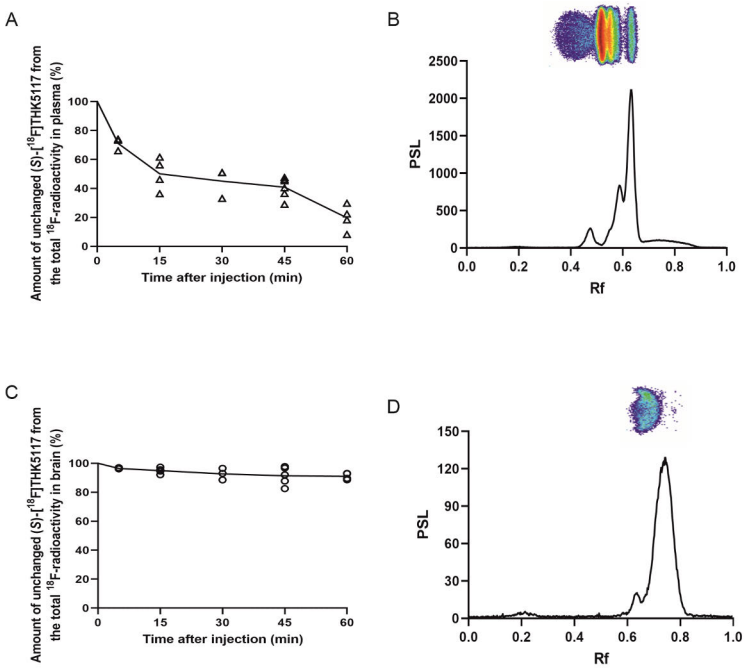

Figure 16. Metabolism of (*S*)-[^{18}F]THK5117 in APP/PS1-21 tg and wt mice. Change in (*S*)-[^{18}F]THK5117 parent fraction as percentage of total ^{18}F-radioactivity in plasma (A) and brain homogenate (C) at 5, 15. 30, 45 and 60 min post-injection *(p.i.)* (*n* = ≥ 3/ time point), (*S*)-[^{18}F]THK5117 radiochemical purity (~98%) was used as the maximum parent fraction value. Representative chromatogram and the corresponding autoradiograph of (*S*)-[^{18}F]THK5117 and its radiometabolites from mouse plasma and brain homogenate at 60 min *p.i.* (B,D). min: minutes, PSL: photostimulated luminescence, Rf: retardation factor.

[^{11}C]SMW139 was metabolised exceptionally fast in mouse plasma and brain. Parent fraction of [^{11}C]SMW139 decreased rapidly from 69.1% (9) at 10 min to 32.7% (5.8) at 45 min *p.i.* from the total radioactivity in plasm, and similarly in the brain from 74.1% (12.3) to 29.8% (9) (Figure 17A,C). Already at 10 min *p.i.,* 2 to 4 radiometabolites of [^{11}C]SMW139 were detected in plasma with increasing amounts until 45 min. Up to 3 radiometabolites were also detected in the brain (Figure 17B,D). In line with radiometabolite analysis, the difference between [^{11}C]SMW139 total and metabolite-corrected *ex vivo* TACs showed the actual level of unchanged [^{11}C]SMW139 in plasma and brain, and that the tracer and its radiometabolites enter the brain (Figure 4, original publication **III**). [^{11}C]SMW139 seemed to metabolise faster and to a greater extent in female than male mice in plasma and brain, although the difference was not statistically significant ($P > 0.41$) (Figure 7, original publication **II**). No difference in [^{11}C]SMW139 metabolism was noted based on genotype or age ($P > 0.43$).

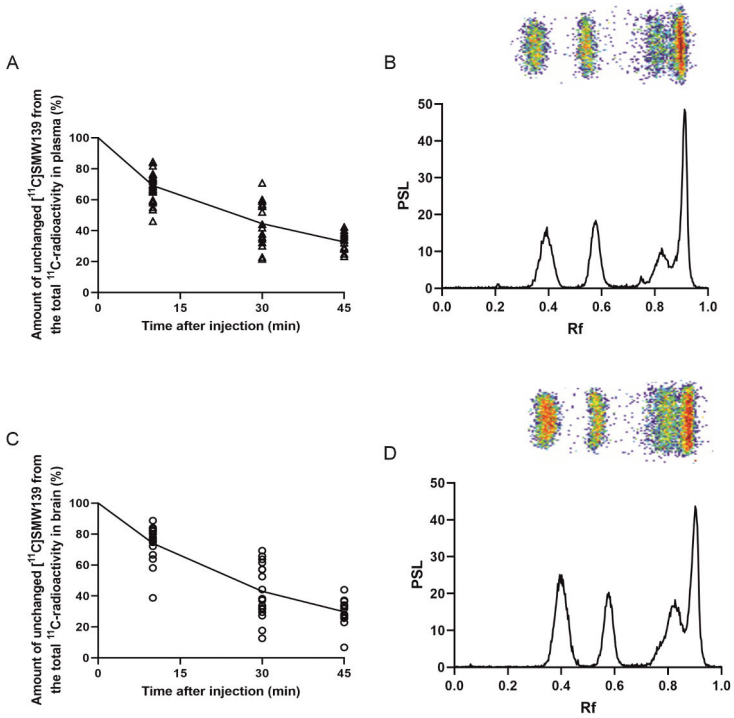

Figure 17. Metabolism of [^{11}C]SMW139 in APP/PS1-21 tg and wt mice. Change in [^{11}C]SMW139 parent fraction as percentage of total ^{11}C-radioactivity in plasma (A) and brain homogenate (C) at 10, 30 and 45 min post-injection *(p.i.)* (n = ≥ 13/ time point), [^{11}C]SMW139 radiochemical purity (~98%) was used as the maximum parent fraction value. Representative chromatogram and the corresponding autoradiograph of [^{11}C]SMW139 and its radiometabolites from mouse plasma and brain homogenate at 45 min *p.i.* (B,D). min: minutes, PSL: photostimulated luminescence, Rf: retardation factor.

In plasma, [^{11}C]SMW139 f_P was low and decreased rapidly from 0.032 at 10 min to 0.007 at 45 min *p.i.*, while f_M remained at much higher levels, between 0.37 and 0.35, during the same time points (Table 1 and figure 5, original publication **III**). Similarly, the fraction of free [^{11}C]SMW139/all free radioactivity in plasma decreased rapidly from 0.085 at 10 min to 0.019 at 45 min *p.i.*, while the fraction of free radiometabolites remained relatively constant (Table 1 and Figure 6, original publication **III**).

5.2.2 Organ biodistribution

Peripheral (*S*)-[^{18}F]THK5117-derived ^{18}F-radioactivity 40 min *p.i.* showed no abnormal uptake in mice. ^{18}F-radioactivity was taken up the most into the excreting organs, with relatively higher uptake into the liver (7(3.3)) and small intestine (48.9 (25.8)) than the kidneys (1.91 (1.64)). High ^{18}F-radioactivity was also noted in the eyes (10.3 (3.31)) and Harderian glands (2.61 (1.18)). Very low ^{18}F-radioactivity was taken up into the skull bone (0.19 (0.09)) (Figure 18A and C). ^{18}F-radioactivity peripheral distribution was similar in tg and wt, female and male, young and old mice ($P > 0.52$). Brain TACs showed that (*S*)-[^{18}F]THK5117 rapidly penetrated the brain and that tracer uptake peaked at 2 min *p.i.* then gradually cleared from the brain. The time frame 20-40 min was selected for (*S*)-[^{18}F]THK5117 binding ratio calculations (Figure 18B).

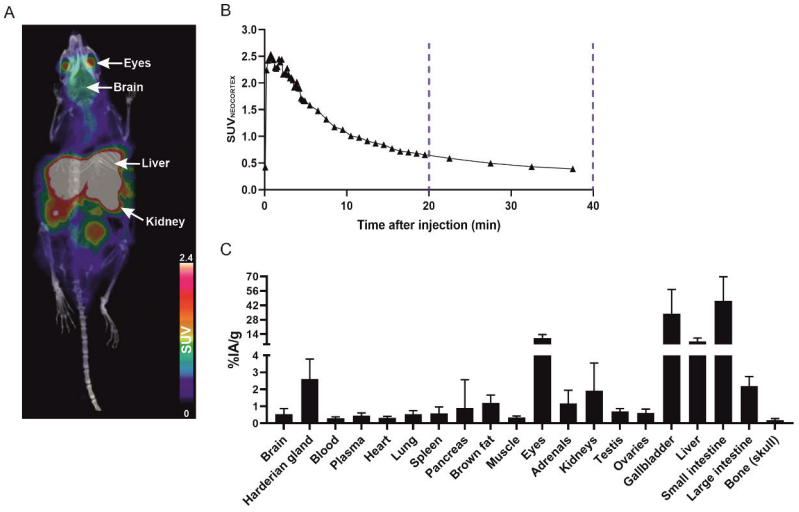

Figure 18. Whole body *in vivo* distribution of (*S*)-[^{18}F]THK5117 in mice. (A) Whole body PET/CT image of APP/PS1-21 tg mouse at 24 months summed during the whole dynamic PET scan 0-40 min. (B) Time-activity curve of (*S*)-[^{18}F]THK5117 in the neocortex of the same mouse. The time frame used for (*S*)-[^{18}F]THK5117 standardized uptake value (SUV) ratio calculations is highlighted with dotted lines. (C) Distribution of (*S*)-[^{18}F]THK5117 in the major organs of interest at 40 min post-injection as percentage injected radioactivity per gram (%IA/g). min: minutes.

At the investigated 10, 30 and 45 min time points, [^{11}C]SMW139-derived ^{11}C-radioactivity was taken up the most in Harderian glands (10 min, 10.5 (1.2)), brown fat (10 min, 5.1 (0.7)) and the excreting organs in liver (10 min, 12 (3.1)), small intestine (10 min, 5.31 (1.12)) and kidneys (10 min, 4.31 (0.84)). Increased ^{11}C-radioactivity uptake was also noted in the eyes at 45 min (Figure 19A and C, *unpublished data*). No clear difference in ^{11}C-radioactivity was noted based on genotype ($P > 0.49$), gender ($P > 0.31$) or age ($P > 0.63$). [^{11}C]SMW139 rapidly penetrated and cleared from the brain; its uptake peaked under 1 min *p.i.* The early time frame of 3-15 min was selected for [^{11}C]SMW139 SUV calculations, due to the [^{11}C]SMW139 fast metabolism and the presence of BBB-penetrating radiometabolites (see chapter 5.2.1) (Figure 19B, *unpublished data*).

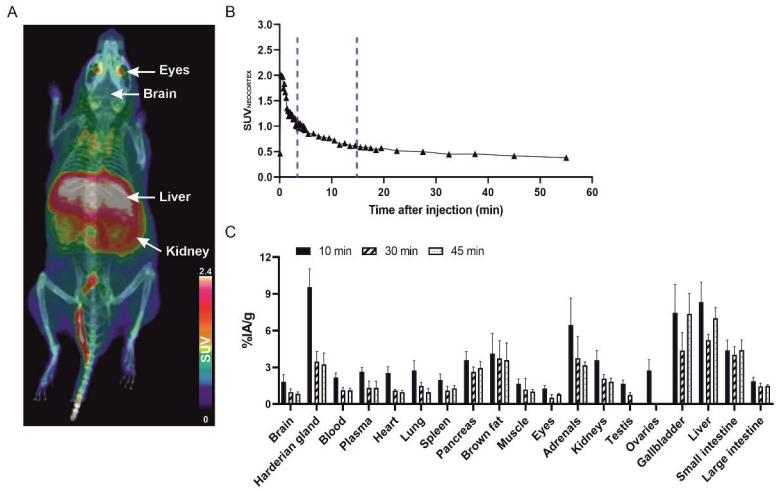

Figure 19. Whole body *in vivo* distribution of [^{11}C]SMW139 in mice. (A) Whole body PET/CT image of APP/PS1-21 tg mouse at 14 months summed during the whole dynamic PET scan 0-60 min. (B) Time-activity curve of [^{11}C]SMW139 in the neocortex of the same mouse. The time frame used for [^{11}C]SMW139 standardized uptake value (SUV) calculations is highlighted with dotted lines. (C) [^{11}C]SMW139 distribution in the major organs of interest at 10, 30, and 45 min post-injection as percentage injected radioactivity per gram (%IA/g). min: minutes.

5.3 (*S*)-[^{18}F]THK5117 uptake in the APP/PS1-21 mouse model

5.3.1 *In vivo* uptake of (*S*)-[^{18}F]THK5117

Increased (*S*)-[^{18}F]THK5117 uptake was observed in APP/PS1-21 tg mice compared to their age-matched wt mice and younger APP/PS1-21 tg mice. Binding ratios were significantly higher ($P \leq 0.01$) in tg mice compared to wt mice in NC and THA at

the investigated time points 6-10, 12-16 and 19-26 months. Binding ratios did not rise in wt mice at any investigated time point. (*S*)-[^{18}F]THK5117 uptake in tg mice reached a plateau at 12-16 months (Figure 20). (*S*)-[^{18}F]THK5117 uptake in CB was minimal, and no statistically significant difference was found between tg and wt mice at any investigated time point (Supplementary figure 2, original publication **I**). Similar findings were also seen in FC, STR and HIPPO (original publication **I**).

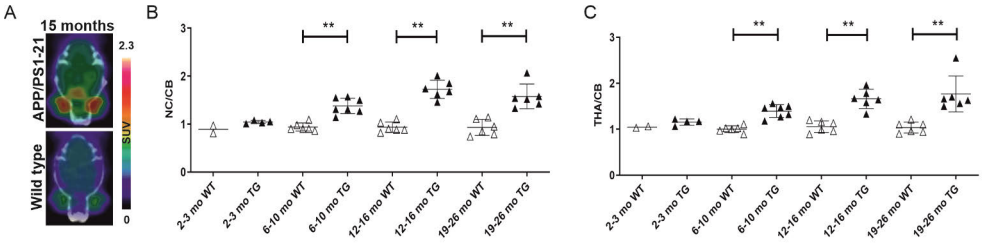

Figure 20. *In vivo* uptake of (*S*)-[^{18}F]THK5117 in APP/PS1-21 transgenic (tg) and wild type (wt) mice (2-26 months). (A) Representative PET images of (*S*)-[^{18}F]THK5117 uptake in APP/PS1-21 tg and wt mice at 15 months summed of 45 min post-injection. (*S*)-[^{18}F]THK5117 binding ratios to the cerebellum (CB) in the neocortex (NC) (B) and thalamus (THA) (C) at 2-3, 6-10, 12-16 and 19-26 months, *n* = 4,7,6,6 tg mice and 2,6,6,6 wt mice. ** = $P < 0.01$. SUV: standardized uptake value.

5.3.2 *Ex vivo* uptake of (*S*)-[^{18}F]THK5117

The *ex vivo* uptake of (*S*)-[^{18}F]THK5117 in APP/PS1-21 tg mouse brain was consistent with the *in vivo* uptake and showed a similar distribution pattern and increasing trend. Binding ratios were significantly higher ($P \leq 0.01$) in tg compared to age-matched wt mice in CTX at the time points 12-16 and 19-26 months (Figure 21). Similar findings were also seen in FC, STR, THA, HIPPO and pons (Figure 3, supplementary figure 3, original publication **I**).

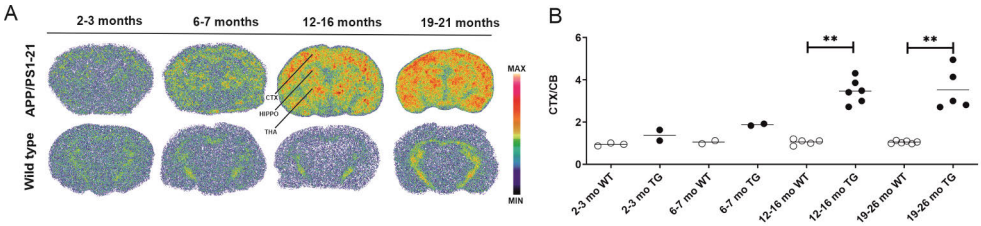

Figure 21. *Ex vivo* uptake of (*S*)-[^{18}F]THK5117 in APP/PS1-21 transgenic (tg) and wild type (wt) mice (2-26 months) 40 min post-injection. (A) Representative coronal autoradiography images of (*S*)-[^{18}F]THK5117 uptake in tg and wt mice at 2-3,6-7,12-16 and 19-26 months. All images are adjusted to the same colour intensity level of 2000-30000. (B) (*S*)-[^{18}F]THK5117 *ex vivo* binding ratios to cerebellum (CB) in cortex (CTX) at 2-3 (*n* = 3 wt, 2 tg), 6-7 (*n* = 2 wt, 2 tg), 12-16 (*n* = 5 wt, 6 tg) and 19-26 (*n* = 6 wt, 5 tg) months. ** = $P < 0.01$. HIPPO = hippocampus, THA = thalamus.

5.3.3 MAO-B enzyme *in vivo* blocking in APP/PS1-21 mice

In vivo blocking of MAO-B enzyme reduced (*S*)-[^{18}F]THK5117 uptake in APP/PS1-21 mouse brain, which confirmed (*S*)-[^{18}F]THK5117 binding to MAO-B enzyme *in vivo*. After tg mice were pretreated with (R)-(−)-deprenyl hydrochloride, (*S*)-[^{18}F]THK5117 binding ratios in NC, HIPPO and THA were reduced by 18.2%, 17.3% and 14.7%, respectively, compared to age-matched untreated tg mice of the same gender (Figure 22A). The effect of MAO-B enzyme blocking appeared clearly in PET and autoradiography images (Figure 22B). A similar reduction in (*S*)-[^{18}F]THK5117 binding was observed in other brain regions (supplementary table 5, original publication **I**). Upon visual inspection, MAO-B enzyme expression seemed similar in treated and untreated tg mice (Figure 22C).

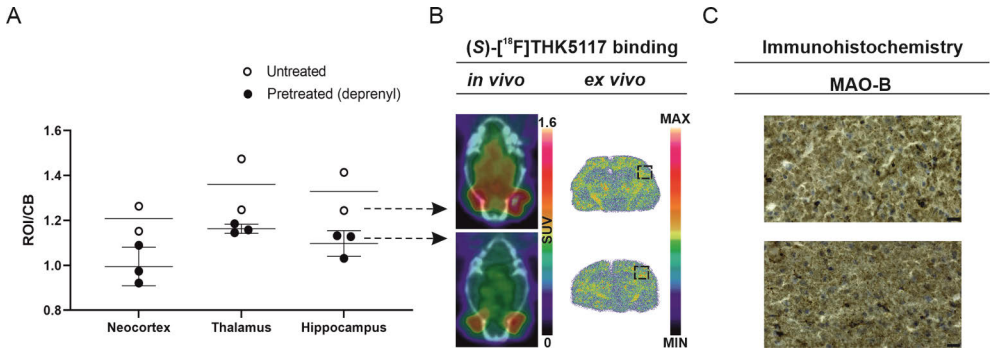

Figure 22. (*S*)-[^{18}F]THK5117 brain uptake and monoamine oxidase B (MAO-B) enzyme immunohistochemical staining in APP/PS1-21 transgenic (tg) mice following MAO-B enzyme *in vivo* blocking. (A) (*S*)-[^{18}F]THK5117 *in vivo* binding ratios to the cerebellum (CB) in the neocortex, thalamus and hippocampus of pretreated (n = 3) and untreated (n = 2) tg mice at 10 months. (B) PET and autoradiography images from the same pretreated and untreated mice (black arrows). PET images summed of 45 min post-injection, and autoradiography images are adjusted to the same colour intensity level of 2000-30000. (C) MAO-B enzyme immunohistochemical staining in pretreated and untreated mice. Microscopic captions magnification 63x, scale bar 20 µm. Image enhancement, such as colour brightness and contrast adjustments, have been done to improve figure readability. ROI: region of interest, SUV: standardized uptake value.

5.3.4 Association between (*S*)-[^{18}F]THK5117 brain uptake and Aβ plaques in APP/PS1-21 mice

The visual appearance of (*S*)-[^{18}F]THK5117 uptake in APP/PS1-21 tg mice brain seen in the *in vivo* PET and *ex vivo* autoradiography images associates with Aβ plaques load seen in IHC staining images from the same mice. Moreover, in several brain regions, Aβ plaques seen in IHC staining images could be spotted in the *ex vivo* brain autoradiography images of (*S*)-[^{18}F]THK5117 uptake as high signal plaque-like spots (Figure 23, Figure 4 original publication **I**).

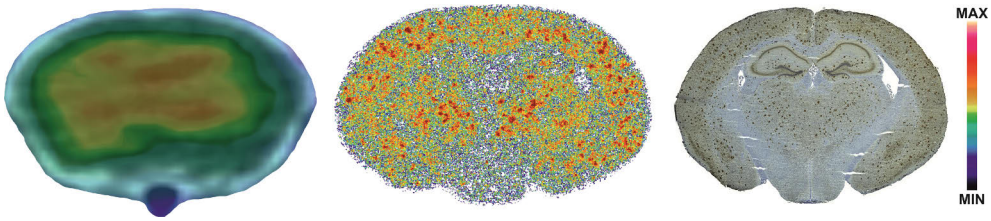

Figure 23. Association between (*S*)-[^{18}F]THK5117 brain uptake and Aβ plaques in APP/PS1-21 transgenic (tg) mice. *In vivo* PET and *ex vivo* autoradiography brain uptake of (*S*)-[^{18}F]THK5117 and Aβ plaques immunohistochemical (IHC) staining in the same tg mouse at 10 months.

5.4 [^{11}C]SMW139 uptake in the APP/PS1-21 mouse model

5.4.1 *In vivo* longitudinal uptake of [^{11}C]SMW139

No clear change in [^{11}C]SMW139 brain uptake was detected in APP/PS1-21 tg or wt mice with ageing from 5 to 14 months. In the same tg or wt mouse, longitudinal analysis of [^{11}C]SMW139 SUVs in NC did not change significantly ($P = 0.53$) when compared from baseline at 5 months to 8, 11 and 14 months. Similarly, no clear increasing or decreasing trend of [^{11}C]SMW139 mean SUVs was detected in the tg or wt groups from 5 to 14 months, due to the high within-group variation. Group difference in [^{11}C]SMW139 SUVs between tg and age-matched wt mice did not reach statistical significance ($P = 0.53$) at any time point (Figure 24). Similar findings were also seen in other brain regions (Figure 2, original publication **II**).

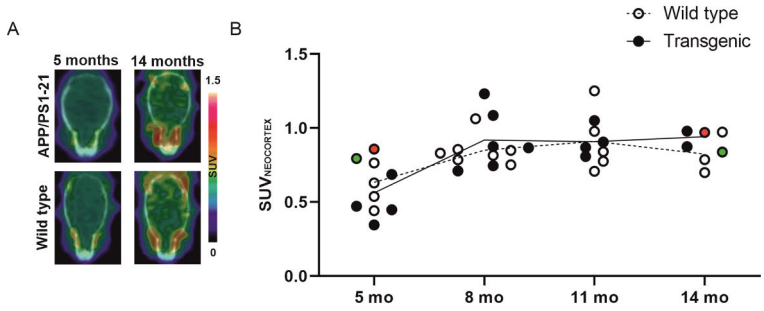

Figure 24. *In vivo* longitudinal uptake of [^{11}C]SMW139 in APP/PS1-21 transgenic (tg) and wild type (wt) mice (5-14 months). (A) Representative PET images of [^{11}C]SMW139 uptake in the same tg and age-matched wt mice at 5 and 14 months summed 60 post-injection. (B) Longitudinal [^{11}C]SMW139 binding standardized uptake value (SUV) in neocortex at 5,8,11 and 14 months. *n* = 5,6,4,3 tg mice and 5,7,5,4 wt mice. The black line represents averaged [^{11}C]SMW139 SUV in tg mice. The dotted line represents averaged [^{11}C]SMW139 SUV in wt mice. The red dot represents the same tg mouse at the first and last time points, and the green dot represents the wt mouse.

5.4.2 *Ex vivo* uptake of [^{11}C]SMW139

[^{11}C]SMW139 *ex vivo* uptake appeared evenly distributed in the brain of APP/PS1-21 tg and wt mice (Figure 25A). [^{11}C]SMW139 *ex vivo* uptake was consistent with the tracer *in vivo* uptake. Binding SUVs of [^{11}C]SMW139 in CTX did not show an increasing trend in tg mice and were similar to binding SUVs in age-matched wt mice at the time points 5,8,11, and 14 months (Figure 25B). Similar findings were also seen in THA (Figure 5, original publication **II**).

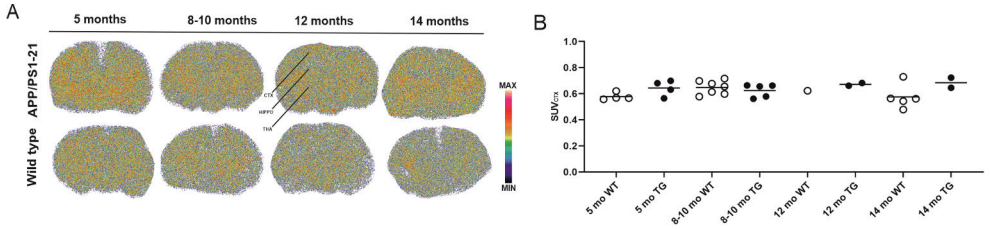

Figure 25. *Ex vivo* uptake of [^{11}C]SMW139 in APP/PS1-21 transgenic (tg) and wild type (wt) mice (5-14 months) 10 min post-injection. (A) Representative coronal autoradiography images of [^{11}C]SMW139 uptake in tg and wt mice at 5,8-10,12 and 14 months. All images are adjusted to the same colour intensity level of 1000-20000. (B) [^{11}C]SMW139 *ex vivo* uptake as standardized uptake value (SUV) in cortex (CTX) at 5 (n = 4 wt, 4 tg), 8-10 (n = 7 wt, 5 tg), 12 (n = 1 wt, 2 tg) and 14 months (n = 5 wt, 2 tg). HIPPO = hippocampus, THA = thalamus.

5.4.3 Comparison between [^{11}C]SMW139 and [^{18}F]F-DPA *in vivo* brain uptake in mice

Brain PET images of [^{18}F]F-DPA clearly differentiated APP/PS1-21 tg from age-matched wt mice, which was not achieved in the same mice with [^{11}C]SMW139 images (Figure 3, original publication **II**). At the 14 months time point, [^{18}F]F-DPA binding SUVs in NC were significantly higher (P = 0.03) in tg compared to age-matched wt mice, whereas [^{11}C]SMW139 binding SUVs also in NC did not significantly differ (P = 0.14) between the same groups (Figure 26A). *In vivo* imaging findings were validated with IHC staining of TSPO and P2X7 receptor. In the same imaged mice, TSPO expression was strongly upregulated in tg mice, unlike P2X7 receptor expression, which was weakly upregulated. TSPO and P2X7 receptor expression was not upregulated in WT mice (Figure 26B).

A

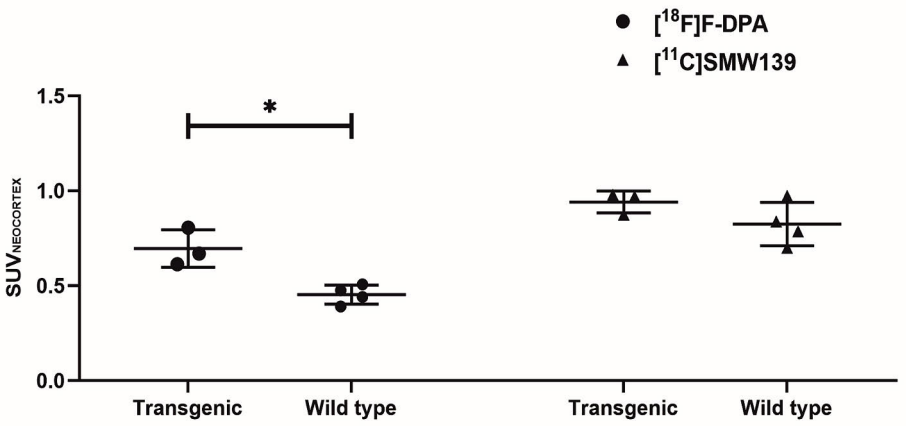

B

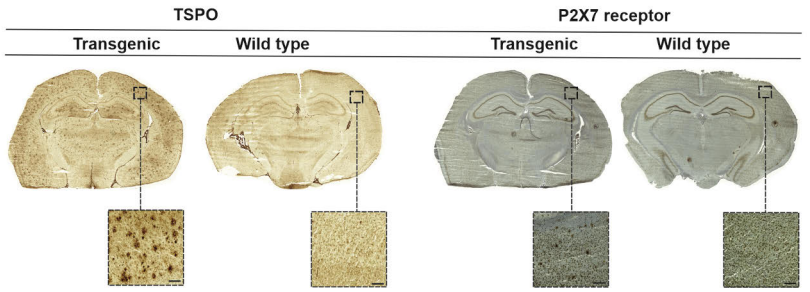

Figure 26. Comparison of [^{11}C]SMW139 and [^{18}F]F-DPA uptake in APP/PS1-21 transgenic (tg) and wild type (wt) mice at 14 months. (A) *In vivo* uptake as standardized uptake value (SUV) of [^{11}C]SMW139 and [^{18}F]F-DPA in the neocortex of tg (n = 3) and age-matched wt mice (n = 4). (B) Representative immunohistochemical staining of translocator protein 18-kDa (TSPO) and purinergic 2 type X subtype 7 (P2X7) receptor in the same tg and wt mice imaged with [^{11}C]SMW139 and [^{18}F]F-DPA. Microscopic captions magnification 1.5x and scale bar 1000 µm for hemisphere caption, 10x and scale bar 100 µm for cortex caption. Image enhancement, such as colour brightness and contrast adjustments, have been done to improve figure readability. * = P < 0.05.

6 Discussion

6.1 Utility of APP/PS1-21 mouse model in preclinical development of PET tracers

The APP/PS1-21 mouse model used in this thesis work has been well-characterised and widely utilised in several PET preclinical imaging studies (7) (14) (208) (209) (210) and the broader AD research (211) (212) (213). In our experience, tg mice have been viable in reasonably good health for up to 23 months. This makes the APP/PS1-21 mouse model an excellent choice, especially for longitudinal imaging studies or efficacy evaluation studies of novel therapeutics.

6.1.1 Assessment of the imaging targets in APP/PS1-21 mouse model

Aligned with amyloid pathology characterisation in the APP/PS1-21 mouse model (134), the used APP/PS1-21 tg mice in the first study of this thesis showed an early onset of Aβ deposition with fast and aggressive temporal progression of Aβ plaques as seen by IHC staining (**I**). It has been reported that in the APP/PS1-21 mouse model, NFTs are absent, and only p-tau are present around Aβ plaques, demonstrating that deposition of Aβ plaques does not lead to aggregation of NFTs in this mouse model (134) (214). Similarly, we did not detect any NFTs in tg mice by IHC staining, only sparse endogenous p-tau that mildly spread in the brain (**I**). The aggressive neuroinflammatory response in the APP/PS1-21 mouse model exerted by reactive microglia and astrocytes (134) was present in the used tg mice. IHC staining demonstrated that TSPO upregulated expression onset and temporal progression followed closely that of Aβ plaques throughout the tg mouse brain, unlike the less convincing P2X7 receptor IHC staining (**II**). These findings indicate that the APP/PS1-21 mouse model phenotypes abundant Aβ plaques load and TSPO upregulated expression in reactive glia, making APP/PS1-21 a suitable model for PET preclinical imaging of Aβ plaques and TSPO. On the contrary, this model has limited utility for preclinical evaluation of PET tracers targeting tau pathology, restricted to assessing *in vivo* binding selectivity, due to the absence of the imaging target, i.e. deposits of p-tau and NFTs in this model. Similarly, the APP/PS1-21

mouse model is unsuitable for the preclinical evaluation of PET tracers targeting P2X7 receptor, due to insufficient upregulated expression in reactive glia.

6.1.2 AD rodent models – strengths and weaknesses

Rodent models of AD have received criticism for their lack of resemblance with human AD. At the same time, they have been praised for their capability to mimic specific pathological changes of AD (130) (131) (132). As highlighted in chapter 2.1.4, no rodent model mimics the late-onset AD, and robustly features the full pathology spectrum of human AD. While the models TgF344-AD (135) and 3xTg-AD (138) have come close to that by mimicking Aβ plaques and NFTs deposition, neuroinflammation and cognitive decline, however, still not with the same complexity and dynamics seen in humans. Overcoming this limitation by the availability of a "complete" AD rodent model would undoubtedly be a remarkable breakthrough in terms of translatability to human AD. However, from a biological imaging perspective, one could argue that this limitation, although relevant, should not be over-stressed at the expense that some well-characterised rodent models also phenotype reliable and, in many cases, translatable amyloid or tau pathology, which have proven to be of great value in PET preclinical imaging studies (9) (12).

The majority of amyloid pathology rodent models do not feature NFT deposition. The same is true for tau pathology models, which do not feature Aβ plaques (130) (131) (132), suggesting that Aβ plaques or tau NFTs alone are not sufficient to drive all pathological processes in rodents, and raising questions on the translatability of amyloid and tau hypotheses. However, one exception is the rat model TgF344-AD featuring both Aβ plaques and NFTs (135). In addition, only a few rodent models of amyloid or tau pathology phenotype neurodegeneration, which is often unconvincing, hard to replicate, and at best localised to specific brain regions (131). Accordingly, a fundamental distinction is that amyloid pathology rodent models which phenotype only p-tau but not NFTs should not be considered models of tau pathology, and their validity for investigating tau pathology should be carefully considered. Similarly, using rodent models without clear and well-established neurodegeneration should probably be avoided to maintain the validity of behavioural studies assessing cognitive impairment in rodents.

In the future, AD rodent models will continue to be an essential tool in preclinical PET imaging and evaluating novel PET tracers. That said, accurate comparisons of imaging target similarities and differences between humans and rodents are crucial for findings' validity and translatability, potentially saving resources and leading to more efficient output of tracer preclinical development. Moreover, using rodent models that phenotype multiple potential targets of a tracer would become more necessary for tracer *in vivo* binding assessment. For instance, the concomitant

presence of Aβ plaques and NFTs offers a more realistic environment to assess tracer binding behaviour *in vivo*, especially binding selectivity, which is a major limitation with developed tracers. It must be stressed that the availability of well-characterised rodent models will improve the quality and translational power of preclinical findings in developing PET tracers and even novel medications in the future.

6.2 (*S*)-[^{18}F]THK5117 suitability for imaging tau pathology

The preclinical evaluation of (*S*)-[^{18}F]THK5117 in this thesis was inspired by serendipity. At the time (*S*)-[^{18}F]THK5117 radiosynthesis was being established at Turku PET Centre, we noticed in pilot testing high (*S*)-[^{18}F]THK5117 brain uptake in APP/PS1-21 mouse model, despite the absence of tau pathology in this model (134) (214). Limited reports were available on (*S*)-[^{18}F]THK5117 *in vivo* binding selectivity at the time; thus, study **I** was initiated to investigate this phenomenon. While APP/PS1-21 is not a mouse model of tau pathology, this model was ideal to evaluate (*S*)-[^{18}F]THK5117 non-specific binding and particularly binding selectivity against Aβ plaques, due to the absence of (*S*)-[^{18}F]THK5117 binding target, i.e. p-tau deposits. Below, findings of (*S*)-[^{18}F]THK5117 preclinical evaluation (**I**) will be discussed in relation to the same *S*-stereoisomer form of the tracer. If relevant findings are not available in the literature, our findings will be discussed in relation to the racemic form of the tracer, i.e. [^{18}F]THK5117 or other THK tracers.

6.2.1 Pharmacokinetics profile of (*S*)-[^{18}F]THK5117

(*S*)-[^{18}F]THK5117 metabolic rate measured in mouse plasma (**I**) is similar to that reported in humans, although the tracer metabolises faster in mice (215). In mouse plasma, (*S*)-[^{18}F]THK5117 metabolised into several more polar radiometabolites, none of which were detected in the brain (**I**). Similarly, at least 2 radiometabolites of the THK tracers [^{18}F]THK-5351 and [^{18}F]THK-5451 were identified in mouse plasma, which did not seem to penetrate the brain (216). (*S*)-[^{18}F]THK5117 metabolic rate was similar in female and male mice (**I**). On the contrary to our findings, it has been reported that the tracer metabolises faster in male than female rats (217). These findings support the notion that tracer metabolism could be gender and/or species-dependent, which needs to be considered when evaluating novel PET tracers and performing tracer kinetic modelling.

The peripheral distribution of (*S*)-[^{18}F]THK5117 in mice was predominantly excreted via the hepatobiliary route (**I**). Similarly, the highest peripheral distribution of [^{18}F]THK5117 in mice has been reported in the liver (202), suggesting a similar excretion route as with (*S*)-[^{18}F]THK5117. ^{18}F-radioactivity measured from the skull

bone was very low at 40 min *p.i.*, indicating a stable ^{18}F labelling position and that (*S*)-[^{18}F]THK5117 does not undergo defluorination *in vivo* (**I**). Similarly, low *ex vivo* bone uptake has also been reported with [^{18}F]THK5117 in mice (202). (*S*)-[^{18}F]THK5117 displayed a desirable pharmacokinetics profile for *in vivo* imaging, entering the brain rapidly and clearing reasonably fast (**I**). Similar brain uptake and clearance have also been reported with [^{18}F]THK5117 in preclinical *ex vivo* biodistribution assessment (202) (216).

6.2.2 (*S*)-[^{18}F]THK5117 binding selectivity to tau pathology

In vivo PET and *ex vivo* autoradiography imaging with (*S*)-[^{18}F]THK5117 revealed higher brain uptake in APP/PS1-21 tg compared to age-matched wt mice, and higher tracer uptake in older compared to younger tg mice (**I**). Increased (*S*)-[^{18}F]THK5117 uptake in tg mice was associated with increased Aβ plaques IHC staining, whereas a similar association could not be established in the absence of NFTs and the limited endogenous p-tau in tg mice (**I**). Moreover, (*S*)-[^{18}F]THK5117 marked uptake in autoradiography was found in close association with Aβ plaques IHC staining (**I**). These findings combined suggest that (*S*)-[^{18}F]THK5117 bind to Aβ plaques in the APP/PS1-21 mouse model. Although this was a cross-sectional imaging study, we investigated APP/PS1-21 and wt mice by *in vivo* PET, *ex vivo* autoradiography, and IHC staining from 2-26 months, which enabled thorough evaluation of (*S*)-[^{18}F]THK5117 brain uptake. We noted that (*S*)-[^{18}F]THK5117 brain uptake reached a plateau in tg mice starting at 12 months, despite the continuous increase in Aβ plaques load in the older tg mice.

A preclinical imaging study demonstrated similar findings to ours, raising similar concerns on (*S*)-[^{18}F]THK5117 *in vivo* binding selectivity against Aβ plaques. In a tg rat model of amyloid and tau pathologies, *in vivo* (*S*)-[^{18}F]THK5117 and [^{11}C]PiB uptake were assessed in relation to p-tau and Aβ plaques load, respectively. Both tracers showed increased uptake in tg rats' brains with a similar regional uptake pattern in the same rats. While [^{11}C]PiB uptake correlated with the increased expression of Aβ plaques, (*S*)-[^{18}F]THK5117 uptake did not correlate with the low expression of p-tau (218). Another study in the APP/PS1-21 mouse model with [^{18}F]AV-45 targeting Aβ plaques revealed several similarities to our findings using (*S*)-[^{18}F]THK5117 in the same mouse model. First, [^{18}F]AV-45 brain uptake in *in vivo* PET and *ex vivo* autoradiography was higher in tg than age-matched wt mice, and Aβ plaque staining associated with the imaging findings. Second, [^{18}F]AV-45 brain uptake values were in a similar range to those we obtained with (*S*)-[^{18}F]THK5117. Third and interestingly, autoradiography images of [^{18}F]AV-45 looked very similar to (*S*)-[^{18}F]THK5117 in the APP/PS1-21 mouse model (210).

On the other hand, preclinical imaging with [^{18}F]THK5117 in P301S and BiGT tau pathology mouse models revealed that the temporal distribution and spatial progression of tau pathology in these models could be followed with [^{18}F]THK5117 *in vivo* PET and *ex vivo* autoradiography imaging, and that tracer uptake differentiated tg from wt mice (219). Another longitudinal imaging study in the P301S mouse model showed that [^{18}F]THK5117 is less sensitive to tau pathology than flortaucipir, the clinically approved tau tracer (12). Both studies highlighted limitations with [^{18}F]THK5117 *in vivo* imaging, the high white matter binding, and radioactivity signal spill-in from extracerebral structures, namely the cranium indicating *in vivo* defluorination, and the Harderian glands (12) (219). In our findings, we also noted high (*S*)-[^{18}F]THK5117 uptake in the Harderian glands, whereas minimal white matter binding was noted in *ex vivo* autoradiography, mainly in older wt mice. The extent of this non-specific binding did not interfere with tracer uptake quantification in the brain. (*S*)-[^{18}F]THK5117 did not undergo defluorination in mice, as assessed from *in vivo* and *ex vivo* skull bone uptake. Our findings align with the reports that using the *S* stereoisomer of THK tracers results in reduced white matter binding and no defluorination (216) (220).

In clinical evaluation, (*S*)-[^{18}F]THK5117 showed high uptake in HIPPO and relevant cortical regions in the *post-mortem* AD brain, and the tracer binding pattern was similar to that of tau IHC (221). Several *in vivo* imaging studies in individuals with AD reported that (*S*)-[^{18}F]THK5117 can image the expected extent and regional distribution of tau pathology (215) (222) (223) (224) (225) (226) (227) (228). Interestingly, one study in patients with idiopathic normal pressure hydrocephalus showed that (*S*)-[^{18}F]THK5117 brain uptake did not significantly correlate with neuropathologically verified tau pathology in brain biopsy from the same patients (229). Meanwhile study I of this thesis was ongoing; reports showed similar [^{3}H]THK5117 and [^{3}H]deprenyl regional binding patterns (230), and that [^{18}F]THK5117 binds substantially to MAO-B enzyme in *post-mortem* AD brain (231). Subsequently, the suspected binding of THK tracers to MAO-B enzyme was assessed *in vivo*. (*S*)-[^{18}F]THK5117 and MAO-B enzyme tracer, [^{11}C]DED, showed overlapping brain uptake patterns in individuals with AD (232). THK tracers binding to MAO-B enzyme was further proven in a study that showed up to ~52% reduced *in vivo* uptake of [^{18}F]THK5351 in different brain regions after selegiline pretreatment in individuals with AD (233). In agreement with these clinical findings, we established (*S*)-[^{18}F]THK5117 binding to MAO-B enzyme in mouse brain. Our findings showed that (*S*)-[^{18}F]THK5117 brain uptake is reduced by up to ~25% in APP/PS1-21 tg mice following *in vivo* pharmacological blocking of MAO-B enzyme with selegiline (Supplemental Table 5, original publication I).

In the brain, MAO-B enzyme is predominantly expressed by astrocytes. *Post-mortem* analysis revealed that MAO-B enzyme exhibits increased activity and

upregulated expression due to inflammation in AD (234), which could be imaged with the MAO-B enzyme PET tracer, [^{11}C]DED, which showed increased brain uptake in individuals with AD (235) (232). Selegiline (also known as deprenyl) is an irreversible and selective inhibitor of MAO-B enzyme (no inhibition on MAO-A) (234), which demonstrated in PET studies that it binds MAO-B enzyme (236). Similarly, in reactive astrocytes of the APP/PS1 mouse model, MAO-B enzyme exhibits increased activity and upregulated expression (234), and *in vivo* [^{11}C]DED uptake was higher in APP_{ArcSwe} than wt mice in HIPPO, THA, STR and CTX (11).

6.2.3 Development of tau PET tracers - learned lessons and future prospects

(*S*)-[^{18}F]THK5117 and other first-generation tau tracers have shown binding to NFTs and close correspondence between tracer uptake and Braak staging of tau pathology in AD. However, the same tracers also showed significant binding to Aβ plaques, MAO-A and B enzymes, white matter, and vascular structures, complicating and casting doubts on *in vivo* signal quantification (232) (237). Thus, the future utility of the first-generation tau tracers, including (*S*)-[^{18}F]THK5117, for imaging tau pathology is likely limited by their lack of selective binding. Studies addressing non-specific binding and its impact on signal quantification are highly important, especially for the ongoing development of second-generation tau tracers, which have demonstrated improved binding characteristics compared to first-generation tracers.

Making a closer assessment of (*S*)-[^{18}F]THK5117 development, the tracer indeed showed a relatively different *in vivo* distribution pattern in the AD brain compared to amyloid pathology tracers. However, distribution patterns of (*S*)-[^{18}F]THK5117 and [^{11}C]PiB still showed overlapping uptake to the same cortical regions in *in vivo* PET (226) and *in vitro* autoradiography (230), which does not rule out (*S*)-[^{18}F]THK5117 binding to Aβ plaques in individuals with AD. The early stages of (*S*)-[^{18}F]THK5117 development relied heavily on binding findings obtained from *post-mortem* AD brains. The tracer was then rushed to clinical development, where it was judged based on its ability to differentiate individuals with AD from healthy subjects, or the severity of AD. Findings of such studies are often informative regarding non-specific binding, but not so much regarding binding selectivity. In a retrospective view, it seems that the missing aspect from (*S*)-[^{18}F]THK5117 development was a more careful assessment of binding selectivity in brains negative for tau pathology. Perhaps this is rather challenging clinically; however, in preclinical studies, this is feasible, and that is what we wanted to address in study **I** of this thesis, which was the first study to investigate (*S*)-[^{18}F]THK5117 binding to other potential targets, namely Aβ plaques and MAO-B enzyme in the absence of NFTs. That said, findings of preclinical evaluation must be critically assessed, as it

is unclear if tau aggregates in the rodent and human brain possess the same core structure and morphological features (238). The development of (*S*)-[^{18}F]THK5117, including our findings, demonstrates the superiority of *in vivo* over *in vitro* findings, and the importance of thoroughly evaluating tracers in relevant animal models, where the imaging target and the pathology in question resemble that in humans.

The main challenge facing the development of tau PET tracers remains to achieve *in vivo* binding selectivity over other similar targets, mainly Aβ plaques, and achieving minimal off-target binding to MAO-B enzyme, white matter and other structures in the brain. Two factors complicate binding selectivity against Aβ plaques in AD. First, PHFs in NFTs adopt a β-sheet structure similar to that seen in Aβ plaques (239). (*S*)-[^{18}F]THK5117 and other first-generation tau tracers binding to p-tau deposits is dependent on the β-sheet structure of PHFs (166), which indicates that tracers could also bind Aβ plaques. Second, NFTs and Aβ plaques co-localise in some brain regions, with 5-20 times higher Aβ plaques load than NFTs (240). Therefore, β-sheet-dependent binding is a common limitation of small molecule tau tracers, although second-generation tau tracers have shown promising binding selectivity in individuals with AD, warranting more extensive characterisation. The introduction of antibody constructs as PET tracers, i.e. immunoPET, and their demonstrated proof-of-concept for imaging Aβ plaques in rodents (9) (241) (242) (243) is a promising strategy to overcome the limitations seen with current tau PET tracers. Compared to small molecules, antibodies can bind their targets with superior affinity, selectivity, and the capacity to target different structural conformations of an aggregated protein. Moreover, antibodies could be engineered to bind a specific protein isoform or its post-translational modification, opening new possibilities for selective binding mechanisms and applications in other tauopathies than AD. However, suboptimal pharmacokinetics is a notable limitation associated with radiolabelled antibodies. Slow target accumulation and clearance of antibodies require the use of long-lived radionuclides for PET imaging and result in high radiation exposure (156). Collectively, tremendous progress has been made in developing tau PET tracers, and our understanding of tau aggregates as an imaging target has significantly improved. In the future, the availability of tau PET tracers with sufficient sensitivity and specificity for tau aggregates will facilitate the role of tau imaging in AD early diagnosis.

6.3 [^{11}C]SMW139 suitability for imaging P2X7 receptor in reactive glia

In this thesis, preclinical evaluation of [^{11}C]SMW139 in the APP/PS1-21 mouse model (**II**) was motivated by reports demonstrating upregulated expression of P2X7 receptor in different AD rodent models (244) (245) (246), together with reports that

robust neuroinflammation and reactive glia in this mouse model could be imaged with PET (7) (14) (247). Accordingly, we wanted to establish if we can image the already proven neuroinflammation and reactive glia in this model targeting the presumed upregulated expression of P2X7 receptor by [^{11}C]SMW139.

6.3.1 Pharmacokinetics profile of [^{11}C]SMW139

Similar to our findings in study **II**, [^{11}C]SMW139 showed to penetrate the brain and to be excreted predominantly via the hepatobiliary route in rats (197). [^{11}C]SMW139 rate of metabolism analysed in mouse plasma and brain was exceptionally fast (**II**,**III**), and much faster compared to that reported in humans (200), and rats' plasma and brain (196) (197). The metabolic profile of [^{11}C]SMW139 is further complicated by the early entry and efficient accumulation of radiometabolites in the brain. (**III**). Similar findings were reported in mice and humans (200). In rats, a high radiometabolite fraction was also reported in the brain (197). The ability of radiometabolites to cross the BBB is an undesired property of any tracer, as that hampers the quantification of tracer uptake in the brain. It is critical to consider BBB-penetrating radiometabolites when modelling tracer *in vivo* brain uptake. With [^{11}C]SMW139, it has been shown that correct modelling of tracer brain uptake demands correction for radiometabolites (200), and the quantification outcome would be inaccurate by not doing so (199).

In our findings, the molecular structure of [^{11}C]SMW139 radiometabolites has not been identified. Therefore, properties like size, molecular weight and lipophilicity of radiometabolites are unknown. With RadioTLC, it is only possible to evaluate lipophilicity based on TLC retardation factor (Rf) value to understand the BBB penetration ability of radiometabolites. The higher the Rf value of an analyte, the more polar, thus less lipophilic it would be. For radiometabolites, this means that they would be less able to penetrate the BBB compared to the parent tracer, due to being less lipophilic. However, the less lipophilic radiometabolites of [^{11}C]SMW139 were still able to penetrate and accumulate in the brain efficiently. This can be explained by assuming that the lipophilicity of radiometabolites was still sufficient for BBB penetration, and the very high f_M fraction compared to the f_P fraction of [^{11}C]SMW139 in plasma.

In mouse plasma, the low and rapidly decreasing [^{11}C]SMW139 protein-free fraction compared to radiometabolites protein-free fraction indicate that most of the free fraction available to enter the brain consisted of radiometabolites during the investigated time points 10-45 min (**III**). Quantifying protein-free fractions in plasma reveals the actual input of tracer and radiometabolites to the brain, as only the free fraction, i.e. unbound to plasma protein, can diffuse from the blood vessels to the brain tissue (159) (163) (164) (248). On the other hand, protein-bound

fractions are still important; they act as a reservoir to stabilise the concentration of free fractions and maintain the state of dynamic equilibrium. Part of the unchanged tracer will be realised from plasma protein when part of the free unchanged tracer is defused to the brain tissue from the blood (249).

6.3.2 Longitudinal imaging of P2X7 receptor with [^{11}C]SMW139

The change in [^{11}C]SMW139 *in vivo* brain uptake did not significantly increase in the same tg mouse longitudinally, nor as a group mean uptake in younger compared to older tg mice, or in tg compared to age-matched wt mice. These findings aligned with the absent widespread upregulated expression of P2X7 receptor in tg mice (**II**). Altogether, our findings indicate that using [^{11}C]SMW139 targeting P2X7 receptor to image reactive glia in the APP/PS1-21 mouse model is not feasible. This could be explained by [^{11}C]SMW139 reported 6-fold lower binding affinity to mouse compared to human P2X7 receptor (250), combined with the limited expression of P2X7 receptor in the APP/PS1-21 mouse model, which increases the likelihood of wrong negative findings. Moreover, the 19% mismatch in amino acid sequence between the human and mouse P2X7 receptor, and the identified 150 single nucleotide polymorphisms of P2X7 receptor may represent critical species differences that affect [^{11}C]SMW139 binding to P2X7 receptor (251).

No findings on preclinical imaging with [^{11}C]SMW139 in AD rodent models are available at the time of writing this thesis. Two preclinical imaging studies investigated [^{11}C]SMW139 brain uptake in rat models of MS. In the first study, [^{11}C]SMW139 showed higher uptake in the striatum, where human P2X7 receptor is overexpressed compared to the contralateral striatum. *In vivo* binding selectivity of [^{11}C]SMW139 to human P2X7 receptor was demonstrated by reduced tracer uptake in the striatum after pretreatment with a P2X7 receptor antagonist. However, in the same study, [^{11}C]SMW139 uptake was similar in AD and healthy *post-mortem* brains, despite upregulated expression of P2X7 receptor in the AD brain, casting doubts on the clinical utility of [^{11}C]SMW139, especially in AD (197). In the second study, [^{11}C]SMW139 showed higher uptake in the brain and spinal cord of MS rat model only at the peak phase of neuroinflammation, despite the weak rat P2X7 upregulated expression shown by IHC. *In vivo* tracer selective uptake was tested after pretreatment with a P2X7 receptor antagonist (196). The comparability of our study to these studies is limited for two reasons. First, it is known that [^{11}C]SMW139 binds to rodent P2X7 receptor with significantly less affinity than to human P2X7 receptor (196) (250). In our study, the APP/PS1-21 mouse model expresses endogenous mouse P2X7 receptor, while the MS rat model expresses human P2X7 receptor in the first study (197), and in the second study, the MS model expresses rat P2X7

receptor (196). Second, we investigated [^{11}C]SMW139 brain uptake in an AD tg mouse model, while these studies investigated [^{11}C]SMW139 brain uptake in MS rat models, where neuroinflammation was induced by intracerebral injection of viral vector (197) or peripheral injections of inflammation triggers (196).

Motivated by the *post-mortem* findings that P2X7 receptor is strongly upregulated in MS brain (198), and that [^{11}C]SMW139 does not bind P2X7 receptor in AD (197), one clinical study evaluated [^{11}C]SMW139 in a small set of individuals with MS and healthy subjects (199). In this study, [^{11}C]SMW139 showed slightly higher brain uptake in the MS group, with a critical assumption that [^{11}C]SMW139 brain-penetrating radiometabolites detected in rats (197) do not penetrate the human brain. Subsequently, in another study, it was revealed that [^{11}C]SMW139 metabolism produces three similar radiometabolites in healthy human subjects and mice plasma; two of these radiometabolites were also detected in mice brains, concluding that correction for BBB-penetrating radiometabolites is critical for correct [^{11}C]SMW139 *in vivo* quantification (200). Clinical evaluation of [^{11}C]SMW139 is yet to reveal the true potential of this tracer to image P2X7 receptor in neurodegenerative diseases.

6.3.3 Comparison of [^{11}C]SMW139 and [^{18}F]F-DPA uptake in the APP/PS1-21 mouse model

Previously, [^{18}F]F-DPA targeting TSPO showed the ability to image reactive glia and neuroinflammation in the APP/PS1-21 mouse model (7) (247) (252). Therefore, in study **II**, after the last longitudinal imaging time point with [^{11}C]SMW139, mice were scanned with [^{18}F]F-DPA to compare both tracers' ability to image reactive glia in the same mice. As expected, brain uptake of [^{18}F]F-DPA was significantly higher in tg compared to age-matched wt mice, and tracer uptake was in line with the strongly upregulated expression of TSPO in tg mice (**II**). On the contrary, [^{11}C]SMW139 brain uptake did not differ significantly between tg and age-matched wt mice, which was in line with the minor upregulated expression of P2X7 receptor in tg mice. These findings indicate that imaging reactive glia and neuroinflammation in the APP/PS1-21 mouse model is better achieved by targeting TSPO with [^{18}F]F-DPA than P2X7 receptor with [^{11}C]SMW139, as TSPO but not P2X7 receptor expression reflects the level of ongoing neuroinflammation in the APP/PS1-21 mouse model. To our knowledge, preclinical imaging studies comparing PET tracers targeting TSPO and P2X7 receptor in AD rodent models are not available. However, in a PD rat model, [^{18}F]DPA-714 targeting TSPO and [^{11}C]JNJ-717 targeting P2X7 receptor showed increased uptake in *in vitro* autoradiography with an overlapping time course, indicating upregulated expression of both imaging targets, which was in line with IHC staining of both targets (253).

6.3.4 Imaging reactive glia - learned lessons and future prospects

TSPO remains the most widely used imaging target for *in vivo* assessment of neuroinflammation. TSPO is considered a reliable imaging target because its expression is low in physiological conditions and strongly upregulated in neuroinflammation (254) (255) (256) (257) (258). However, PET imaging of TSPO is associated with several limitations. Collectively, TSPO PET tracers suffer from high non-specific binding and limited capacity to quantify TSPO expression *in vivo*, which partly limits their routine clinical use (255) (256) (257). On the other hand, TSPO as an imaging target is widely expressed in the periphery. In the CNS, its expression is not limited to reactive microglia; also reactive astrocytes and other cell types express TSPO to varying degrees. Besides, TSPO expression is upregulated in both reparative and damaging events. Thus, quantifying the uptake of TSPO PET tracers needs to be regarded as a sum of neuroinflammatory processes, where some are detrimental and others are restorative. Finally and possibly the most pressing limitation of TSPO is an identified polymorphism that commonly occurs in the TSPO gene and results in more than 10-fold difference in tracers binding affinity to TSPO, causing high inter-subject variability of TSPO tracers uptake. The only TSPO PET tracer that does not exhibit sensitivity to this polymorphism is [^{11}C]PK11195, which partly explains why this tracer remains the gold standard for imaging TSPO, despite its complex uptake quantification methods (254) (255) (256) (257) (258). Significantly, it has recently been shown that TSPO expression increases in reactive microglia in the mouse brain but does not necessarily change in the human brain during neuroinflammatory diseases. Moreover, TSPO expression in mice is related to different phenomena than in humans, and that TSPO-PET signals in humans reflect the density of inflammatory cells rather than the activation state as in mice (259). These findings raise concerns on the translatability of preclinical TSPO-PET imaging studies and must be considered in the future.

Over the years, several PET tracers targeting TSPO have been developed to overcome the limitations mentioned above (256) (260). Additionally, alternative imaging targets of reactive glia and neuroinflammation have been explored (254) (261) (262) (263). Nonetheless, despite its limitations, TSPO remains the gold standard imaging target of neuroinflammation. A superior imaging target to TSPO needs to show a lack of sensitivity to genetic polymorphisms. In addition, different expression profiles in different glial cells, and ideally upregulated expression specific to pro-inflammatory (M1) or anti-inflammatory (M2) functional phenotypes of reactive microglia. A superior PET tracer to the currently available tracers needs to show *in vivo* brain uptake that reflects the properties above. That said, one study using *post-mortem* MS brains and a rat model of MS revealed a predominant upregulated expression of P2X7 receptor in pro-inflammatory reactive microglia,

and upregulated expression of P2Y12 receptor mainly in anti-inflammatory reactive microglia (198). This same study demonstrated that enhanced expression of microglial P2X7 receptor is accompanied by decreased expression of P2Y12 receptor on the same cells (198). These findings suggest that P2X7 receptor could be a specific imaging target of pro-inflammatory (M1) reactive microglia, and P2Y12 receptor could be a specific imaging target of anti-inflammatory (M2) reactive microglia (198). Nonetheless, additional assessment of both receptors is needed, and the evaluation of PET tracers targeting P2X7 and P2Y12 receptors *in vivo* and in different neurodegenerative diseases is yet to reveal the true potential of these imaging targets over TSPO. Collectively, the ongoing development of PET tracers for imaging neuroinflammatory markers is important. In the future, adequately established imaging of neuroinflammation in AD could improve our understanding of the disease course and help connect the dots between amyloid, tau and other neuropathological processes in the brain.

6.4 Considerations with preclinical PET imaging

6.4.1 Methodological considerations

Preclinical and clinical PET imaging could be different in certain aspects. There are potential sources of error with preclinical PET imaging that are especially applicable to imaging targets in the mouse brain. **(i)** Dedicated small animal PET scanners, including the scanner used in this thesis studies, have a spatial resolution of ~1.5 mm. Although PET scanners with improved resolution have been developed (264), the physical properties of PET radionuclides, mainly the positron range, limit utilising further improvements in resolution. Accordingly, due to the relatively large pixel size, quantifying PET tracer uptake in mouse brain VOIs approaching the spatial resolution of the PET scanner leads to a phenomenon called partial volume effect (PVE). PVE result in underestimation of the quantified radioactivity signal, and this effect could be noted with lower *in vivo* tracer uptake compared to subsequently quantified tracer uptake in the same region using *ex vivo* autoradiography. In studies **I-II** of this thesis, mouse brain regions prone to PVE, such as HIPPO, were not used to firmly assess tracer brain uptake in APP/PS1-21 tg mice. **(ii)** Overestimation of the PET signal, partly related to the limited resolution of PET scanners, could potentially occur in some VOIs in the mouse brain, due to radioactivity spillover from adjacent structures with high radioactivity signal. In the mouse brain, cortical regions are prone to radioactivity signal spillover from the skull and Harderian glands, while white matter could cause spillover for subcortical regions. In studies **I-II**, no substantial tracer uptake was noted in white matter or skull. On the contrary, the Harderian glands' uptake was substantially high for both

(*S*)-[^{18}F]THK5117 and [^{11}C]SMW139. In an attempt to further avoid this issue, the CT image and MRI template rather than the PET image-guided VOIs drawing in the analysis. **(iii)** In preclinical imaging studies with mice, performing blood sampling during the PET scan is not feasible, due to the small total blood volume and challenging cannulation of the femoral or jugular artery in mice. Accordingly, quantifying tracers' brain uptake in mice is often performed as SUV binding ratios to a reference region, if available (**I**) or SUVs if no reference region exists (**II**). **(iv)** Am is one of the most important radiochemical parameters of a PET tracer and describes the radionuclide purity of tracer molecules as an amount of radioactivity in mass. Am refers to the number of tracer molecules labelled with the radionuclide and capable of producing radioactive signal relative to the total number of tracer molecules, including the no-longer radioactive ones, because their labelled radionuclides have already decayed. Achieving radiochemical synthesis with high Am is critical to limit the non-radioactive tracer molecules binding to and occupying the imaging target (152). This is particularly important when imaging targets with low presence in the brain (156). In studies **I-II**, all tracer batches were produced with Am values suitable for the imaged targets.

6.4.2 Translational considerations

PET tracers could show a lack of suitability in preclinical evaluation, due to suboptimal pharmacokinetics profile and/ or binding properties. Additionally, differences between rodents and humans could complicate imaging findings translatability. Generally, such differences could be identified early in tracer development, typically at the target validation stage or preclinical evaluation. **(i)** Physiological differences between rodents and humans. Efflux transporters within the BBB endothelial cell layer, such as P-glycoprotein (Pgp), is a relevant example that needs to be considered for PET tracers developed to image targets in the brain, as Pgp efflux transporters' expression level and activity are lower in humans than rodent (265). Some PET tracers could possess substrate activity to Pgp, thus be pumped back to the periphery and prevented from entering the brain, despite having suitable molecular weight and lipophilicity (266). **(ii)** Varying binding affinity of a PET tracer to the rodent and human versions of an imaging target. This obstacle was encountered in study **II** of this thesis. Compared to the human P2X7 receptor, [^{11}C]SMW139 binds mouse and rat P2X7 receptor with 6-fold and 5-fold lower affinity, respectively (196) (250). Similarly, another tracer targeting P2X7 receptor, [^{11}C]GSK1482160, showed significantly lower binding affinity to rat P2X7 receptor than human P2X7 receptor (183) (184). **(iii)** Variability within rodent models, and between rodent models and humans. There is an evident heterogeneity in pathologies developed in AD rodent models. Factors like background strain, selected mutation,

and used promoter cause variability in protein expression level and accordingly impact tracer *in vivo* binding and PET imaging. Thus, rodent model selection is a critical step in PET tracer evaluation (267) (268). For example, mouse models of amyloid pathology develop Aβ plaques that are different relative to each other and to human Aβ plaques, which has been supported by the varying uptake of PET tracers, such as [^{11}C]PiB in mice (13). Accordingly, In study **I** of this thesis, we cannot rule out that the different (*S*)-[^{18}F]THK5117 binding selectivity against Aβ plaques in the APP/PS1-21 mouse model compared to that reported in humans could be due to the differences in Aβ plaques structure in individuals with AD and APP/PS1-21 mice. **(iv)** Sufficient expression level of the imaging target in the rodent model. Availability of the imaging target is crucial for sufficient signal-to-noise ratio in the PET images, given that the tracer has suitable binding properties. In study **II** of this thesis, a superior signal-to-noise ratio was obtained from imaging the highly expressed TSPO compared to the low expressed P2X7 receptor in the APP/PS1-21 mouse model. **(v)** Species selection. Neurobiology and brain networks of mice and rats are generally comparable to those of humans. Mice are more often used than rats in preclinical brain imaging studies, because creating tg AD models in mice is more feasible, as modifying the mouse genome is relatively more straightforward. In addition, mimicking pathologies in mice is more successful and occurs faster. Mice are also more cost-effective than rats as they are less expensive and demand less housing space (131) (269). Despite that, rats still have advantages over mice in brain imaging applications. The bigger brain size of rats is more practical when investigating small brain regions, especially considering the poor spatial resolution of PET imaging devices. In addition, the larger blood volume in rats allows blood sampling, which is useful in image data analysis. Rats also have richer and more interpretable behavioural displays than mice, which makes behavioural studies assessing cognitive decline more feasible in rats. Finally, rats are more favoured over mice in toxicity studies because of their larger organs and being physiologically closer to humans (131) (269).

6.5 Study limitations

There were limitations in all studies of this thesis, despite the careful planning and execution. In a retrospective view, all studies of this thesis would have benefited from periodic assessments of experimental work protocols and findings. This is particularly true for PET studies, due to the complicated logistics operating simultaneously or in quick succession. The following are specific limitations in each study. **(i)** Study **I** would have benefited from an *in vivo* blocking experiment of Aβ plaques in APP/PS1-21 tg mice to precisely assess (*S*)-[^{18}F]THK5117 binding to Aβ plaques. Also, imaging tau deposits in a robust rodent model of tau pathology with

(*S*)-[^{18}F]THK5117 would have provided insights on tracer *in vivo* binding affinity to tau pathology. **(ii)** Study **II** would have benefited from an *in vivo* PET imaging experiment with a P2Y12 receptor targeting PET tracer to shed more light on the neuroinflammatory environment in APP/PS1-21 tg mice, especially that reactive glia in the same mice were imaged by targeting P2X7 receptor and TSPO. However, tracer availability for P2Y12 receptor would have been an obstacle. **(iii)** In studies **I-II**, correlation analysis of findings from IHC staining quantification with *in vivo* PET and *ex vivo* autoradiography imaging would have further validated the conclusions made in those studies. **(iv)** The suboptimal pharmacokinetic properties of [^{11}C]SMW139 limited the options of *in vivo* tracer uptake quantification and forced the use of an early time frame for tracer SUV calculations, which is not typical with brain-targeting PET tracers. **(v)** Using a relatively small number of animals. In studies **I-II**, including more animals in the IHC staining experiment would have allowed for conducting statistical analysis of the performed quantification and drawing more concrete conclusions. Similarly, in study **III**, performing analysis of tracer and radiometabolites free fractions in more animals would have resulted in more robust comparisons. **(vi)** All experiments in studies **I-III** were performed in female and male mice for practical purposes and to increase the relatively small sample size. Although differences based on gender were rare and reported accordingly, it would have been more optimal to include only male or female mice in the studies.

7 Conclusions

I. The APP/PS1-21 mouse model of Aβ deposition is suitable for preclinical evaluation of PET tracers targeting Aβ plaques and TSPO. However, this mouse model is unsuitable for evaluating PET tracers targeting P2X7 receptor, and has limited utility for preclinical evaluation of PET tracers targeting tau pathology, restricted to assessing *in vivo* binding selectivity.

II. (*S*)-[^{18}F]THK5117 demonstrated a lack of *in vivo* binding selectivity in the APP/PS1-21 mouse model in the absence of tau pathology, as tracer uptake in the brain associated with Aβ plaques and demonstrated specific binding to MAO-B enzyme.

III. (*S*)-[^{18}F]THK5117 demonstrated desirable pharmacokinetic properties in mice, including no *in vivo* defluorination, moderate metabolic rate, and a lack of BBB-penetrating radiometabolites.

IV. Imaging reactive glia in the APP/PS1-21 mouse model using [^{11}C]SMW139 targeting P2X7 receptor is not feasible, as the longitudinal change in [^{11}C]SMW139 uptake did not increase in tg mice, possibly due to the weak upregulated expression of P2X7 receptor, and the significantly lower binding affinity of the tracer to the mouse than human P2X7 receptor.

V. Imaging reactive glia in the APP/PS1-21 mouse model is better achieved by targeting TSPO with [^{18}F]F-DPA than P2X7 receptor with [^{11}C]SMW139, as TSPO but not P2X7 receptor expression in the APP/PS1-21 mouse model reflects the level of ongoing neuroinflammation.

VI. [^{11}C]SMW139 demonstrated undesirable pharmacokinetic properties in mice, including an exceptionally fast rate of metabolism accompanied by a quick and efficient accumulation of several radiometabolites in the brain, and that the majority of protein-free fraction in plasma available for brain uptake consisting of radiometabolites.

Acknowledgements

My utmost gratitude is directed to Allah for blessing me with the strength and guidance to accomplish this work. The scientific research presented in this doctoral thesis was conducted at Turku PET Centre and Medicity Research Laboratory, Faculty of Medicine, University of Turku, Finland, from 2016 to 2023. I want to express my gratitude to the University of Turku for providing me with the opportunity to pursue my master's and doctoral degree studies.

I am deeply grateful to the supervisors of my thesis, Adjunct Professor Merja Haaparanta-Solin and Professor Juha Rinne. It has been a privilege to start my scientific research journey under your guidance. Merja, you taught me a lot about PET imaging and preclinical research. Thank you for encouraging me continuously, and for your warm presence over the years. Your leadership has truly been inspiring to me. Juha, I learned from you a lot about Alzheimer's disease, clinical and scientific research. Thank you for giving me the opportunity to be part of the Alzheimer's disease research team in Turku. Most importantly, thank you for supporting me during the critical times I went through in this long journey. You believed in me and never gave up on my thesis. That is something I will never forget.

To the follow-up committee members of my doctoral dissertation, Professor Sari Mäkelä, Adjunct Professor Tove Grönroos, and Adjunct Professor Sarita Forsback, I am grateful for your valuable advice and support during my doctoral training. I appreciate that you made yourselves available to help whenever I needed support. I would like to thank the examiners of my thesis, Associate Professor Kristina Herfert and Adjunct Professor Eino Solje, for their valuable comments, constructive criticism and advice. Your input improved the quality of my thesis significantly. I also thank Associate Professor Mikael Palner for accepting the invitation to be my opponent in the doctoral dissertation defense.

To all my co-authors, thank you for your valuable contribution to my thesis studies. Together we conducted scientific research that is important and valuable. A special thank you goes to my dear colleagues and co-authors Richard Aarino and Markus Matilainen. Richard, thank you for being the "go-to" expert with all radiometabolite-related and all practical matters. Your kind and helpful personality is unmatched. I am grateful for all the moments we shared during this journey.

Markus, thank you for sharing your priceless expertise in biostatistics. You always explained statistics to me like a piece of classical music.

My current and previous colleagues from the Preclinical Imaging Laboratory, Anniina Snellman, Jatta Helin, Susanne Vainio and Kirsi Mikkola, you all have been like older cousins to me. I am lucky I had you around during my PhD journey, thank you for the support and the memories. Anniina, I cannot thank you enough for your constant willingness to help and share your expertise, you have been a role model to me. You may not have been an official supervisor for this thesis, but your contribution was no less of that. Diana Bocancea, thank you for the friendship and the stimulating conversations over lunch. My office mates Vilhelmiina Parikka, Heidi Nykänen, Luciana Kovacs dos Santos and Saeka Shimochi, thank you for being such a great company. I also thank Heidi Liljenbäck, Johanna Rokka, Tomas Keller, Riikka Viitanen, Petri Elo, Mia Ståhle, Justyna Zdrojewska, and all students and post-docs over the years; it has been a pleasure having you as colleagues. To the heroes behind the scenes, our brilliant technicians! Aake Honkaniemi, Marko Vehmanen, Mira Eisala and Päivi Kotitalo. You all have been irreplaceable in my projects. Aake, the long and tense PET scans were much easier and enjoyable in your presence. Marko, thank you for the chats we had about football in Finnish.

I would like to thank everyone at the Turku PET Centre, who has been involved in my thesis. A special appreciation to Professor Olof Solin, your enthusiasm for research and science is a treasure to those around you. I sincerely thank Francisco Lopez Picon for supervising my master's thesis project and continuously sharing his neuroscience expertise. To the members of the Radiopharmaceutical Chemistry Laboratory and the Accelerator Laboratory, thank you for all the tracer batches you produced for my research. I thank Rami Mikkola for helping me with all IT-related matters, and Lenita Saloranta for assisting with all administration matters over the years. I would like to express my gratitude to the Drug Research Doctoral Programme for the offered educational opportunities, professional and financial support. A very special thank you to Eeva Valve for supporting me with administrative matters over the years. Also, I would like to thank Outi Irjala for the flawless guidance during the lengthy thesis submission process.

I sincerely thank Markus Peurla, Joanna Pylvänäinen, Laura Mairinoja and Junel Solis for sharing their valuable expertise and support with immunohistochemical staining image data processing and analyses. I also thank the staff of the Central Animal Facility at the University of Turku for taking care of my mice. Special thanks go to Małgorzata Major (Goshia) for teaching me how to handle and perform procedures in rodents.

To the three pillars of the Drug Discovery and Development master programme, Markku Koulu, Sanna Soini, and Eeva Rainio. Markku, thank you for caring about me, drawing my attention to Turku PET Centre and introducing me to my supervisor

Juha Rinne. Sanna, thank you for your effort in teaching and arranging our courses and study materials. Eeva, thank you for sending me the email that changed my life. You always managed to draw a smile on my face.

To my two companions since 2015, the two without whom this PhD journey would not have been the same, Ali Benkherouf and Jamal Kadiri. Ali, you are one of a kind. A loyal and caring friend. With you, I am willing to do whatever. Everyone can only dream of having a friend like you in their life. Over the years, we shared the ups and downs of life and the tears of joy and sorrow. I am so grateful for our friendship. Jamal, thank you for being the wise one. You have been someone who I always knew I could rely on and trust, no matter what. Ali, Jamal…we have made it! To the special one, Ashour Abdelrahman. You are the most brilliant listener I know. For many years, you listened so patiently to all my complaints and rambles. Thank you for always lending a shoulder to lean on. Also, your technical skills and help in preparing the figures of my thesis are much appreciated and saved me precious time, thank you! I also would like to thank Khalil Shahramian, Tarek Omran and Sherif Bayoumy for their special friendship and the happy memories. Minun suomen kielen opettajilleni, Niina Kuusivaara, Anni Toikka ja Anni Itähaarla, olen todella kiitollinen teidän tuestanne ja avustanne. Olin “vähän” haastava opiskelija ja aina kysyin kaikenlaista loogista ja epäloogista kysymyksiä, mutta jaksoitte aina vastata kysymyksiini kärsivällisesti. On ollut kunnia tietää teidät, ja olen erittäin iloinen, että me pidettiin yhteyttä jatkuvasti opiskelun vuosien jälkeen.

Lastly, my dad Mohammad Alzghool and my mom Magbouleh Almomani. Thank you for raising me to live my life with purpose. This PhD journey got out of me absolutely everything, and me reaching the finish line is a testament to you as parents. To my eldest brother Muath, thank you for putting me first and making the hard decisions, you have the purest heart. To all my other lovely siblings, Baraa, Khaled, Eman, Alaa and Esraa, I am forever grateful for your unconditional love. Finally, I want to thank me for the persistence, for all the hard work, for not giving up when I was not sure, for giving my absolute best in every attempt.

I am grateful to all the private foundations that have supported both my salary and participation in conferences abroad for the support: Suomen Kulttuurirahasto, Turun Yliopistosäätiö, Orionin Tutkimussäätiö, Paulon Säätiö, the Finnish Society of Nuclear Medicine, and the Scandinavian Society of Clinical Physiology and NuclearMedicine.

In Kaarina, 4.2.2024

Obada Alzghool

References

1. Dementia. WHO. https://www.who.int/news-room/fact-sheets/detail/dementia
2. Querfurth HW, LaFerla FM. Alzheimer's Disease. *NEJM*. 2010. 362(4):329–44.
3. Wyss-Coray T, Mucke L. Inflammation in neurodegenerative disease - A double-edged sword. *Neuron*. 2002. 35,419–32.
4. Kemppainen NM, Scheinin NM, Koivunen J, Johansson J, Toivonen JT, Någren K, et al. Five-year follow-up of ^{11}C-PIB uptake in Alzheimer's disease and MCI. *Eur J Nucl Med Mol Imaging*. 2014. 41(2):283–9.
5. Fleisher AS, Pontecorvo MJ, Devous MD, Lu M, Arora AK, Truocchio SP, et al. Positron Emission Tomography Imaging with [^{18}F]flortaucipir and Postmortem Assessment of Alzheimer Disease Neuropathologic Changes. *JAMA Neurol*. 2020. 77(7):829–39.
6. Edison P, Archer HA, Gerhard A, Hinz R, Pavese N, Turkheimer FE, et al. Microglia, amyloid, and cognition in Alzheimer's disease: An [^{11}C](R)PK11195-PET and [^{11}C]PIB-PET study. *Neurobiol Dis*. 2008. 32(3):412–9.
7. Keller T, López-Picón FR, Krzyczmonik A, Forsback S, Kirjavainen AK, Takkinen JS, et al. [^{18}F]F-DPA for the detection of activated microglia in a mouse model of Alzheimer's disease. *Nucl Med Biol*. 2018. 67:1–9.
8. López-Picón FR, Kirjavainen AK, Forsback S, Takkinen JS, Peters D, Haaparanta-Solin M, et al. In vivo characterization of a novel norepinephrine transporter PET tracer [^{18}F]NS12137 in adult and immature Sprague-Dawley rats. *Theranostics*. 2019. 9(1):11–9.
9. Sehlin D, Fang XT, Cato L, Antoni G, Lannfelt L, Syvänen S. Antibody-based PET imaging of amyloid beta in mouse models of Alzheimer's disease. *Nat Commun*. 2016. 7(1):1–11.
10. Xiong M, Roshanbin S, Rokka J, Schlein E, Ingelsson M, Sehlin D, et al. In vivo imaging of synaptic density with [^{11}C]UCB-J PET in two mouse models of neurodegenerative disease. *Neuroimage*. 2021. 239:118302.
11. Olsen M, Aguilar X, Sehlin D, Fang XT, Antoni G, Erlandsson A, et al. Astroglial Responses to Amyloid-Beta Progression in a Mouse Model of Alzheimer's Disease. *Mol Imaging Biol*. 2018. 20(4):605–14.
12. Brendel M, Yousefi BH, Blume T, Herz M, Focke C, Deussing M, et al. Comparison of ^{18}F-T807 and ^{18}F-THK5117 PET in a mouse model of tau pathology. *Front Aging Neurosci*. 2018. 10:174.
13. Snellman A, López-Picón FR, Rokka J, Salmona M, Forloni G, Scheinin M, et al. Longitudinal amyloid imaging in mouse brain with ^{11}C-PIB: Comparison of APP23, Tg2576, and APPswe-PS1dE9 mouse models of Alzheimer disease. *J Nucl Med*. 2013. 54(8):1434–41.
14. Takkinen JS, López-Picón FR, Al Majidi R, Eskola O, Krzyczmonik A, Keller T, et al. Brain energy metabolism and neuroinflammation in ageing APP/PS1-21 mice using longitudinal ^{18}F-FDG and ^{18}F-DPA-714 PET imaging. *J Cereb Blood Flow Metab*. 2017. 37(8):2870–82.

15. Chaney AM, Lopez-Picon FR, Serrière S, Wang R, Bochicchio D, Webb SD, et al. Prodromal neuroinflammatory, cholinergic and metabolite dysfunction detected by PET and MRS in the TgF344-AD transgenic rat model of AD: A collaborative multi-modal study. *Theranostics*. 2021. 11(14):6644–67.
16. Zhang L, López-Picón FR, Jia Y, Chen Y, Li J, Han C, et al. Longitudinal [^{18}F]FDG and [^{13}N]NH3 PET/CT imaging of brain and spinal cord in a canine hemisection spinal cord injury model. *NeuroImage Clin*. 2021. 31:102692.
17. Snellman A, Takkinen JS, López-Picón FR, Eskola O, Solin O, Rinne JO, et al. Effect of genotype and age on cerebral [^{18}F]FDG uptake varies between transgenic APP Swe -PS1 dE9 and Tg2576 mouse models of Alzheimer's disease. *Sci Rep*. 2019. 9(1):1–12.
18. Takkinen JS, López-Picón FR, Kirjavainen AK, Pihlaja R, Snellman A, Ishizu T, et al. [^{18}F]FMPEP-d_2 PET imaging shows age- and genotype-dependent impairments in the availability of cannabinoid receptor 1 in a mouse model of Alzheimer's disease. *Neurobiol Aging*. 2018. 69:199–208.
19. Anand K, Sabbagh M. Amyloid Imaging: Poised for Integration into Medical Practice. *Neurother*. 2017. 14:p 54–61.
20. Barthel H. First Tau PET tracer approved: Toward accurate in vivo diagnosis of Alzheimer disease. *J Nucl Med*. 2020. 61:p. 1409–10.
21. Jack CR, Knopman DS, Jagust WJ, Petersen RC, Weiner MW, Aisen PS, et al. Tracking pathophysiological processes in Alzheimer's disease: An updated hypothetical model of dynamic biomarkers. *Lancet Neurol*. 2013. 12:p. 207–16.
22. Dahm R. Alzheimer's discovery. *Curr Biol*. 2006. 16:p. R906–10.
23. Morley JE, Morris JC, Berg-Weger M, Borson S, Carpenter BD, del Campo N, et al. Brain Health: The Importance of Recognizing Cognitive Impairment: An IAGG Consensus Conference. *J Am Med Dir Assoc*. 2015. 16(9):731–9.
24. Harada CN, Natelson Love MC, Triebel KL. Normal cognitive aging. *Clin Geriatr Med*; 2013. 29:p. 737–52.
25. 2023 Alzheimer's disease facts and figures. *Alzheimer's Dement*. 2023. 19(4):1598–695.
26. Bennett DA, Schneider JA, Arvanitakis Z, Kelly JF, Aggarwal NT, Shah RC, et al. Neuropathology of older persons without cognitive impairment from two community-based studies. *Neurology*. 2006. 66(12):1837–44.
27. Knopman DS, Parisi JE, Salviati A, Floriach-Robert M, Boeve BF, Ivnik RJ, et al. Neuropathology of Cognitively Normal Elderly. *J Neuropathol Exp Neurol*. 2003. 62(11):1087–95.
28. Canevelli M, Grande G, Lacorte E, Quarchioni E, Cesari M, Mariani C, et al. Spontaneous Reversion of Mild Cognitive Impairment to Normal Cognition: A Systematic Review of Literature and Meta-Analysis. *J Am Med Dir Assoc*. 2016. 17(10):943–8.
29. Gauthier S, Reisberg B, Zaudig M, Petersen RC, Ritchie K, Broich K, et al. Mild cognitive impairment. *Lancet*. 2006. 367:p. 1262–70.
30. Sperling RA, Aisen PS, Beckett LA, Bennett DA, Craft S, Fagan AM, et al. Toward defining the preclinical stages of Alzheimer's disease: Recommendations from the National Institute on Aging-Alzheimer's Association workgroups on diagnostic guidelines for Alzheimer's disease. *Alzheimer's Dement*. 2011. 7(3):280–92.
31. Alzheimer's Association. Alzheimer's Stages - Early, Middle, Late Dementia Symptoms | alz.org. 2022. https://www.alz.org/alzheimers-dementia/stages

32. Beam CR, Kaneshiro C, Jang JY, Reynolds CA, Pedersen NL, Gatz M. Differences between Women and Men in Incidence Rates of Dementia and Alzheimer's Disease. *J Alzheimer's Dis*. 2018. 64(4):1077–83.
33. Thinking About Your Risk for Alzheimer's Disease? Five Questions To Consider | National Institute on Aging. https://www.nia.nih.gov/health/alzheimers-causes-and-risk-factors/thinking-about-your-risk-alzheimers-disease-five
34. Lott IT, Dierssen M. Cognitive deficits and associated neurological complications in individuals with Down's syndrome. *Lancet Neurol*. 2010. 9:p. 623–33.
35. Saunders AM, Strittmatter WJ, Schmechel D, St. George-Hyslop PH, Pericak-Vance MA, Joo SH, et al. Association of apolipoprotein E allele ϵ4 with late-onset familial and sporadic alzheimer's disease. *Neurology*. 1993. 43(8):1467–72.
36. Olufunmilayo EO, Holsinger RMD. Variant TREM2 Signaling in Alzheimer's Disease. *J Mol Biol*. 2022. 434:p. 167470.
37. Green RC, Cupples LA, Go R, Benke KS, Edeki T, Griffith PA, et al. Risk of dementia among white and African American relatives of patients with Alzheimer disease. *JAMA*. 2002. 287(3):329–36.
38. Loy CT, Schofield PR, Turner AM, Kwok JBJ. Genetics of dementia. *Lancet*. 2014. 383:p. 828–40.
39. Lautenschlager NT, Cupples LA, Rao VS, Auerbach SA, Becker R, Burke J, et al. Risk of dementia among relatives of Alzheimer's disease patients in the MIRAGE study: What is in store for the oldest old?. *Neurology*. 1996. 46(3):641–50.
40. Livingston G, Huntley J, Sommerlad A, Ames D, Ballard C, Banerjee S, et al. Dementia prevention, intervention, and care: 2020 report of the Lancet Commission. *Lancet*. 2020. 396:p. 413–46.
41. Ngandu T, Lehtisalo J, Solomon A, Levälahti E, Ahtiluoto S, Antikainen R, et al. A 2 year multidomain intervention of diet, exercise, cognitive training, and vascular risk monitoring versus control to prevent cognitive decline in at-risk elderly people (FINGER): A randomised controlled trial. *Lancet*. 2015. 385(9984):2255–63.
42. Reitz C, Brayne C, Mayeux R. Epidemiology of Alzheimer disease. Nat Rev Neurol. 2011. 7:p. 137–52.
43. Bekris LM, Yu CE, Bird TD, Tsuang DW. Review article: Genetics of Alzheimer disease. *J Geriatr Psychiatry Neurol*. 2010. 23:p. 213–27.
44. Goldman JS, Hahn SE, Catania JW, Larusse-Eckert S, Butson MB, Rumbaugh M, et al. Genetic counseling and testing for Alzheimer disease: Joint practice guidelines of the American College of Medical Genetics and the National Society of Genetic Counselors. *Genet Med*. 2011. 13(6):597–605.
45. McKhann G, Drachman D, Folstein M, Katzman R, Price D, Stadlan EM. Clinical diagnosis of alzheimer's disease: Report of the NINCDS-ADRDA work group⋆ under the auspices of department of health and human services task force on alzheimer's disease. *Neurology*. 1984. 34(7):939–44.
46. Dubois B, Feldman HH, Jacova C, Hampel H, Molinuevo JL, Blennow K, et al. Advancing research diagnostic criteria for Alzheimer's disease: The IWG-2 criteria. *Lancet Neurol*. 2014. 13:p. 614–29.
47. McKhann GM, Knopman DS, Chertkow H, Hyman BT, Jack CR, Kawas CH, et al. The diagnosis of dementia due to Alzheimer's disease: Recommendations from the National Institute on Aging-Alzheimer's Association workgroups on diagnostic guidelines for Alzheimer's disease. *Alzheimer's Dement*. 2011. 7(3):263–9.

48. Alzheimer's Association. Medical Tests for Diagnosing Alzheimer's & Dementia. 2023. Available from: https://www.alz.org/alzheimers-dementia/diagnosis/medical_tests
49. Dubois B, Villain N, Frisoni GB, Rabinovici GD, Sabbagh M, Cappa S, et al. Clinical diagnosis of Alzheimer's disease: recommendations of the International Working Group. *Lancet Neurol*. 2021. 20:p. 484–96.
50. Jack CR, Knopman DS, Jagust WJ, Petersen RC, Weiner MW, Aisen PS, et al. Tracking pathophysiological processes in Alzheimer's disease: An updated hypothetical model of dynamic biomarkers. *Lancet Neurol*. 2013. 12:p. 207–16.
51. Iaccarino L, Burnham SC, Dell'Agnello G, Dowsett SA, Epelbaum S. Diagnostic Biomarkers of Amyloid and Tau Pathology in Alzheimer's Disease: An Overview of Tests for Clinical Practice in the United States and Europe. *J Prev Alzheimers Dis*. 2023. 10:p. 426–42.
52. Ikonomovic MD, Klunk WE, Abrahamson EE, Mathis CA, Price JC, Tsopelas ND, et al. Post-mortem correlates of in vivo PiB-PET amyloid imaging in a typical case of Alzheimer's disease. Brain. 2008. 131(6):1630–45.
53. Tapiola T, Alafuzoff I, Herukka SK, Parkkinen L, Hartikainen P, Soininen H, et al. Cerebrospinal fluid β-amyloid 42 and tau proteins as biomarkers of Alzheimer-type pathologic changes in the brain. *Arch Neurol*. 2009. 66(3):382–9.
54. Fleisher AS, Pontecorvo MJ, Devous MD, Lu M, Arora AK, Truocchio SP, et al. Positron Emission Tomography Imaging with [^{18}F]flortaucipir and Postmortem Assessment of Alzheimer Disease Neuropathologic Changes. *JAMA Neurol*. 2020. 77(7):829–39.
55. Jack CR, Bennett DA, Blennow K, Carrillo MC, Dunn B, Haeberlein SB, et al. NIA-AA Research Framework: Toward a biological definition of Alzheimer's disease. *Alzheimer's Dement*. 2018. 14:p. 535–62.
56. Blennow K, Zetterberg H. The Past and the Future of Alzheimer's Disease Fluid Biomarkers *J Alzheimer's Dis*. 2018. 62:p. 1125–40.
57. Duboisa B, Padovanib A, Scheltensc P, Rossid A, Agnello GD. Timely diagnosis for alzheimer's disease: A literature review on benefits and challenges. *J Alzheimer's Dis*. 2015. 49(3):617–31.
58. Cummings J, Zhou Y, Lee G, Zhong K, Fonseca J, Cheng F. Alzheimer's disease drug development pipeline: 2023. *Alzheimer's Dement Transl Res Clin Interv*. 2023. 9(2).
59. Alzheimer's Association. Medications for Memory Loss | Alzheimer's Association. 2023. https://www.alz.org/alzheimers-dementia/treatments/medications-for-memory
60. van Bokhoven P, de Wilde A, Vermunt L, Leferink PS, Heetveld S, Cummings J, et al. The Alzheimer's disease drug development landscape. *Alzheimer's Res Ther*. 2021. 13(1):1–9.
61. Blennow K, de Leon MJ, Zetterberg H. Alzheimer's disease. *Lancet*. 2006. 368:p. 387–403.
62. Duyckaerts C, Delatour B, Potier MC. Classification and basic pathology of Alzheimer disease. *Acta Neuropathol*. 2009. 118:p. 5–36.
63. Querol-Vilaseca M, Colom-Cadena M, Pegueroles J, Nuñez-Llaves R, Luque-Cabecerans J, Muñoz-Llahuna L, et al. Nanoscale structure of amyloid-β plaques in Alzheimer's disease. *Sci Rep*. 2019. 9(1):1–10.
64. LaFerla FM, Oddo S. Alzheimer's disease: Aβ, tau and synaptic dysfunction. *Trends in Mol Med*. 2005. 11:p. 170–6.
65. Paasila PJ, Davies DS, Kril JJ, Goldsbury C, Sutherland GT. The relationship between the morphological subtypes of microglia and Alzheimer's disease neuropathology. *Brain Pathol*. 2019. 29(6):726–40.
66. Alzheimer's Disease Fact Sheet | National Institute on Aging. https://www.nia.nih.gov/health/alzheimers-disease-fact-sheet

67. Braak H, Braak E. Frequency of stages of Alzheimer-related lesions in different age categories. *Neurobiol Aging*. 1997. 18(4):351–7.
68. Braak H, Braak E. Neuropathological stageing of Alzheimer-related changes. *Acta Neuropathol*. 1991. 82:p. 239–59.
69. Gómez-Isla T, Hollister R, West H, Mui S, Growdon JH, Petersen RC, et al. Neuronal loss correlates with but exceeds neurofibrillary tangles in Alzheimer's disease. *Ann Neurol*. 1997. 41(1):17–24.
70. Whitwell JL, Josephs KA, Murray ME, Kantarci K, Przybelski SA, Weigand SD, et al. MRI correlates of neurofibrillary tangle pathology at autopsy: A voxel-based morphometry study. *Neurology*. 2008. 71(10):743–9.
71. Josephs KA, Whitwell JL, Ahmed Z, Shiung MM, Weigand SD, Knopman DS, et al. β-amyloid burden is not associated with rates of brain atrophy. *Ann Neurol*. 2008. 63(2):204–12.
72. Arriagada P V., Growdon JH, Hedley-Whyte ET, Hyman BT. Neurofibrillary tangles but not senile plaques parallel duration and severity of Alzheimer's disease. *Neurology*. 1992. 42(3):631–9.
73. Sengoku R. Aging and Alzheimer's disease pathology. *Neuropathology*. 2020. 40:p. 22–9.
74. Jucker M, Walker LC. Pathogenic protein seeding in Alzheimer disease and other neurodegenerative disorders. *Ann Neurol*. 2011. 70(4):532–40.
75. Kang J, Lemaire HG, Unterbeck A, Salbaum JM, Masters CL, Grzeschik KH, et al. The precursor of Alzheimer's disease amyloid A4 protein resembles a cell-surface receptor. *Nature*. 1987. 325(6106):733–6.
76. Haass C, Schlossmacher MG, Hung AY, Vigo-Pelfrey C, Mellon A, Ostaszewski BL, et al. Amyloid β-peptide is produced by cultured cells during normal metabolism. *Nature*. 1992. 359(6393):322–5.
77. Claeysen S, Cochet M, Donneger R, Dumuis A, Bockaert J, Giannoni P. Alzheimer culprits: Cellular crossroads and interplay. *Cell Signal*. 2012. 24:p. 1831–40.
78. Morley JE, Farr SA, Nguyen AD, Xu F. What is the Physiological Function of Amyloid-Beta Protein?. *J Nutr Health Aging*. 2019. 23:p. 225–6.
79. Dawkins E, Small DH. Insights into the physiological function of the β-amyloid precursor protein: Beyond Alzheimer's disease. *J Neurochem*. 2014. 129:p. 756–69.
80. Selkoe DJ, Hardy J. The amyloid hypothesis of Alzheimer's disease at 25 years. *EMBO Mol Med*. 2016. 8(6):595–608.
81. Shibata M, Yamada S, Ram Kumar S, Calero M, Bading J, Frangione B, et al. Clearance of Alzheimer's amyloid-β1-40 peptide from brain by LDL receptor-related protein-1 at the blood-brain barrier. *J Clin Invest*. 2000. 106(12):1489–99.
82. Tanzi RE, Moir RD, Wagner SL. Clearance of Alzheimer's Aβ peptide: The many roads to perdition. *Neuron*. 2004. 43:p. 605–8.
83. Pacheco-Quinto J, Herdt A, Eckman CB, Eckman EA. Endothelin-converting enzymes and related metalloproteases in Alzheimer's disease. *J Alzheimer's Dis*. 2013. 33:p. S101.
84. Carson JA, Turner AJ. β-amyloid catabolism: Roles for neprilysin (NEP) and other metallopeptidases?. *J Neurochem*. 2002. 81:p. 1–8.
85. MacPherson REK. Filling the void: A role for exercise-induced BDNF and brain amyloid precursor protein processing. American Journal of Physiology - Regulatory Integrative and Comparative Physiology. *Am J Physiol Regul Integr Comp Physiol*. 2017. 313:p. R585–93.
86. Grundke-Iqbal I, Iqbal K, Tung YC, Quinlan M, Wisniewski HM, Binder LI. Abnormal phosphorylation of the microtubule-associated protein tau (tau) in Alzheimer cytoskeletal pathology. *Proc Natl Acad Sci USA*. 1986. 83(13):4913–7.

87. Grundke-Iqbal I, Iqbal K, Quinlan M, Tung YC, Zaidi MS, Wisniewski HM. Microtubule-associated protein tau. A component of Alzheimer paired helical filaments. *J Biol Chem*. 1986. 261(13):6084–9.
88. Shi Y, Zhang W, Yang Y, Murzin AG, Falcon B, Kotecha A, et al. Structure-based classification of tauopathies. *Nature*. 2021. 598(7880):359–63.
89. Binder LI, Frankfurter A, Rebhun LI. The distribution of tau in the mammalian central nervous central nervous. *J Cell Biol*. 1985. 101(4):1371–8.
90. Hutton M, Lendon CL, Rizzu P, Baker M, Froelich S, Houlden HH, et al. Association of missense and 5'-splice-site mutations in tau with the inherited dementia FTDP-17. *Nature*. 1998. 393(6686):702–4.
91. Poorkaj P, Bird TD, Wijsman E, Nemens E, Garruto RM, Anderson L, et al. Tau is a candidate gene for chromosome 17 frontotemporal dementia. *Ann Neurol*. 1998. 43(6):815–25.
92. Goedert M, Spillantini MG, Potier MC, Ulrich J, Crowther RA. Cloning and sequencing of the cDNA encoding an isoform of microtubule-associated protein tau containing four tandem repeats: differential expression of tau protein mRNAs in human brain. *EMBO J*. 1989. 8(2):393–9.
93. Goedert M, Spillantini MG, Cairns NJ, Crowther RA. Tau proteins of alzheimer paired helical filaments: Abnormal phosphorylation of all six brain isoforms. *Neuron*. 1992. 8(1):159–68.
94. Zhang Y, Wu KM, Yang L, Dong Q, Yu JT. Tauopathies: new perspectives and challenges. *Mol Neurodegener*. 2022. 17:p. 1–29.
95. Drubin DG, Kirschner MW. Tau protein function in living cells. *J Cell Biol*. 1986. 103(6):2739–46.
96. Lindwall G, Cole RD. Phosphorylation affects the ability of tau protein to promote microtubule assembly. *J Biol Chem*. 1984. 259(8):5301–5.
97. Alonso ADC, Zaidi T, Grundke-Iqbal I, Iqbal K. Role of abnormally phosphorylated tau in the breakdown of microtubules in Alzheimer disease. *Proc Natl Acad Sci USA*. 1994. 91(12):5562–6.
98. Iqbal K, Liu F, Gong CX. Tau and neurodegenerative disease: The story so far. *Nat Rev Neurol*. 2016. 12:p. 15–27.
99. Liu F, Grundke-Iqbal I, Iqbal K, Gong CX. Contributions of protein phosphatases PP1, PP2A, PP2B and PP5 to the regulation of tau phosphorylation. *Eur J Neurosci*. 2005. 22(8):1942–50.
100. Iqbal K, Del C. Alonso A, Chen S, Chohan MO, El-Akkad E, Gong CX, et al. Tau pathology in Alzheimer disease and other tauopathies. *BBA*. 2005. 1739:p. 198–210.
101. Gong C -X, Singh TJ, Grundke-Iqbal I, Iqbal K. Phosphoprotein Phosphatase Activities in Alzheimer Disease Brain. *J Neurochem*. 1993. 61(3):921–7.
102. Gong C -X, Shaikh S, Wang J -Z, Zaidi T, Grundke-Iqbal I, Iqbal K. Phosphatase Activity Toward Abnormally Phosphorylated τ: Decrease in Alzheimer Disease Brain. *J Neurochem*. 1995. 65(2):732–8.
103. Alonso ADC, Zaidi T, Novak M, Grundke-Iqbal I, Iqbal K. Hyperphosphorylation induces self-assembly of τ into tangles of paired helical filaments/straight filaments. *Proc Natl Acad Sci USA*. 2001. 98(12):6923–8.
104. Sengupta A, Grundke-Iqbal I, Iqbal K. Regulation of phosphorylation of tau by protein kinases in rat brain. *Neurochem Res*. 2006. 31(12):1473–80.
105. Arnsten AFT, Datta D, Del Tredici K, Braak H. Hypothesis: Tau pathology is an initiating factor in sporadic Alzheimer's disease. *Alzheimer's Dement*. 2021. 17(1):115–24.
106. Leng F, Edison P. Neuroinflammation and microglial activation in Alzheimer disease: where do we go from here?. *Nat Rev Neurol*. 2021. 17:p. 157–72.

107. Colonna M, Butovsky O. Microglia function in the central nervous system during health and neurodegeneration. Annu Rev Immunol. 2017. 35:p. 441–68.
108. Nimmerjahn A, Kirchhoff F, Helmchen F. Neuroscience: Resting microglial cells are highly dynamic surveillants of brain parenchyma in vivo. *Science*. 2005. 308(5726):1314–8.
109. Norden DM, Godbout JP. Review: Microglia of the aged brain: Primed to be activated and resistant to regulation. *Neuropathol Appl Neurobiol*. 2013. 39:p. 19–34.
110. Spittau B. Aging microglia-phenotypes, functions and implications for age-related neurodegenerative diseases. *Front Aging Neurosci*. 2017. 9:267978.
111. Salter MW, Stevens B. Microglia emerge as central players in brain disease. *Nat Med*. 2017. 23:p.1018–27.
112. Glass CK, Saijo K, Winner B, Marchetto MC, Gage FH. Mechanisms Underlying Inflammation in Neurodegeneration. *Cell*. 2010. 140:p. 918–34.
113. Leyns CEG, Holtzman DM. Glial contributions to neurodegeneration in tauopathies. *Mol Neurodegener*. 2017. 12:p. 1–16.
114. Dani M, Wood M, Mizoguchi R, Fan Z, Walker Z, Morgan R, et al. Microglial activation correlates in vivo with both tau and amyloid in Alzheimer's disease. *Brain*. 2018. 141(9):2740–54.
115. Hayes A, Thaker U, Iwatsubo T, Pickering-Brown SM, Mann DMA. Pathological relationships between microglial cell activity and tau and amyloid β protein in patients with Alzheimer's disease. *Neurosci Lett*. 2002. 331(3):171–4.
116. McGeer PL, Itagaki S, Tago H, McGeer EG. Reactive microglia in patients with senile dementia of the Alzheimer type are positive for the histocompatibility glycoprotein HLA-DR. *Neurosci Lett*. 1987. 79(1–2):195–200.
117. Jacobs AH, Tavitian B. Noninvasive molecular imaging of neuroinflammation. *J Cereb Blood Flow Metab*. 2012. 32:p. 1393–415.
118. Perry VH, Nicoll JAR, Holmes C. Microglia in neurodegenerative disease. *Nat Rev Neurol*. 2010. 6:p. 193–201.
119. Pekny M, Wilhelmsson U, Pekna M. The dual role of astrocyte activation and reactive gliosis. *Neurosci. Lett.* 2014. 565:p. 30–8.
120. Liddelow SA, Guttenplan KA, Clarke LE, Bennett FC, Bohlen CJ, Schirmer L, et al. Neurotoxic reactive astrocytes are induced by activated microglia. *Nature*. 2017. 541(7638):481–7.
121. Rupprecht R, Papadopoulos V, Rammes G, Baghai TC, Fan J, Akula N, et al. Translocator protein (18 kDa) (TSPO) as a therapeutic target for neurological and psychiatric disorders. *Nat Rev Drug Discov*. 2010. 9:p. 971–88.
122. Papadopoulos V, Baraldi M, Guilarte TR, Knudsen TB, Lacapère JJ, Lindemann P, et al. Translocator protein (18 kDa): new nomenclature for the peripheral-type benzodiazepine receptor based on its structure and molecular function. *Trends Pharmacol Sci*. 2006. 27(8):402–9.
123. Papadopoulos V, Liu J, Culty M. Is there a mitochondrial signaling complex facilitating cholesterol import?. *Mol Cell Endocrinol*. 2007. 265–266:p. 59–64.
124. Cosenza-Nashat M, Zhao ML, Suh HS, Morgan J, Natividad R, Morgello S, et al. Expression of the translocator protein of 18 kDa by microglia, macrophages and astrocytes based on immunohistochemical localization in abnormal human brain. *Neuropathol Appl Neurobiol*. 2009. 35(3):306–28.

125. Gulyás B, Makkai B, Kása P, Gulya K, Bakota L, Várszegi S, et al. A comparative autoradiography study in post mortem whole hemisphere human brain slices taken from Alzheimer patients and age-matched controls using two radiolabelled DAA1106 analogues with high affinity to the peripheral benzodiazepine receptor (PBR) syst. *Neurochem Int*. 2009. 54(1):28–36.
126. Chauveau F, Boutin H, Van Camp N, Dollé F, Tavitian B. Nuclear imaging of neuroinflammation: A comprehensive review of [^{11}C]PK11195 challengers. *EJNMMI*. 2008. 35:p. 2304–19.
127. Bartlett R, Stokes L, Sluyter R. The p2x7 receptor channel: Recent developments and the use of p2x7 antagonists in models of disease. *Pharmacol Rev*. 2014. 66(3):638–75.
128. Sperlágh B, Vizi ES, Wirkner K, Illes P. P2X7 receptors in the nervous system. *Prog Neurobiol*. 2006. 78:p. 327–46.
129. Oliveira-Giacomelli ágatha, Naaldijk Y, Sardá-Arroyo L, Gonçalves MCB, Corrêa-Velloso J, Pillat MM, et al. Purinergic receptors in neurological diseases with motor symptoms: Targets for therapy. *Front Pharmacol*. 2018. 9:p. 331754.
130. Duyckaerts C, Potier MC, Delatour B. Alzheimer disease models and human neuropathology: Similarities and differences. *Acta Neuropathol*. 2008. 115:p. 5–38.
131. Kitazawa M, Medeiros R, M. LaFerla F. Transgenic Mouse Models of Alzheimer Disease: Developing a Better Model as a Tool for Therapeutic Interventions. *Curr Pharm Des*. 2012. 18(8):1131–47.
132. Chin J. Selecting a mouse model of Alzheimer's disease. *Methods Mol Biol*. 2011. 670:169–89.
133. Research Models. ALZFORUM. 2021. https://www.alzforum.org/research-models/search?species=&diseases%5B%5D=145&genes=&types=&keywords-entry=&keywords=#results
134. Radde R, Bolmont T, Kaeser SA, Coomaraswamy J, Lindau D, Stoltze L, et al. Aβ42-driven cerebral amyloidosis in transgenic mice reveals early and robust pathology. *EMBO Rep*. 2006. 7(9):940–6.
135. Cohen RM, Rezai-Zadeh K, Weitz TM, Rentsendorj A, Gate D, Spivak I, et al. A transgenic alzheimer rat with plaques, tau pathology, behavioral impairment, oligomeric Aβ, and frank neuronal loss. *J Neurosci*. 2013. 33(15):6245–56.
136. Barghorn S, Zheng-Fischhofer Q, Ackmann M, Biernat J, Von Bergen M, Mandelkow EM, et al. Structure, microtubule interactions, and paired helical filament aggregation by tau mutants of frontotemporal dementias. *Biochem*. 2000. 39(38):11714–21.
137. Allen B, Ingram E, Takao M, Smith MJ, Jakes R, Virdee K, et al. Abundant tau filaments and nonapoptotic neurodegeneration in transgenic mice expressing human P301s tau protein. *J Neurosci*. 2002. 22(21):9340–51.
138. Oddo S, Caccamo A, Shepherd JD, Murphy MP, Golde TE, Kayed R, et al. Triple-transgenic model of Alzheimer's Disease with plaques and tangles: Intracellular Aβ and synaptic dysfunction. *Neuron*. 2003. 39(3):409–21.
139. Zhang H, Wang H, Gao F, Yang J, Xu Y, Fu Y, et al. TSPO deficiency accelerates amyloid pathology and neuroinflammation by impairing microglial phagocytosis. *Neurobiol Aging*. 2021. 106:292–303.
140. Parvathenani LK, Tertyshnikova S, Greco CR, Roberts SB, Robertson B, Posmantur R. P2X7 mediates superoxide production in primary microglia and is up-regulated in a transgenic mouse model of Alzheimer's disease. *J Biol Chem*. 2003. 278(15):13309–17.

141. Gratuze M, Leyns CEG, Sauerbeck AD, St-Pierre MK, Xiong M, Kim N, et al. Impact of TREM2^{R47H} variant on tau pathology-induced gliosis and neurodegeneration. *J Clin Invest*. 2020. 130(9):4954–68.
142. Van Dam D, De Deyn PP. Animal models in the drug discovery pipeline for Alzheimer's disease. *Br J Pharmacol*. 2011. 164:p. 1285–300.
143. Ghosh KK, Padmanabhan P, Yang CT, Ng DCE, Palanivel M, Mishra S, et al. Positron emission tomographic imaging in drug discovery. *Drug Discov Today*. 2022. 27:p. 280–91.
144. Hanseeuw BJ, Betensky RA, Jacobs HIL, Schultz AP, Sepulcre J, Becker JA, et al. Association of Amyloid and Tau with Cognition in Preclinical Alzheimer Disease: A Longitudinal Study. *JAMA Neurol*. 2019. 76(8):915–24.
145. Sevigny J, Chiao P, Bussière T, Weinreb PH, Williams L, Maier M, et al. The antibody aducanumab reduces Aβ plaques in Alzheimer's disease. *Nature*. 2016. 537(7618):50–6.
146. Nerella SG, Singh P, Sanam T, Digwal CS. PET Molecular Imaging in Drug Development: The Imaging and Chemistry Perspective. *Front Med*. 2022. 9:p.812270.
147. Khalil MM. Basic Science of PET Imaging [Chapter title]. Basic Science of PET Imaging. *Springer*. 2016. https://link.springer.com/content/pdf/10.1007%2F978-3-319-40070-9.pdf
148. Cherry SR, Dahlbom M. PET: Physics, Instrumentation, and Scanners. *Springer*. 2006. https://link.springer.com/chapter/10.1007/0-387-34946-4_1
149. Fowler JS, Volkow ND. Molecular Imaging: Positron Emission Tomography. Neuroscience in the 21st Century. *Springer*. 2016. https://link.springer.com/referenceworkentry/10.1007/978-1-4614-6434-1_149-2
150. Rudroff T, Kindred JH, Kalliokoski KK. [^{18}F]-FDG positron emission tomography—an established clinical tool opening a new window into exercise physiology. *J Appl Physiol*. 2015. 118(10):1181–90.
151. Rahmim A, Zaidi H. PET versus SPECT: Strengths, limitations and challenges. *Nucl Med Commun*. 2008. 29:p. 193–207.
152. Gambhir SS. Quantitative Assay Development for PET. *Springer*. 2004. https://link.springer.com/chapter/10.1007/978-0-387-22529-6_2
153. Zhang L, Villalobos A. Strategies to facilitate the discovery of novel CNS PET ligands. *EJNMMI Radiopharm Chem*. 2016. 1:p. 1–12.
154. Need A, Kant N, Jesudason C, Barth V. Approaches for the discovery of novel positron emission tomography radiotracers for brain imaging. *Clin Transl Imaging*. 2017. 5:p. 265–74.
155. Lau J, Rousseau E, Kwon D, Lin KS, Bénard F, Chen X. Insight into the development of PET radiopharmaceuticals for oncology. *Cancers*. 2020.
156. Alzghool OM, van Dongen G, van de Giessen E, Schoonmade L, Beaino W. α-Synuclein Radiotracer Development and In Vivo Imaging: Recent Advancements and New Perspectives. *Mov Disord*. 2022. 37:p. 936–48.
157. Mathis CA, Lopresti BJ, Ikonomovic MD, Klunk WE. Small-molecule PET Tracers for Imaging Proteinopathies. *Semin Nucl Med*. 2017. 47:p. 553–75.
158. Pike VW. PET radiotracers: crossing the blood-brain barrier and surviving metabolism. *Trends Pharmacol Sci*. 2009. 30:p. 431–40.
159. W. Pike V. Considerations in the Development of Reversibly Binding PET Radioligands for Brain Imaging. *Curr Med Chem*. 2016. 23(18):1818–69.
160. Korat Š, Bidesi NSR, Bonanno F, Di Nanni A, Hoàng ANN, Herfert K, et al. Alpha-Synuclein PET tracer development-an overview about current efforts. *Pharm*. 2021. 14:p. 847.

161. McCluskey SP, Plisson C, Rabiner EA, Howes O. Advances in CNS PET: the state-of-the-art for new imaging targets for pathophysiology and drug development. *EJNMMI*. 2020. 47:p. 451–89.
162. Waterhouse RN. Determination of lipophilicity and its use as a predictor of blood-brain barrier penetration of molecular imaging agents. *Mol Imaging Biol*. 2003. 5(6):376–89.
163. Ghosh KK, Padmanabhan P, Yang CT, Mishra S, Halldin C, Gulyás B. Dealing with PET radiometabolites. *EJNMMI Research*. 2020. 10:p. 1–17.
164. Deb PK, Al-Attraqchi O, Prasad MR, Tekade RK. Protein and Tissue Binding: Implication on Pharmacokinetic Parameters. *Dosage Form Design Considerations*. 2018. I:p. 371–99.
165. Eriksson O, Laughlin M, Brom M, Nuutila P, Roden M, Hwa A, et al. In vivo imaging of beta cells with radiotracers: state of the art, prospects and recommendations for development and use. *Diabetologia*. 2016. 59:p. 1340–9.
166. Harada R, Okamura N, Furumoto S, Tago T, Yanai K, Arai H, et al. Characteristics of tau and its ligands in PET imaging. *Biomolecules*. 2016. 6:p. 2–15.
167. Okamura N, Harada R, Ishiki A, Kikuchi A, Nakamura T, Kudo Y. The development and validation of tau PET tracers: current status and future directions. *Clin Transl Imaging*. 2018. 6:p. 305–16.
168. Okamura N, Harada R, Furumoto S, Arai H, Yanai K, Kudo Y. Tau PET Imaging in Alzheimer's Disease. *Curr Neurol Neurosci Rep*. 2014. 14:p.500.
169. Leuzy A, Chiotis K, Lemoine L, Gillberg PG, Almkvist O, Rodriguez-Vieitez E, et al. Tau PET imaging in neurodegenerative tauopathies—still a challenge. *Mol Psychiatry*. 2019.1.
170. Kroth H, Oden F, Molette J, Schieferstein H, Capotosti F, Mueller A, et al. Discovery and preclinical characterization of [^{18}F]PI-2620, a next-generation tau PET tracer for the assessment of tau pathology in Alzheimer's disease and other tauopathies. *Eur J Nucl Med Mol Imaging*. 2019. 46(10):2178–89.
171. Hostetler ED, Walji AM, Zeng Z, Miller P, Bennacef I, Salinas C, et al. Preclinical Characterization of ^{18}F-MK-6240, a Promising PET Tracer for In Vivo Quantification of Human Neurofibrillary Tangles. *J Nucl Med*. 2016. 57(10):1599–606.
172. Sanabria Bohórquez S, Marik J, Ogasawara A, Tinianow JN, Gill HS, Barret O, et al. [^{18}F]GTP1 (Genentech Tau Probe 1), a radioligand for detecting neurofibrillary tangle tau pathology in Alzheimer's disease. *EJNMMI*. 2019. 46(10):2077–89.
173. Mueller A, Bullich S, Barret O, Madonia J, Berndt M, Papin C, et al. Tau PET imaging with ^{18}F-PI-2620 in patients with Alzheimer disease and healthy controls: A first-in-humans study. *J Nucl Med*. 2020. 61(6):911–9.
174. Rullmann M, Brendel M, Schroeter ML, Saur D, Levin J, Perneczky RG, et al. Multicenter ^{18}F-PI-2620 PET for In Vivo Braak Staging of Tau Pathology in Alzheimer's Disease. *Biomolecules*. 2022. 12(3):458.
175. Cassinelli Petersen G, Roytman M, Chiang GC, Li Y, Gordon ML, Franceschi AM. Overview of tau PET molecular imaging. *Curr Opin Neurol*. 2022. 35:p. 230–9.
176. Teng E, Ward M, Manser PT, Sanabria-Bohorquez S, Ray RD, Wildsmith KR, et al. Cross-sectional associations between [^{18}F]GTP1 tau PET and cognition in Alzheimer's disease. *Neurobiol Aging*. 2019. 81:138–45.
177. Baker SL, Provost K, Thomas W, Whitman AJ, Janabi M, Schmidt ME, et al. Evaluation of [^{18}F]-JNJ-64326067-AAA tau PET tracer in humans. *J Cereb Blood Flow Metab*. 2021. 41(12):3302–13.

178. Declercq L, Rombouts F, Koole M, Fierens K, Mariën J, Langlois X, et al. Preclinical evaluation of ^{18}F-JNJ64349311, a novel PET tracer for tau imaging. *J Nucl Med*. 2017. 58(6):975–81.
179. Chapleau M, Iaccarino L, Soleimani-Meigooni D, Rabinovici GD. The Role of Amyloid PET in Imaging Neurodegenerative Disorders: A Review. *J Nucl Med*. 2022. 63:13S-19S.
180. Mallik A, Drzezga A, Minoshima S. Clinical Amyloid Imaging. *Semin Nucl Med*. 2017. 47:p. 31–43.
181. Janssen B, Vugts DJ, Funke U, Spaans A, Schuit RC, Kooijman E, et al. Synthesis and initial preclinical evaluation of the P2X7 receptor antagonist [^{11}C]A-740003 as a novel tracer of neuroinflammation. *J Label Compd Radiopharm*. 2014. 57(8):509–16.
182. Fantoni ER, Dal Ben D, Falzoni S, Di Virgilio F, Lovestone S, Gee A. Design, synthesis and evaluation in an LPS rodent model of neuroinflammation of a novel ^{18}F-labelled PET tracer targeting P2X7. *EJNMMI Res*. 2017. 7(1):1–12.
183. Han J, Liu H, Liu C, Jin H, Perlmutter JS, Egan TM, et al. Pharmacologic characterizations of a P2X7 receptor-specific radioligand, [^{11}C]GSK1482160 for neuroinflammatory response. *Nucl Med Commun*. 2017. 38(5):372–82.
184. Territo PR, Meyer JA, Peters JS, Riley AA, McCarthy BP, Gao M, et al. Characterization of ^{11}C-GSK1482160 for Targeting the P2X7 receptor as a biomarker for neuroinflammation. *J Nucl Med*. 2017. 58(3):458–65.
185. Green M, Hutchins G, Fletcher J, Territo W, Polson H, Trussell H, et al. Distribution of the P2X7-receptor-targeted [^{11}C]GSK1482160 radiopharmaceutical in normal human subjects. *J Nucl Med*. 2018. 59:1009 LP – 1009.
186. Gao M, Wang M, Meyer JA, Territo PR, Hutchins GD, Zarrinmayeh H, et al. Synthesis and in vitro biological evaluation of new P2X7R radioligands [^{11}C]halo-GSK1482160 analogs. *Bioorganic Med Chem Lett*. 2019. 29(12):1476–80.
187. Gao M, Wang M, Glick-Wilson BE, Meyer JA, Peters JS, Territo PR, et al. Synthesis and preliminary biological evaluation of a novel P2X7R radioligand [^{18}F]IUR-1601. *Bioorganic Med Chem Lett*. 2018. 28(9):1603–9.
188. Gao M, Wang M, Glick-Wilson BE, Meyer JA, Peters JS, Territo PR, et al. Synthesis and initial in vitro characterization of a new P2X7R radioligand [^{18}F]IUR-1602. *Appl Radiat Isot*. 2019. 144:10–8.
189. Jin H, Han J, Resing D, Liu H, Yue X, Miller RL, et al. Synthesis and in vitro characterization of a P2X7 radioligand [^{123}I]TZ6019 and its response to neuroinflammation in a mouse model of Alzheimer disease. *Eur J Pharmacol*. 2018. 5;820:8–17.
190. Ory D, Celen S, Gijsbers R, Haute C Van Den, Postnov A, Koole M, et al. Preclinical evaluation of a P2X7 receptor-selective radiotracer: PET studies in a rat model with local overexpression of the human p2x7 receptor and in nonhuman primates. *J Nucl Med*. 2016. 57(9):1436–41.
191. Kolb HC, Barret O, Bhattacharya A, Chen G, Constantinescu C, Huang C, et al. Preclinical evaluation and nonhuman primate receptor occupancy study of ^{18}F-JNJ-64413739, a PET radioligand for P2X7 receptors. *J Nucl Med*. 2019. 60(8):1154–9.
192. Berdyyeva T, Xia C, Taylor N, He Y, Chen G, Huang C, et al. PET Imaging of the P2X7 Ion Channel with a Novel Tracer [^{18}F]JNJ-64413739 in a Rat Model of Neuroinflammation. *Mol Imaging Bio*l. 2019. 21(5):871–8.

193. Koole M, Schmidt ME, Hijzen A, Ravenstijn P, Vandermeulen C, Van Weehaeghe D, et al. ^{18}F-JNJ-64413739, a novel PET ligand for the P2X7 ion channel: Radiation dosimetry, kinetic modeling, test-retest variability, and occupancy of the P2X7 antagonist JNJ-54175446. *J Nucl Med*. 2019. 60(5):683–90.
194. Van Weehaeghe D, Koole M, Schmidt ME, Deman S, Jacobs AH, Souche E, et al. [^{11}C]JNJ54173717, a novel P2X7 receptor radioligand as marker for neuroinflammation: human biodistribution, dosimetry, brain kinetic modelling and quantification of brain P2X7 receptors in patients with Parkinson's disease and healthy volunteers. *EJNMMI*. 2019. 46(10):2051–64.
195. van Weehaeghe D, van Schoor E, de Vocht J, Koole M, Attili B, Celen S, et al. TSPO versus P2X7 as a target for neuroinflammation: An in vitro and in vivo study. *J Nucl Med*. 2020. 61(4):604–7.
196. Beaino W, Janssen B, Kooijman E, Vos R, Schuit RC, O'Brien-Brown J, et al. PET imaging of P2X7R in the experimental autoimmune encephalomyelitis model of multiple sclerosis using [^{11}C]SMW139. *J Neuroinflammation*. 2020. 17(1):300.
197. Janssen B, Vugts DJ, Wilkinson SM, Ory D, Chalon S, Hoozemans JJM, et al. Identification of the allosteric P2X7 receptor antagonist [^{11}C]SMW139 as a PET tracer of microglial activation. *Sci Rep*. 2018. 8(1).
198. Beaino W, Janssen B, Kooij G, van der Pol SMA, van Het Hof B, van Horssen J, et al. Purinergic receptors P2Y12R and P2X7R: Potential targets for PET imaging of microglia phenotypes in multiple sclerosis. *J Neuroinflammatio*n. 2017. 14(1):259.
199. Hagens MHJ, Golla SSV, Janssen B, Vugts DJ, Beaino W, Windhorst AD, et al. The P2X7 receptor tracer [^{11}C]SMW139 as an in vivo marker of neuroinflammation in multiple sclerosis: a first-in man study. *EJNMMI*. 2020. 47(2):379–89.
200. Brumberg J, Aarnio R, Forsberg A, Marjamäki P, Kerstens V, Moein MM, et al. Quantification of the purinergic P2X7 receptor with [^{11}C]SMW139 improves through correction for brain-penetrating radiometabolites. *J Cereb Blood Flow Metab*. 2023. 43(2):258–68.
201. Percie du Sert N, Hurst V, Ahluwalia A, Alam S, Avey MT, Baker M, et al. The ARRIVE guidelines 2.0: Updated guidelines for reporting animal research. *Br J Pharmacol*. 2020. 177(16):3617–24.
202. Okamura N, Furumoto S, Harada R, Tago T, Yoshikawa T, Fodero-Tavoletti M, et al. Novel ^{18}F-Labeled Arylquinoline Derivatives for Noninvasive Imaging of Tau Pathology in Alzheimer Disease. *J Nucl Me*d. 2013. 54(8):1420–7.
203. Aarnio R, Alzghool OM, Wahlroos S, O'Brien-Brown J, Kassiou M, Solin O, et al. Novel plasma protein binding analysis method for a PET tracer and its radiometabolites: A case study with [^{11}C]SMW139 to explain the high uptake of radiometabolites in mouse brain. *J Pharm Biomed Anal*. 2022. 219:114860.
204. Keller T, Krzyczmonik A, Forsback S, Picón FRL, Kirjavainen AK, Takkinen J, et al. Radiosynthesis and Preclinical Evaluation of [^{18}F]F-DPA, A Novel Pyrazolo[1,5a]pyrimidine Acetamide TSPO Radioligand, in Healthy Sprague Dawley Rats. *Mol Imaging Biol*. 2017. 19(5):736–45.
205. Bankhead P, Loughrey MB, Fernández JA, Dombrowski Y, McArt DG, Dunne PD, et al. QuPath: Open source software for digital pathology image analysis. *Sci Rep*. 2017. 7(1):1–7.
206. Wang CY, Yeh IH, Liao HYM. You Only Learn One Representation: Unified Network for Multiple Tasks. 2021. https://arxiv.org/abs/2105.04206v1

207. MacGregor RR, Halldin C, Fowler JS, Wolf AP, Arnett CD, Langström B, et al. Selective, irreversible in vivo binding of [^{11}C]clorgyline and [^{11}C]-L-deprenyl in mice: Potential for measurement of functional monoamine oxidase activity in brain using positron emission tomography. *Biochem Pharmacol*. 1985. 34(17):3207–10.
208. Zoufal V, Mairinger S, Krohn M, Wanek T, Filip T, Sauberer M, et al. Measurement of cerebral ABCC1 transport activity in wild-type and APP/PS1-21 mice with positron emission tomography. *J Cereb Blood Flow Metab*. 2020. 40(5):954–65.
209. Zoufal V, Mairinger S, Brackhan M, Krohn M, Filip T, Sauberer M, et al. Imaging p-glycoprotein induction at the blood-brain barrier of a β-amyloidosis mouse model with ^{11}C-metoclopramide PET. *J Nucl Med*. 2020. 61(7):1050–7.
210. Poisnel G, Dhilly M, Moustié O, Delamare J, Abbas A, Guilloteau D, et al. PET imaging with [^{18}F]AV-45 in an APP/PS1-21 murine model of amyloid plaque deposition. *Neurobiol Aging*. 2012. 33(11):2561–71.
211. Mahan TE, Wang C, Bao X, Choudhury A, Ulrich JD, Holtzman DM. Selective reduction of astrocyte apoE3 and apoE4 strongly reduces Aβ accumulation and plaque-related pathology in a mouse model of amyloidosis. *Mol Neurodegene*r. 2022. 17(1):1–20.
212. Paumier A, Boisseau S, Jacquier-Sarlin M, Pernet-Gallay K, Buisson A, Albrieux M. Astrocyte-neuron interplay is critical for Alzheimer's disease pathogenesis and is rescued by TRPA1 channel blockade. *Brain*. 2022. 145(1):388–405.
213. Alzforum. APPPS1 | Alzforum. 2020. https://www.alzforum.org/research-models/appps1
214. Radde R, Duma C, Goedert M, Jucker M. The value of incomplete mouse models of Alzheimer's disease. *EJNMMI*. 2008. 35:70–4.
215. Jonasson M, Wall A, Chiotis K, Saint-Aubert L, Wilking H, Sprycha M, et al. Tracer Kinetic Analysis of (*S*)-^{18}F-THK5117 as a PET Tracer for Assessing Tau Pathology. *J Nucl Med*. 2016. 57(4):574–81.
216. Tago T, Furumoto S, Okamura N, Harada R, Adachi H, Ishikawa Y, et al. Structure-Activity Relationship of 2-Arylquinolines as PET Imaging Tracers for Tau Pathology in Alzheimer Disease. *J Nucl Med*. 2016. 57(4):608–14.
217. Mairinger S, Filip T, Sauberer M, Flunkert S, Wanek T, Stanek J, et al. Plasma pharmacokinetic and metabolism of [^{18}F]THK-5317 are dependent on sex. *Nucl Med Biol*. 2020. 84–85:28–32.
218. Filip T, Mairinger S, Neddens J, Sauberer M, Flunkert S, Stanek J, et al. Characterization of an APP/tau rat model of Alzheimer's disease by positron emission tomography and immunofluorescent labeling. *Alzheimer's Res Ther*. 2021. 13(1):1–13.
219. Brendel M, Jaworska A, Probst F, Overhoff F, Korzhova V, Lindner S, et al. Small-Animal PET Imaging of Tau Pathology with ^{18}F-THK5117 in 2 Transgenic Mouse Models. *J Nucl Med*. 2016. 57(5):792–8.
220. Tago T, Furumoto S, Okamura N, Harada R, Adachi H, Ishikawa Y, et al. Preclinical Evaluation of [^{18}F]THK-5105 Enantiomers: Effects of Chirality on Its Effectiveness as a Tau Imaging Radiotracer. *Mol Imaging Biol*. 2016. 18(2):258–66.
221. Lemoine L, Saint-Aubert L, Marutle A, Antoni G, Eriksson JP, Ghetti B, et al. Visualization of regional tau deposits using ^{3}H-THK5117 in Alzheimer brain tissue. *Acta Neuropathol Commun*. 2015. 3(1):40.
222. Chiotis K, Saint-Aubert L, Savitcheva I, Jelic V, Andersen P, Jonasson M, et al. Imaging in-vivo tau pathology in Alzheimer's disease with THK5317 PET in a multimodal paradigm. *EJNMMI*. 2016. 43(9):1686–99.

223. Betthauser TJ, Lao PJ, Murali D, Barnhart TE, Furumoto S, Okamura N, et al. In Vivo Comparison of Tau Radioligands ^{18}F-THK-5351 and ^{18}F-THK-5317. *J Nucl Med*. 2017. 58(6):996–1002.
224. Ishiki A, Okamura N, Furukawa K, Furumoto S, Harada R, Tomita N, et al. Longitudinal assessment of Tau pathology in patients with Alzheimer's disease using [^{18}F]THK-5117 positron emission tomography. *PLoS One* . 2015. 10(10):e0140311.
225. Jonasson M, Wall A, Chiotis K, Leuzy A, Eriksson J, Antoni G, et al. Optimal timing of tau pathology imaging and automatic extraction of a reference region using dynamic [^{18}F]THK5317 PET. *NeuroImage Clin*. 2019. 22:101681.
226. Rodriguez-Vieitez E, Leuzy A, Chiotis K, Saint-Aubert L, Wall A, Nordberg A. Comparability of [^{18}F]THK5317 and [^{11}C]PIB blood flow proxy images with [^{18}F]FDG positron emission tomography in Alzheimer's disease. *J Cereb Blood Flow Metab*. 2017. 37(2):740–9.
227. Colato E, Chiotis K, Ferreira D, Mazrina MS, Lemoine L, Mohanty R, et al. Assessment of Tau Pathology as Measured by ^{18}F-THK5317 and ^{18}F-Flortaucipir PET and Their Relation to Brain Atrophy and Cognition in Alzheimer's Disease. *J Alzheimer's Dis*. 2021. 84(1):103–17.
228. Chiotis K, Savitcheva I, Poulakis K, Saint-Aubert L, Wall A, Antoni G, et al. [^{18}F]THK5317 imaging as a tool for predicting prospective cognitive decline in Alzheimer's disease. *Mol Psychiatry*. 2021. 26(10):5875–87.
229. Leinonen V, Rauramaa T, Johansson J, Bottelbergs A, Tesseur I, Van Der Ark P, et al. *S*-[^{18}F]THK-5117-PET and [^{11}C]PIB-PET Imaging in Idiopathic Normal Pressure Hydrocephalus in Relation to Confirmed Amyloid-β Plaques and Tau in Brain Biopsies. *J Alzheimer's Dis*. 2018. 64(1):171–9.
230. Lemoine L, Saint-Aubert L, Nennesmo I, Gillberg PG, Nordberg A. Cortical laminar tau deposits and activated astrocytes in Alzheimer's disease visualised by ^{3}H-THK5117 and ^{3}H-deprenyl autoradiography. *Sci Rep*. 2017. 7(1):45496.
231. Lemoine L, Gillberg PG, Svedberg M, Stepanov V, Jia Z, Huang J, et al. Comparative binding properties of the tau PET tracers THK5117, THK5351, PBB3, and T807 in postmortem Alzheimer brains. *Alzheimer's Res Ther*. 2017. 9(1):96.
232. Murugan NA, Chiotis K, Rodriguez-Vieitez E, Lemoine L, Ågren H, Nordberg A. Cross-interaction of tau PET tracers with monoamine oxidase B: evidence from in silico modelling and in vivo imaging. *EJNMMI*. 2019. 46(6):1369–82.
233. Ng KP, Pascoal TA, Mathotaarachchi S, Therriault J, Kang MS, Shin M, et al. Monoamine oxidase B inhibitor, selegiline, reduces ^{18}F-THK5351 uptake in the human brain. *Alzheimer's Res Ther*. 2017. 9(1):25.
234. Jo S, Yarishkin O, Hwang YJ, Chun YE, Park M, Woo DH, et al. GABA from reactive astrocytes impairs memory in mouse models of Alzheimer's disease. *Nat Med*. 2014. 20:p. 886–96.
235. Carter SF, Schöll M, Almkvist O, Wall A, Engler H, Långström B, et al. Evidence for astrocytosis in prodromal alzheimer disease provided by ^{11}C-deuterium-L-deprenyl: A multitracer PET paradigm combining ^{11}C-Pittsburgh compound B and ^{18}F-FDG. *J Nucl Med*. 2012. 53(1):37–46.
236. Fowler JS, MacGregor RR, Wolf AP, Arnett CD, Dewey SL, Schlyer D, et al. Mapping human brain monoamine oxidase a and B with ^{11}C-labeled suicide inactivators and PET. *Science*. 1987. 235(4787):481–5.
237. Lemoine L, Leuzy A, Chiotis K, Rodriguez-Vieitez E, Nordberg A. Tau positron emission tomography imaging in tauopathies: The added hurdle of off-target binding. *Alzheimer's Dement Diagnosis*. 2018. 10:232–6.

238. Limorenko G, Lashuel HA. Revisiting the grammar of Tau aggregation and pathology formation: How new insights from brain pathology are shaping how we study and target Tauopathies. *Chem Soc Rev.* 2022. 51:p.513–65.
239. Kirschner DA, Abraham C, Selkoe DJ. X-ray diffraction from intraneuronal paired helical filaments and extraneuronal amyloid fibers in Alzheimer disease indicates cross-beta conformation. *Proc Natl Acad Sci*. 1986. 83(2):503–7.
240. Näslund J, Haroutunian V, Mohs R, Davis KL, Davies P, Greengard P, et al. Correlation between elevated levels of amyloid β-peptide in the brain and cognitive decline. *JAMA*. 2000. 283(12):1571–7.
241. Syvänen S, Fang XT, Hultqvist G, Meier SR, Lannfelt L, Sehlin D. A bispecific Tribody PET radioligand for visualization of amyloid-beta protofibrils – a new concept for neuroimaging. *Neuroimage*. 2017. 148:55–63.
242. Sehlin D, Fang XT, Meier SR, Jansson M, Syvänen S. Pharmacokinetics, biodistribution and brain retention of a bispecific antibody-based PET radioligand for imaging of amyloid-β. *Sci Rep*. 2017. 7(1).
243. Syvänen S, Hultqvist G, Gustavsson T, Gumucio A, Laudon H, Söderberg L, et al. Efficient clearance of Aβ protofibrils in AβPP-transgenic mice treated with a brain-penetrating bifunctional antibody. *Alzheimer's Res Ther*. 2018. 10(1):49.
244. Parvathenani LK, Tertyshnikova S, Greco CR, Roberts SB, Robertson B, Posmantur R. P2X7 mediates superoxide production in primary microglia and is up-regulated in a transgenic mouse model of Alzheimer's disease. *J Biol Chem*. 2003. 278(15):13309–17.
245. Lee HG, Won SM, Gwag BJ, Lee YB. Microglial P2X7 receptor expression is accompanied by neuronal damage in the cerebral cortex of the APPswe/PS1dE9 mouse model of alzheimer's disease. *Exp Mol Med*. 2011. 43(1):7–14.
246. McLarnon JG, Ryu JK, Walker DG, Choi HB. Upregulated expression of purinergic P2X7 receptor in Alzheimer disease and amyloid-β peptide-treated microglia and in peptide-injected rat hippocampus. *J Neuropathol Exp Neurol*. 2006. 65(11):1090–7.
247. López-Picón FR, Keller T, Bocancea D, Helin JS, Krzyczmonik A, Helin S, et al. Direct Comparison of [^{18}F]F-DPA with [^{18}F]DPA-714 and [^{11}C]PBR28 for Neuroinflammation Imaging in the same Alzheimer's Disease Model Mice and Healthy Controls. *Mol Imaging Bio*l. 2022. 24(1):157–66.
248. Vuignier K, Schappler J, Veuthey JL, Carrupt PA, Martel S. Drug-protein binding: A critical review of analytical tools. *Anal Bioanal Chem*. 398:p. 53–66.
249. Roberts JA, Pea F, Lipman J. The clinical relevance of plasma protein binding changes. *Clin Pharmacokinet*. 52:p.1–8.
250. Wilkinson SM, Barron ML, O'Brien-Brown J, Janssen B, Stokes L, Werry EL, et al. Pharmacological Evaluation of Novel Bioisosteres of an Adamantanyl Benzamide P2X7 Receptor Antagonist. *ACS Chem Neurosci*. 2017. 8(11):2374–80.
251. Schmidt S, Isaak A, Junker A. Spotlight on P2X7 Receptor PET Imaging: A Bright Target or a Failing Star?. *Int J Mol Sci*. 2023. 24.
252. Keller T, López-Picón FR, Krzyczmonik A, Forsback S, Takkinen JS, Rajander J, et al. Comparison of high and low molar activity TSPO tracer [^{18}F]F-DPA in a mouse model of Alzheimer's disease. *J Cereb Blood Flow Metab*. 2020. 40(5):1012–20.
253. Crabbé M, Van Der Perren A, Bollaerts I, Kounelis S, Baekelandt V, Bormans G, et al. Increased P2X7 receptor binding is associated with neuroinflammation in acute but not chronic rodent models for Parkinson's disease. *Front Neurosci*. 2019. 13(JUL):464363.

254. Jain P, Chaney AM, Carlson ML, Jackson IM, Rao A, James ML. Neuroinflammation PET imaging: Current opinion and future directions. *J Nucl Med*. 2020. 61(8):1107–12.
255. Venneti S, Lopresti BJ, Wiley CA. Molecular imaging of microglia/macrophages in the brain. *Glia*. 2013. 61(1):10–23.
256. Alam MM, Lee J, Lee SY. Recent Progress in the Development of TSPO PET Ligands for Neuroinflammation Imaging in Neurological Diseases. *Nucl Med Mol Imaging*. 2017. 51:p. 283–96.
257. Van Camp N, Lavisse S, Roost P, Gubinelli F, Hillmer A, Boutin H. TSPO imaging in animal models of brain diseases. *EJNMMI*. 2021. 49:p. 77–109.
258. Chen MK, Guilarte TR. Translocator protein 18 kDa (TSPO): Molecular sensor of brain injury and repair. *Pharmacol Ther*. 2008. 118:p. 1–17.
259. Nutma E, Fancy N, Weinert M, Tsartsalis S, Marzin MC, Muirhead RCJ, et al. Translocator protein is a marker of activated microglia in rodent models but not human neurodegenerative diseases. *Nat Commun*. 2023. 14(1):1–25.
260. Singh P, Adhikari A, Singh D, Gond C, Tiwari AK. The 18-kDa Translocator Protein PET Tracers as a Diagnostic Marker for Neuroinflammation: Development and Current Standing. *ACS Omega*. 2022. 7:p.14412–29.
261. Narayanaswami V, Dahl K, Bernard-Gauthier V, Josephson L, Cumming P, Vasdev N. Emerging PET Radiotracers and Targets for Imaging of Neuroinflammation in Neurodegenerative Diseases: Outlook Beyond TSPO. *Mol Imaging*. 2018. 17:p.1–25.
262. Beaino W, Janssen B, Vugts DJ, de Vries HE, Windhorst AD. Towards PET imaging of the dynamic phenotypes of microglia. *Clin. Exp. Immunol*. 2021. 206:p.282–300.
263. Janssen B, Vugts DJ, Windhorst AD, Mach RH. PET imaging of microglial activation - Beyond targeting TSPO. *Molecules*. 2018. 23:p.607.
264. Weissler B, Gebhardt P, Dueppenbecker PM, Wehner J, Schug D, Lerche CW, et al. A Digital Preclinical PET/MRI Insert and Initial Results. *IEEE Trans Med Imaging*. 2015. 34(11):2258–70.
265. Verscheijden LFM, Koenderink JB, de Wildt SN, Russel FGM. Differences in P-glycoprotein activity in human and rodent blood–brain barrier assessed by mechanistic modelling. *Arch Toxicol*. 2021. 95(9):3015–29.
266. Van Der Wildt B, Janssen B, Pekošak A, Stéen EJL, Schuit RC, Kooijman EJM, et al. Novel Thienopyrimidine-Based PET Tracers for P2Y12 Receptor Imaging in the Brain. *ACS Chem Neurosci*. 2021. 12(23):4465–74.
267. Zimmer ER, Parent MJ, Cuello AC, Gauthier S, Rosa-Neto P. MicroPET imaging and transgenic models: A blueprint for Alzheimer's disease clinical research. *Trends Neurosci*. 2014. 37:p.629–41.
268. Epis R, Gardoni F, Marcello E, Genazzani A, Canonico PL, Di Luca M. Searching for new animal models of Alzheimer's disease. *Eur J Pharmacol*. 2010. 626:p.57–63.
269. Do Carmo S, Cuello AC. Modeling Alzheimer's disease in transgenic rats. *Mol Neurodegener*. 2013. 8:p.1–11.

TURUN
YLIOPISTO
UNIVERSITY
OF TURKU

Painosalama, Turku, Finland 2024

ISBN 978-951-29-9603-2 (PRINT)
ISBN 978-951-29-9604-9 (PDF)
ISSN 0355-9483 (Print)
ISSN 2343-3213 (Online)